EXPERIMENTAL AND NUMERICAL INVESTIGATION OF MECHANICAL
PROPERTIES OF ADDITIVELY MANUFACTURED AUXETIC STRUCTURES

A THESIS SUBMITTED TO
THE GRADUATE SCHOOL OF NATURAL AND APPLIED SCIENCES
OF
MIDDLE EAST TECHNICAL UNIVERSITY

BY
MEHMET TAŞDEMİR

IN PARTIAL FULLFILLMENT OF THE REQUIREMENTS
FOR
THE DEGREE OF MASTER OF SCIENCE
IN
ENGINEERING SCIENCES

AUGUST 2022

Approval of thesis

EXPERIMENTAL AND NUMERICAL INVESTIGATION OF MECHANICAL PROPERTIES OF ADDITIVELY MANUFACTURED AUXETIC STRUCTURES

submitted by **MEHMET TAŞDEMİR** in partial fulfillment of the requirements for the degree of **Master of Science in Engineering Sciences Department, Middle East Technical University** by,

Prof. Dr. Halil Kalıpçılar   _____
Dean, Graduate School of **Natural and Applied Sciences**

Prof. Dr. Murat Dicleli   _____
Head of the Department, **Engineering Sciences**

Prof. Dr. Zafer Evis   _____
Supervisor, **Engineering Sciences, METU**

Examining Committee Members:

Prof. Dr. Dilek Keskin   _____
Engineering Sciences, Middle East Technical University

Prof. Dr. Zafer Evis   _____
Engineering Sciences, Middle East Technical University

Prof. Dr. Fahrettin Öztürk   _____
Mechanical Engineering, Ankara Yıldırım Beyazıt University

Assoc. Prof. Dr. Onur Tokdemir   _____
Civil Engineering, İstanbul Technical University

Assist. Prof. Dr. Yasin Sarıkavak   _____
Mechanical Engineering, Ankara Yıldırım Beyazıt University

Date: …./…./2022

I hereby declare that all information in this document has been obtained and presented in accordance with academic rules and ethical conduct. I also declare that, as required by these rules and conduct, I have fully cited and referenced all material and results that are not original to this document.

Name, Last Name: Mehmet Taşdemir
Signature:

ABSTRACT

EXPERIMENTAL AND NUMERICAL INVESTIGATION OF MECHANICAL PROPERTIES OF ADDITIVELY MANUFACTURED AUXETIC STRUCTURES

Taşdemir, Mehmet

Master's Degree, Engineering Sciences

Supervisor: Prof. Dr. Zafer Evis

August 2022, 134 pages

In this thesis, two novel unit cell designs were constituted by combining different auxetic structures in literature, and they were produced via the 3D printers, which is one of the most popular additive manufacturing methods nowadays. Based on the unit cells produced with various parameters, tensile and compression samples were manufactured and the mechanical properties of auxetic structures and their feasibility in the field of additive manufacturing were investigated. Although polymer-based materials are accepted as the base material of 3D printing technology, titanium and its alloys can also be used in various engineering applications such as additive manufacturing. In this context, the production of the samples was carried out using PLA and Ti6Al4V alloy, the specimens were subjected to tensile and compression tests, and their mechanical properties were investigated. Afterward, the microstructures of the samples were investigated by means of microhardness, SEM, FTIR, XRD, TGA, and DSC analyses.

Furthermore, with Finite Element Analysis, the tensile and compression tests of the samples were simulated in the computer environment and their comparisons with the experimental results were also carried out. In this thesis study, it was observed that the tensile and compressive strength of the unit cell increased as the angle between the branches forming the unit cell decreased. Furthermore, it was also achieved that the increase in the thickness values of the branches constituting the unit cell also leads to an increase in the tensile and compressive strength values of the unit cell.

Keywords: Auxetic Materials, Negative Poisson's Ratio, Lattice Geometries, Additive Manufacturing

ÖZ

EKLEMELİ İMALATLA ÜRETİLMİŞ ÖKZETİK YAPILARIN MEKANİK ÖZELLİKLERİNİN DENEYSEL VE SAYISAL İNCELEMESİ

Taşdemir, Mehmet

Yüksek Lisans, Mühendislik Bilimleri

Tez Yöneticisi: Prof. Dr. Zafer Evis

Ağustos 2022, 134 sayfa

Bu tez kapsamında literatürdeki farklı kafes yapılarının konfigürasyonu ile iki yeni birim hücre tasarımı oluşturulmuş ve günümüzdeki popüler eklemeli imalat yöntemlerinden biri olan 3 boyutlu yazdırma yöntemi ile üretimleri gerçekleştirilmiştir. Çeşitli parametrelerle tasarlanmış olan birim hücreler baz alınarak çekme ve basma numuneleri üretilmiş ve üretilen numunelerdeki kafes yapıların mekanik özellikleri ve eklemeli imalat alanındaki uygulanabilirlikleri araştırılmıştır. Polimer bazlı malzemeler 3D baskı teknolojisinin temel malzemesi olarak kabul edilse de titanyum ve alaşımları eklemeli imalat gibi çeşitli mühendislik uygulamalarında da kullanılabilmektedir. Bu kapsamda PLA ve Ti6Al4V alaşımı kullanılarak numunelerin üretimi gerçekleştirilmiş, üretilen numuneler çekme ve basma testlerine tabi tutulmuş ve mekanik özellikleri incelenmiştir. Daha sonra numunelerin mikroyapıları Mikrosertlik, SEM, FTIR, XRD, TGA ve DSC analizleri ile incelenmiştir. Ayrıca Sonlu Elemanlar Analizi ile numunelerin çekme ve

basma testleri bilgisayar ortamında simüle edilerek deneysel sonuçlarla karşılaştırmaları yapılmıştır. Bu tez çalışmasında, birim hücreyi oluşturan dallar arasındaki açı azaldıkça birim hücrenin çekme ve basınç dayanımının arttığı gözlemlenmiştir. Ayrıca birim hücreyi oluşturan dalların kalınlık değerlerindeki artışın birim hücrenin çekme ve basınç dayanım değerlerinde de artışa yol açtığı görülmüştür.

Anahtar Kelimeler: Ökzetik Malzemeler, Negatif Poisson Oranı, Kafes Geometriler, Eklemeli İmalat

I would like to dedicate this thesis to my dear wife and my parents, who gave encouragement in my academic achievements.

Fortis Fortuna Adiuvat

x

ACKNOWLEDGMENTS

I would like to wish to express my deepest gratitude to my supervisor Prof. Dr. Zafer Evis for his invaluable guidance, criticism, encouragements, comments and suggestions throughout the research.

For the technical assistance of Mr. Hossein Jodati and Dr. Ali Motameni are gratefully acknowledged.

I would like to offer my special thanks to Turkish Aerospace Industry for assisting with the production of samples and for the facilities they provide.

I am deeply grateful to my parents for their support and appreciation. Finally, I really thank my wife for her moral support throughout the thesis study.

TABLE OF CONTENTS

CHAPTERS

LIST OF TABLES

TABLES

LIST OF FIGURES

FIGURES

LIST OF ABBREVIATIONS

ABBREVIATIONS

3D	:	3-Dimensional
ABS	:	Acrylonitrile Butadiene Styrene
CAD	:	Computer Aided Design
DMLS	:	Direct Metal Laser Sintering
DSC	:	Differential Scanning Calorimetry
EDM	:	Electrical Discharge Machining
EBM	:	Electron Beam Melting
EBS	:	Electron Beam Welding
FTIR	:	Fourier-transform Infrared Spectroscopy
FDM	:	Fused Deposition Modelling
LENS	:	Laser Engineered Net Shaping
LM	:	Layered Manufacturing
NPR	:	Negative Poisson Ratio
PCL	:	Polycaprolactone
PLA	:	Polylactic Acid
SEM	:	Scanning Electron Microscopy
SLM	:	Selective Laser Melting
SLS	:	Selective Laser Sintering
STL	:	Standard Triangle Language
SLA	:	Stereolithography
TBI	:	Traumatic Brain Injury
TGA	:	Thermo Gravimetric Analysis
UV	:	Ultraviolet
XRD	:	X-Ray Diffraction

LIST OF SYMBOLS

SYMBOLS

°	:	Degree
°C	:	Celcius Degree
cm^3	:	Cubic Centimeter
G	:	Shear Modulus
g	:	Gram
GPa	:	Giga-Pascal
HV	:	Vickers Hardness
K	:	Bulk Modulus
kV	:	Kilovolt
L	:	Initial Length
m	:	Meter
mm	:	Milimeter
MPa	:	Mega-Pascal
N	:	Newton
R	:	Distance Between the Corner of the Square and the Center Point of the Ligament
R-Scale	:	Rockwell Hardness
t	:	Thickness of Ligament
Δ_L	:	Change of Length
E	:	Young's Modulus
ϵ_B	:	Longitudinal Elongation Rate
ϵ_E	:	Transverse Elongation Rate
θ	:	Angle of the Inner Structures
ν	:	Poisson's Ratio

CHAPTER 1

1. INTRODUCTION

1.1 Overview

Lattice geometry structures represent hollow shapes consisting of thin edges. A hollow and thin-edged geometry (re-entrant or hexagonal etc.) with continuously repeating morphology throughout the geometry is called as the unit cell of lattice geometry structures. Lattice geometry structures are difficult-to-process, have complex geometries, and their unit cells are quite small to be manufactured. For this reason, conventional manufacturing methods cannot be used to produce lattice geometry structures. Therefore, non-conventional manufacturing methods or additive manufacturing methods are preferred to produce lattice geometry structures. Moreover, lattice geometry structures have lightweight shapes and materials with different lattice geometries would have improved mechanical properties than the bulk materials.

1.2 Problem Statement

Poisson's ratio is a measure of strain behavior of materials in transverse direction in case of existence of an exerted lateral load. To give an example, if a material extends in transverse direction under a tension load the specimen is classified as negative Poisson's ratio. Visa versa, if a material shrinks in the transverse direction under tension, which is observed with most daily materials such as rubber, it is called positive Poisson's ratio. Negative Poisson's ratio is provided with auxetic geometries, if the given material naturally occupies aforementioned characteristics, therefore, a comprehensive investigation over novel auxetic geometries is a significant lack for the literature.

The thesis focuses on the answer to the question of how does ligament gap, ligament thickness, size effect over unit cell, and global alignment of the unit cell in spherical coordinate system affect Young's modulus, tensile strength, stress-strain characteristics.

1.3   Objective

In this thesis, two novel lattice structures designed and characteristics of these lattice structures modified following Box-Behnken method, and general properties of the lattice geometry structures, engineering fields, production methods, unit cell shapes and materials used in these structures were explained in detail. Therewithal, materials that used for lattice geometry structures, were also mentioned in conjunction with their production methods, mechanical properties and Poisson ratio's. Furthermore, application fields of different shaped lattice geometry structures, their specific geometries, and a special case for different ligament lengths related to mechanical properties were also discussed in this review. A Finite Element Method model also employed for further novel lattice cell which is validated with the empirical works.

To specifically summarize the objectives of this thesis:

- Design two different auxiliary lattice to design two different auxiliary lattice structures, which are candidate to have high strength additive manufactured functional parts. In the early stages of design, a literature review is conducted and alternative lattice geometries generated following Box-Behnken method.
- To characterize additive manufactured specimens to detect stress – strain characteristics following tensile and compression tests, and hardness character following microhardness experiments. Besides that, following instrumental analysis conducted for further investigations; scanning electron microscope (SEM), relative density (RD) to investigate sponge like structure, thermogravimetric analyzer (TGA) and differential scanning calorimetry (DSC).

- To characterize chemically, X-ray diffraction (XRD), Fourier transform infrared (FTIR) analysis conducted.
- To create a FEA model in order to compare empirical studies and numerical constitutive models for further studies, which would enable one to design novel auxetic studies computationally prior cost of time and money with experimental studies.

1.4 Significance

Auxetic structures have been used for various engineering applications. For instance, they have a place in engineering materials which are commonly used in packaging, transportation, heat sinks, electrical and electronical equipment's, automotive industry, biomedical, and aerospace engineering applications. Specifically, auxetic chiral structures can be used to prototype morphing wings, and also can be used in composite aero structures designs due to the fact that they show higher shear resistance. Since metals are much heavier than auxiliary composites and auxiliary composites have a higher strength-to-weight ratio than metals, they are more preferred in the aviation industry. Furthermore, auxiliary materials can be used in aviation applications such as thermal protection and noise cancellation applications of turbine engines.

CHAPTER 2

2. LITERATURE REVIEW

2.1 Additive Manufacturing

"Additive manufacturing" is an emerging technology in the growing industry that aims minimizing the production time of the end product, reducing the processes required to create final product, and facilitating the production of complex 3-dimensional (3D) geometries difficult to manufacture. The necessity for light and high-strength materials, especially in the aerospace and automotive sectors, has encouraged engineers and scientists working in these fields to search different ways from the traditional manufacturing methods [1]. Furthermore, the fact that additive manufacturing methods perform the prototyping phase of the product faster than traditional manufacturing methods has led to its spread in the industry. In recent studies and tests carried out, it has been observed that the mechanical, electrical, thermal properties, surface qualities, and dimensional accuracies of the samples produced by additive manufacturing methods fulfill the values required for the end product. Thus, "rapid prototyping" was developed and started to be used in the scientific world instead of prototyping with traditional manufacturing methods as "additive manufacturing" [2].

Additive manufacturing works with the principle of apposition and is carried out with deposition of material. In other words, it is based on the creation of the final product by depositing the material on a flat platform layer by layer [3]. Since the printing process is based on the same method as a typical printer, the systems used in the additive manufacturing method are called 3D printers. In recent years, 3D printer technology proves its importance rapidly in various fields due to advantages such as high precision, production of complex structures, personalized manufacturing, and rapid production [4]. 3D printing technologies particularly provide rapid production of complex parts and

facilitate their repair processes. Furthermore, 3D printing technology is preferred in various industrial fields such as medical sciences, aerospace and aviation, automotive, defense, electronics, civil engineering, etc. due to its advantages that ensure great convenience in part production [5]. In this context, unmanned aerial vehicles, fuel nozzles, gas turbines, mechanical gears, turbine blades, screws, and bolts biomedical implants, dental prostheses, electronic sensors, cardiac and vascular stents can be given as an example of final products fabricated with additive manufacturing [6].

When the academic studies in literature are examined, it was observed that the studies in the field of medical sciences occupy the largest place in 3D printer technology. Applications such as the production of patient-specific medical and dental implants, and printing of living tissue and artificial organs can be shown in some of the studies using additive manufacturing. For instance, it can be proved by the upper jaw bone restructuring processes applied in the field of dentistry that additive manufacturing provides personalized production, high precision and accuracy, and fast end product delivery. Furthermore, in studies, it has been observed that the scenario in which this process is performed using additive manufacturing is completed in a three-quarters shorter time than the scenario using standard implants and traditional production methods [7]. In another study, Bodnarova et al., [8] fabricated a Polylactic Acid (PLA) based porous scaffold by 3D printing technology and evaluated their cytotoxicity and biocompatibility under in vitro conditions. Moreover, Park et al., [9] attempted to create an effective artificial trachea via a tissue engineering method using 3D bio-printing in their study and they fabricated a multi-layered scaffold by using Polycaprolactone (PCL) and hydrogel with nasal epithelial and auricular cartilage cells in the printing process.

In literature, many studies have compared traditional and additive manufacturing methods. As an example, Dawoud et al., [10] observed the tensile and impact strength analysis of Acrylonitrile butadiene styrene (ABS) polymer by using both injection molding and Fused Deposition Modelling (FDM) methods. In consequence of the study,

they observed that both manufacturing methods have advantages and disadvantages against each other. In addition, in another study conducted by Puerta et al., [11], the vacuum casting method and FDM method were compared. Materials that are used in production have been determined as epoxy resin and PLA. Specimens produced by both methods were subjected to a tensile test. When the values were compared, it was observed that the specimen produced using PLA with the FDM method was 30% higher than the tensile strength value of the specimen produced using resin by vacuum casting method. As a result, the superiority of the FDM method over vacuum casting has been proven. From the studies, it can be clearly observed that additive manufacturing methods can compete with traditional manufacturing methods when the mechanical properties, surface properties, and production speeds of the samples are examined.

2.2　3D Printing Technologies

3D printing has become one of the most extensive additive manufacturing methods that is known in daily life. As a matter of fact, various lattice geometries with complex structure can be manufactured in 3D printers. To fabricate an object from 3D printers, geometry designed in the CAD environment must first be converted to a print format (STL) and then to a format called GCODE and transferred to a 3D printer. After that, designed geometry is processed layer by layer on the platform in the 3D printer and becomes the final product. In other words, user uploads CAD drawings into the 3D printer and obtain the desired end product via printers. Figure 1 represents 3D printers used in the production of the test specimens carried out in this thesis.
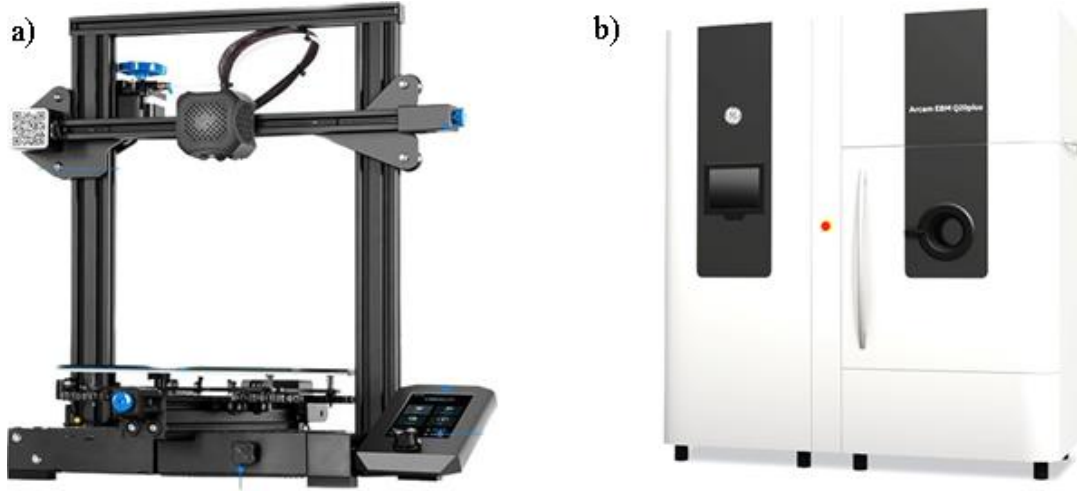
Figure 1. Demonstration of 3D printers used in this thesis study; (a) FDM method-based 3D printer: Ender 3 V2; (b) Electron Beam Modelling (EBM) method-based 3D printer: Arcam EBM Q20 Plus.

2.2.1   3D Printing Methods

As mentioned in the previous sections, 3D printing is an additive manufacturing technique developed to produce various structures and complex geometries from 3D CAD model data. The process comprises cumulative layers of material built on top of each other. It has been discovered by Charles Hull in 1986 in a process known as stereolithography (SLA). With the progress in material science, a wide range of methods have been developed in 3D printing technology such as FDM, powder bed fusion, electron beam melting (EBM), and inkjet printing. In this section, FDM, and SLA which are the most common polymer additive manufacturing methods will be explained. Furthermore, EBM, which is one of the extensive metal additive manufacturing methods, will also be explained. Moreover, the classification of additive manufacturing methods is shown in Table 1.

Table 1. Classification of additive manufacturing methods [12].

Method	Technology	Material	Type of Energy
Material Extrusion	FDM	Thermoplastic	Thermal Energy
		Ceramic Mud	
		Metal Paste	
Photopolymerization	SLA	Ceramics	UV Laser Beam
		Photopolymers	
Powder Bed Fusion	Selective Laser Sintering (SLS)	Polymers Ceramic Powders Metal Powders	High Energy Laser Beam
	Direct Metal Laser Sintering (DMLS)		
	Selective Laser Melting (SLM)		Electron Beam
	EBM		
PolyJet - Inkjet	Material Jetting	Photopolymers	Thermal Energy
		Vax	
Inkjet	Binder Jetting	Polymer Powders	Thermal Energy
		Metal Powders	
		Ceramic Powders	
Layer Lamination	Laminated Object Manufacturing (LOM)	Polymer Film	Laser Beam
		Sheet Metal	
		Ceramic Tape	
Directed Energy Deposition	Laser Engineered Net Shaping (LENS)	Molten Metal Powder	Laser Beam
	Electron Beam Welding (EBW)		

2.2.1.1 Fused Deposition Modelling (FDM)

FDM method is the process of 3D printing of material layers in a certain plane, with layer-by-layer deposition of a thermoplastic polymer by melting. The polymer filament is first heated in the nozzle to a semi-liquid state, and then the liquid polymer is extruded on the platform or onto preprinted layers.

The thermoplasticity of the polymer filament is an extremely important feature in this method, which ensures the fusion of the filaments with each other during the printing phase and solidification at room temperature after printing. The layer thickness, width, direction of the filament and the air gaps that may occur in the same layer or between the layers are the main parameters that affect the mechanical properties of the parts to be produced in the FDM method (Mohamed et al., 2015) [13]. Furthermore, the main advantages of the FDM method can be shown as low cost, high production speed and simplicity of the process. On the other hand, the low strength caused by the inter-layer distortion, the layered appearance, poor surface quality and the inadequacy of thermoplastic material diversity are the main disadvantages of the FDM method [14]. Schematic diagram of FDM is shown in Figure 2.
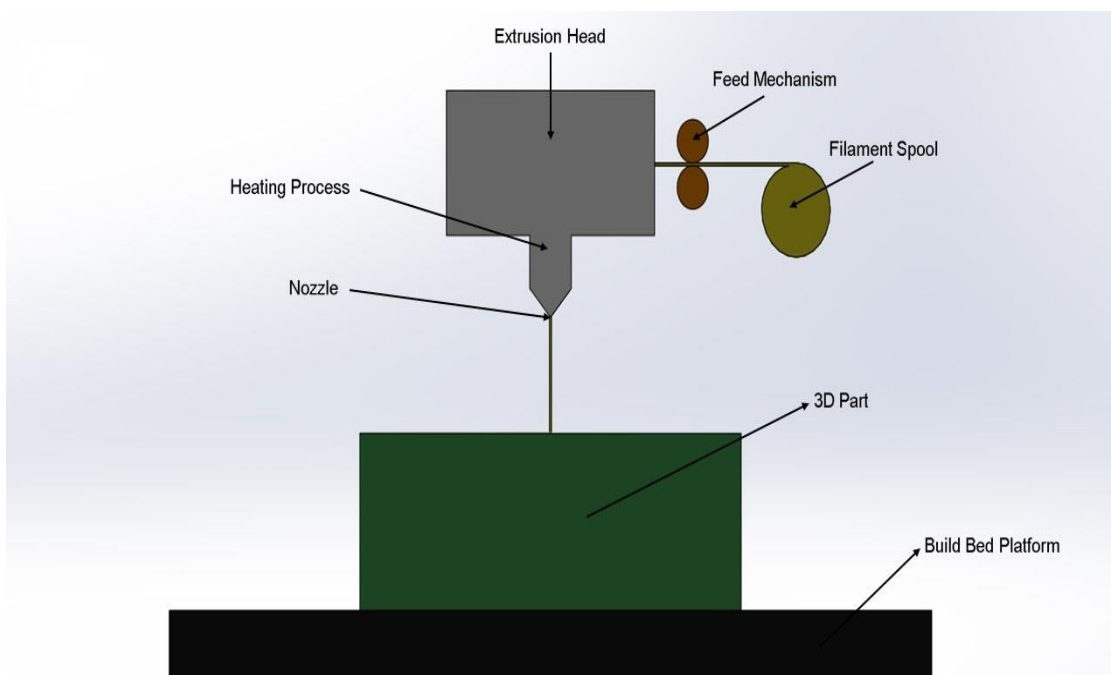
Figure 2. Schematic diagram of fused deposition modelling

2.2.1.2 Stereolithography (SLA)

The SLA method is one of the earliest additive manufacturing methods developed. This method is based on the principle of reflecting UV light into a liquid resin or monomer solution with photopolymer (which can solidify under light) and creating the desired design layer by layer. As an example of the photopolymer resins used in this method; epoxy, acrylic and rubber can be given. At this point, the UV light initiates a chain reaction on the resin or monomer solution layer. Monomers are UV-active and they are converted into polymer chains instantly after activation (radicalization). After polymerization, a pattern inside the resin layer is solidified so that the layers to be added adhere to each other. After completion of printing, unreacted resin is removed. In general, mechanical properties of the end-products fabricated by the SLA method are quite low. Therefore, the final products need to be subjected to some post-treatments such as annealing or curing in order to achieve the desired mechanical performance. The biggest advantage of this method is that final products with high resolution quality can be produced with this method. Hence, it is possible to print high quality parts at a resolution as low as 10μm with the SLA method [15].

On the other hand, the disadvantages of this method are that it is relatively slow and much more expensive than other additive manufacturing methods, and the range of materials for printing is limited. Nowadays, additive manufacturing of complex nanocomposites can be performed effectively with the SLA method [16]. Working principle of stereolithography is shown in Figure 3.
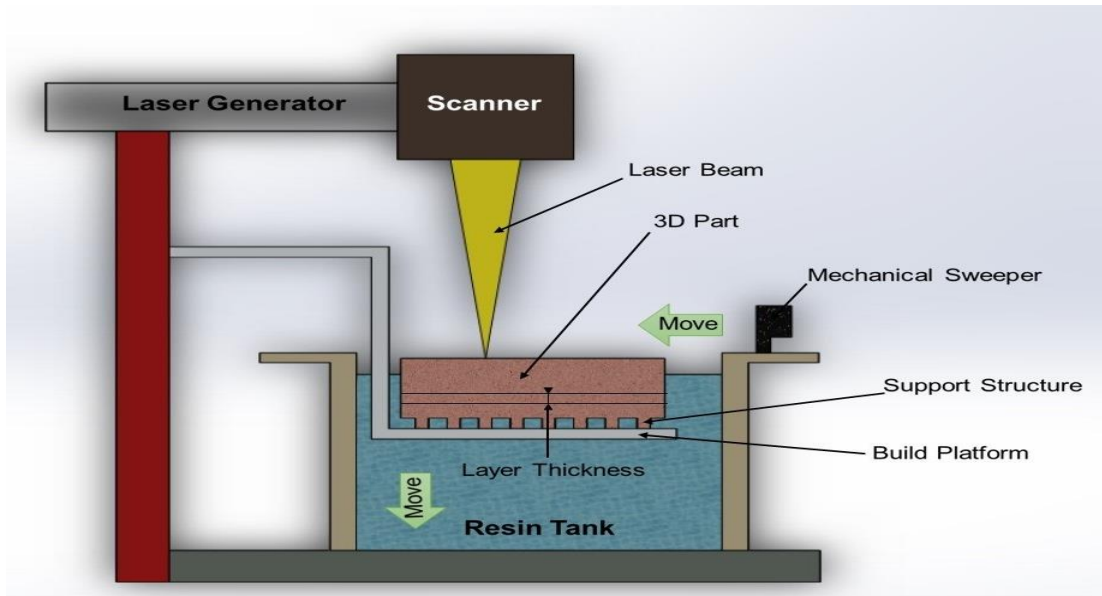
Figure 3. Working principle of stereolithography method.

2.2.1.3 Electron Beam Melting

EBM method is a 3D printing technology that is very similar to the SLS method at first glance. However, a closer examination of the two methods reveals that EBM differs in several ways. The most important discrepancy is that the energy source comes from the electron beam instead of the CO_2 laser, and the material used is a conductive metal instead of a thermoplastic polymer. All 3D printers working with the EBM method consist of an energy source capable of emitting the electron beam, a powder container, a powder feeder, a powder recoater and a heatable build platform. In this method, the process begins with the powder recoater that is depositing a layer of powder onto the preheated build platform. After the powder is set, the melting process begins with electron beams. The electron beam is controlled by a set of electromagnetic coils that regularly direct the beam towards desired points of the build platform. The electron beam acts selectively as it melts the powder, thereby causing the powder particles to fuse together. The important thing to note is that whole printing process must take place under a vacuum. Schematic diagram of EBM method is shown in Figure 4.

12
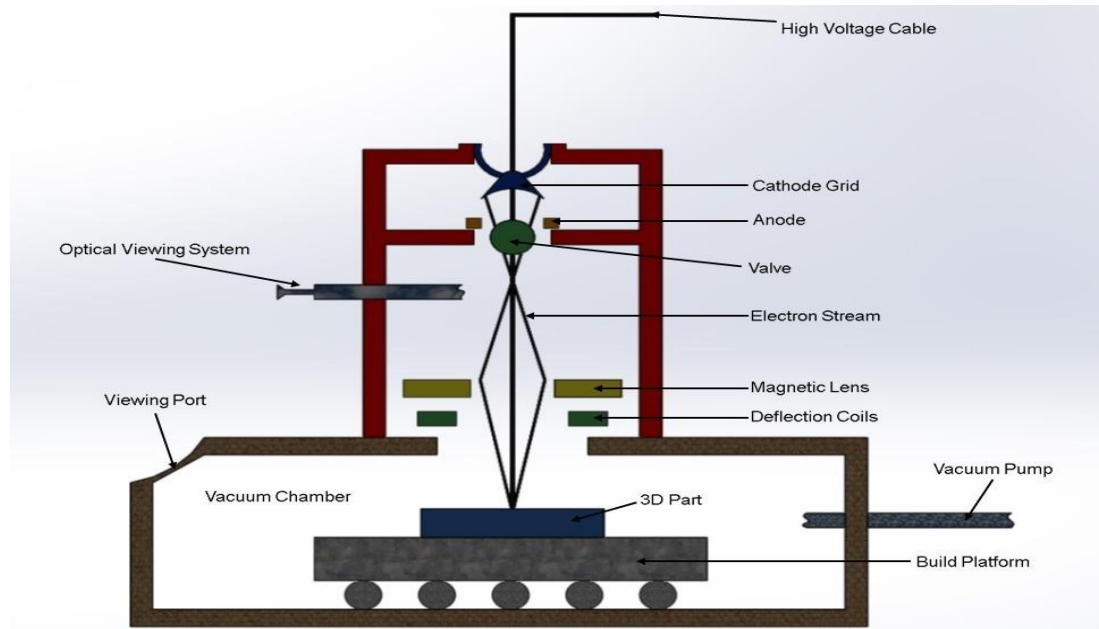
Figure 4. Schematic diagram of EBM.

2.2.2 3D Printing Materials

With the developments of methods, a wide range of materials have been started to be used in 3D printing including polymers, metals, ceramics, and concrete. The materials used for 3D printing are as diverse as the raw materials required for the production methods. Thus, 3D printing allows manufacturers to determine the geometric, mechanical, thermal, etc. properties they want to provide in the products to create. In this section, 3D printing materials that are widely used today will be examined.

2.2.2.1 Polymers

Polymers with thermoplastic properties have become one of the most important raw materials of 3D printer technology due to their ability to be easily shaped under high temperatures. Polymers, which can be easily shaped when they reach a certain temperature, have been actively used in the market due to their easy applicability and low cost, although they do not have as high mechanical properties as metals or ceramics.

Today, polymers are widely used in sectors such as automotive, aerospace, food, and medical. For polymers to be usable in 3D printers, they must first be converted into a filament form. Filaments are the raw materials used by 3D printers working with the FDM method to obtain the final product. In this context, polymers are first prepared in a bead-shaped spherical form called granules. Afterward, it is transferred into the extruder, which is the equipment of the system called filament drawing system, and heated under a certain temperature. As a result of this process, a filament form with the desired diameter and length is obtained. PLA and ABS have become the base polymers used in 3D printing processes nowadays. Various properties of common 3D printing polymers are shown in Table 2.

Table 2. Common properties of various 3D printing polymers [4].

Properties	Ultimate Tensile Strength	Printability	Extruder Temperature	Bed Temperature	Flexibility
PLA	65 MPa	High	190-220 °C	45-60 °C	Low
ABS	40 MPa	High	220-250 °C	95-110 °C	Low
TPU	25-45 MPa	Medium	225-245 °C	45-60 °C	High
PETG	50-60 MPa	High	230-250 °C	75-90 °C	Low
NYLON	50-60 MPa	High	220-270 °C	70-90 °C	High
POLY-PROPYLENE	30-40 MPa	Low	220-250 °C	85-100 °C	High

PLA, one of the most common polymers used in additive manufacturing methods, is an organic biopolymer and thermoplastic produced from corn starch and sugar cane. Therefore, it is not harmful to human health. This feature has made PLA widely used in the biomedical field. In addition, PLA is a biodegradable material and it can decompose in less than three months. Automotive, aerospace, biomedical, and robotics fields can be shown as the most extensive usage areas of PLA polymer. PLA is used in the literature to obtain the final product by using the FDM method and to investigate the mechanical properties and microstructure analyzes of different lattice geometries.

On the other hand, the most prevalent polymer material used in additive manufacturing applications is ABS, which is a petroleum-based thermoplastic. Due to the fact that it cannot be preferred in the biomedical field. However, its high strength becomes ABS utilizable in various prototyping studies of engineering fields, automotive industry, and aerospace industry. In literature, the behavior of ABS polymer in different 3D printers and its tensile strength values in different orientations, infill values, and indifferent layer thicknesses have been investigated.

2.2.2.2 Metals

Another type of material popularly used in the 3D printing industry is metals. Metal-based additive manufacturing methods contain many different types of production technologies. These systems vary according to the type of energy source or the way the material used is transferred. In the printing process, the metal in powder form on the table is fired to form a solid piece. In order to fabricate a solid piece, the relevant parts of the powdered metal are melted layer by layer to reach the required hardness. After this process, the final product is obtained by purifying the produced part from unheated and loose powders. EBM and SLM can be shown to be the most popular metal-based additive manufacturing technologies used in the industry recently.

Metallic materials are preferred due to their superior mechanical properties. In additive manufacturing metal powders are used to obtain products due to the fact that metals require high energy to be melted and re-shaped, it expedites processing and handling. The quality of metal powders is an important issue and directly affects the mechanical properties of the part to be produced. Thanks to metal powders, a wide variety of alloys can be included in additive manufacturing technology. Most of the used alloys are:

- Steels,
- Nickel and cobalt based superalloys,
- Titanium alloys,
- Aluminum alloys,

Apart from these metals, various metals are in the process of being evaluated and used for additive manufacturing. The most important examples of them are:

- Copper alloys,
- Magnesium alloys,
- Precious metals such as gold, silver, platinum,
- Metals that cannot be easily machined such as molybdenum, tungsten, tungsten carbide,
- Metal matrix composites.

2.2.2.3 Ceramics

Ceramic additive manufacturing follows the same design and production procedures as plastic and metal additive manufacturing. However, sintering shrinkage of the material, as well as any deformations of the component, must be considered during the design stage. In general, additive manufacturing of ceramics refers to the shaping stage of the production process, which includes everything from selection of raw materials through the product finishing.

The benefit of this technique is that it allows complicated structures to be produced close to their ultimate near-net form without the need for specialized equipment. Furthermore,

high-precision high-speed printing technology has been enhanced by improving and fusing current technologies. Preceramic polymers and composite materials have been used in a range of material investigations to create ceramic structures with improved characteristics. C-AM has been used in a variety of fields, including medicine, energy, manufacturing, and construction, as a result of these research. The significance of C-AM-based ceramic manufacturing technology is proven by these ongoing growths and diversified outcomes.

2.3   The Printing Problems in FDM

Layered manufacturing (LM) is the most popular method for rapid prototyping (RP), which focuses on design verification, visualization, and kinematic functionality testing. RP is an advanced and one of the most promising techniques to produce prototypes and models that can be used directly in a variety of fields. [17]. LM, which produces arbitrary items using computer-controlled manufacturing, sends computer-generated solid models of the parts straight to a 3D printer. It is a very effective and tested method for cutting the time and expenses associated with product development and manufacturing [18]. SLS, FDM, and SLA are three of the LM technologies available. Fused deposition modeling is one of the most promising RP techniques when it comes to cost-effectiveness and production speed. The term itself also indicates the approach in which fused material is deposited in layers to make a part. The FDM procedure only provides the phases of melting, extrusion, and resolidification in order to construct a physical component by the addition of fused material in layers with the aid of adhesion. The process sequence shows that thermoplastic materials are required for this production technique. It is widely utilized, and this category includes roughly half of all 3D printers [17].

In FDM, an electric motor and heat are used to extrude the filament material through the nozzle in a fluid phase to create a model that was previously designed on CAD software. A feeding motor extrusion is controlled by a controller to maintain the extruder's feed rate. Depending on the change in inner pressure in the FDM nozzle and layer thickness, the feeding rate and motor torque can be adjusted. The extruded material is joined to the preceding layer by a weld because the construction material is heated to a temperature above its melting point and is planned to solidify less than 0.1 seconds following the extrusion process. On a gantry-robot that can move in both X and Y directions, the nozzle is mounted. Furthermore, flat plates for many FDM printers can be made of glass or aluminum. When a layer is fully extruded, the bed descends in accordance with layer thickness, and the nozzle moves into position for the subsequent layer. The FDM system uses support materials to construct intricately structured physical objects. These materials offer integrity while supporting overhanging sections during manufacturing. These support structures are cleaned by breaking them or by using specific solvents after the main section has been removed from the build platform.

In addition, the primary element is constructed on a flat support known as the printing bed that has supporting structures laid down layer by layer [1]. To reduce material, use and construction time, supporting materials can be created either horizontally or vertically. The size of typical consumer-grade 3D printers has dropped over the past few decades, and they have been replaced by cubic desktop printers, which typically have edge lengths between 50 cm and 100 cm and weigh between 5 and 10 kg. Although 3D printers may now be used almost everywhere due to their reduced size, they must be kept out of the user's reach because to the hazardous gases that are produced when the filament melts. For instance, ABS is a harmful material that, if inhaled, might give you a headache or other health issues. Figure 5 gives a presentation of the FDM.
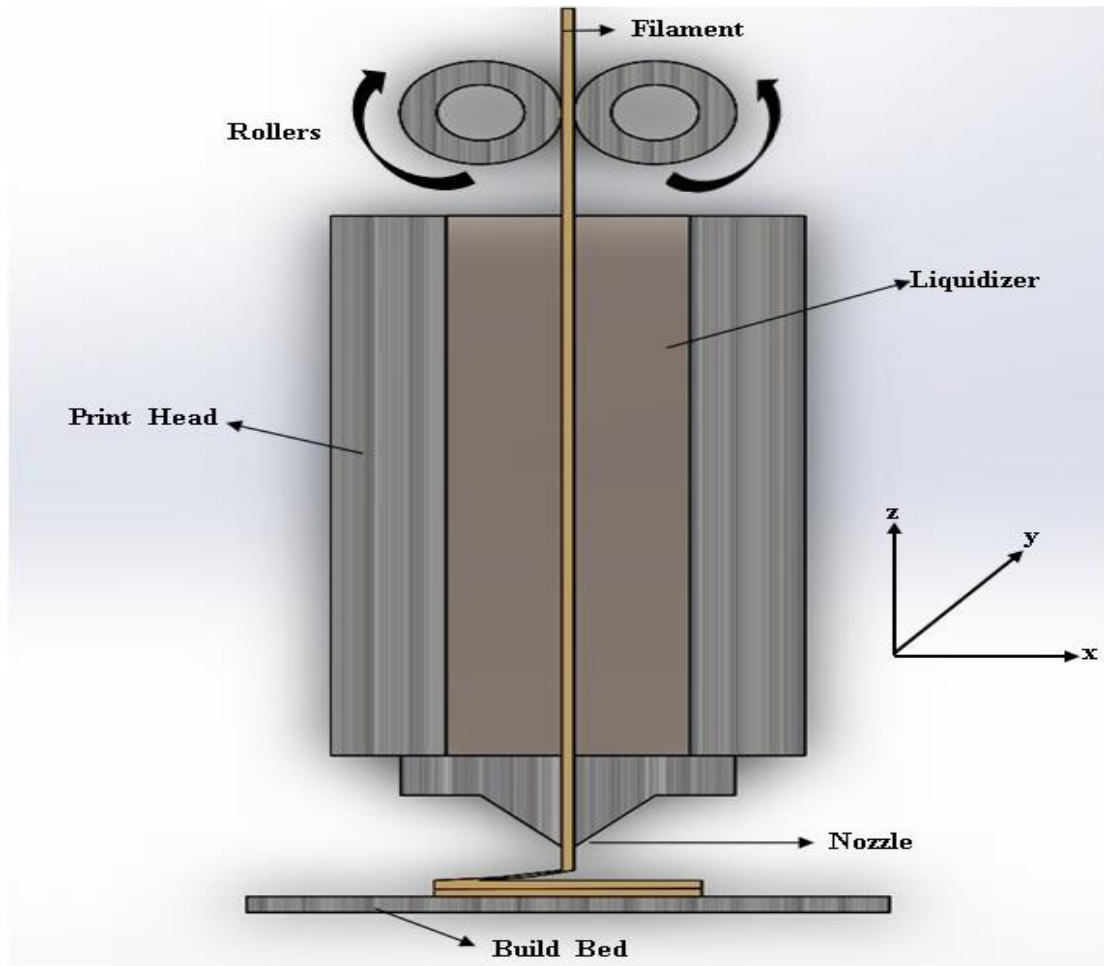
Figure 5. Demonstration of FDM 3D printing method.

Minor and large flaws may occur when a physical part is printed because the material flow may occasionally be blocked by unique problems. Minor flaws may not be considered if the preceding and/or following layers make up for the missing or flawed layer. On the other hand, if serious flaws develop, a 3D-printed part cannot be used in the intended production and may even be rejected. To avoid these kinds of flaws, the 3D printing process must also be properly understood, and appropriate steps must be taken. Otherwise, a typo results in a loss of resources like time and money.

The printing defects can be grouped according to Anitha et al., [17] as listed:

- An incorrectly aligned print platform
- Nozzle alignment issues
- Running out of printing supplies or interrupted material flow
- Loss of adherence to the print platform or a lack thereof
- A snap or shock (from the printer or another source)
- Inappropriate modifications to printer settings

2.3.1   Misalignment of the Print Platform

If the 3D printer is not calibrated or tuned properly, misalignment of the print platform might result in serious issues, including deformation of the print platform or nozzle. The layer thickness is determined by the movement of the print platform, which only moves in the Z direction. The next layer in some situations will not stick to the prior layer, or extruded materials may bow out if the length of steps cannot be controlled properly.

A misaligned print platform can also result in a variety of issues, including print that does not adhere to the platform, nozzle penetration or deformation of the print platform, print that bows out at the bottom (known as an elephant's foot), bent print edges (warping syndrome), and a failure to capture fine detail. Therefore, it is important to examine if there is any bending or printing debris that prevents the threaded rods or lead screws from moving the nozzle in the X and Y directions or leveling up or down the construction plate. Therefore, it's crucial to wipe the rods clean of any residue before putting on a fresh coat of lubrication.

2.3.2 Misalignment of the Nozzle

The gantry-robot, which consists of two stepper motors, belts, and pulleys, can move the nozzle. At this point, some issues that affect the operation of motors, belts, and pulleys also affect the nozzle position, making it impossible to create a physical representation of the nozzle position as it is modelled by CAD software. The primary problems with these printer components are belt tension, loose grub screws, and printing debris that prevents the nozzle from moving steadily.

The issues listed above can result in the print head missing the bed, poorly aligned layers, missing layers, slanted printed pieces, and print offsets in some areas (shifted layers). The grub screws on the pulleys on the X and Y-axis motors must be tightened, and the rods must be checked to see if they are straight by rolling them across a level surface. Cleaning print dirt, wiping rods, and lubricating necessary parts are also essential. Additionally, end switch/stop issues can result in issues with the print platform being missed. The end switch is inoperative on the X or Y axes if the nozzle remains on one of the edges without moving.

2.3.3 Depletion of Printing Material or Disrupted Material Flow

The spool needs to be examined to see if there is enough material before printing the real model. However, other issues might sometimes arise in addition to the filament running out. Other frequent issues include stripped filament, low diameter filament, broken filament, and blocked nozzles. High-quality filaments must be used, and the spool must be examined, to avoid difficulties caused by the filament.

The clogged nozzle, which prevents the flow of the melted filament, is one of the common and significant issues. The blocked nozzle can be cleaned using a variety of techniques; the most popular ones involve heating the nozzle to a reasonable temperature and cleaning with a needle with a smaller diameter than the nozzle diameter. However, given the high temperature of the nozzle in this scenario, safety is crucial. Other techniques include pushing the filament through with another piece of filament, heating the nozzle to high temperatures in an oven to turn remaining filament in the nozzle into a carbonized substance, and cleaning the nozzle by soaking it in Acetone or another solvent.

2.3.4 Lack or Loss of Adhesion to the Build Platform

Sometimes prints fail to adhere to print platforms, and as a result, warping syndrome can develop, eventually destroying the physical model. This issue can be attributed to a number of factors, including an uneven platform, a lack of calibration, a low heated platform, a low heated filament, and a dirty platform. The following techniques can be used to solve this issue: giving the platform some texture, adjusting the print platform height, applying cleaning agents to the platform, employing supports, and using the printing bed. Perforated print platforms are being used with Ender 3 V2 to avoid this problem, which solves adhesion problems to the most cases. A thin layer of water-soluble adhesive can be applied on flat print platforms of other types, and this glue can then be removed with hot water after printing. Decorator tape is another remedy for things printed using PLA filament. As was already noted, the nozzle's distance from the platform is crucial for the initial layer's adherence and must be carefully adjusted.

2.3.5 Shock and Vibration

Vibration is a crucial factor that has an impact on print quality. The moving components of 3D printers, particularly the acceleration and shake of the gantry robot, are what cause vibration or shock. Visual waves can be produced on the print surface by shock or vibration. First of all, the 3D printer needs to be placed on a stable, flat surface or table to support the machine in order to stop this phenomenon. Poor maintenance and damaged linear bearings may also be the root cause for the vibrations. The pulleys, bits, and grub screws must all be sufficiently tight. For the gantry robot to travel easily, the rails must also be free of debris like dust, dirt, and fluff, and the rods must be well oiled. The print speed can be slowed down if all technical precautions have been followed but there are still visible waves on the print as a result of vibration. Bowden type extruders are much lighter than direct type extruders, this issue is not very effective for printers that use them. In the Bowden type, the extruder is stationary and not moving like the direct type; it is placed behind the printer or somewhere close to the spool. As a result, it decreases inertia as well as the weight of the moving part.

2.3.6 Inaccurate Adjustments of Printer Settings

The extruder flow ratio, print speed, nozzle distance, infill type, infill density, surface layers, supports, seam type, and fan speed are just a few of the numerous variables that may be controlled by the printer parameters. They are all crucial factors to consider when determining print quality. Stringing issues are the most frequent issue related to printer settings, and they may be avoided by cleaning the nozzle and raising the fan speed. After taking these steps, if the problem persists, adjusting the filament's melting temperature may be the answer. Additionally, due to contradiction, the size of the holes may be too tiny compared to the indentation, in which case increasing the hole diameters by around 0.3 mm over the intended one can solve the issue. Another printer setting issue is hanging strands, which may be avoided by adjusting the support angle, fan speed, and layer thickness.

2.4   Lattice Structures

In this thesis, structures with lattice geometries, the unit cells of these structures, different shapes in these cells, cell sizes, and the angles and thicknesses of the branches forming the edges of the lattice geometries are examined. In addition, a detailed literature review of the effects of these geometries on mechanical properties is evaluated under this title. The thermoplastic property of polymers shows that they can be shaped when exposed to heat. For this reason, polymers are a frequently preferred material in 3D printers. Hollow figures with thin edges represent structures with lattice geometry. Compared to conventional structures, these structures meet the same mechanical properties in a lighter form than these structures. Their high strength behavior together with their high lightness properties have made lattice geometry structures important. Lattice geometry structures have a very important place in engineering materials. Packaging, transportation, heat transfer equipment (due to its high heat transfer properties), electrical and electronic equipment (due to its good electrical conductivity properties), different engineering materials such as smart filters and sensors are some of them. As the final product, these structures can be used as aircraft wing prototypes. In addition, composite space equipment can be produced from these structures due to the high shear modulus and the fact that composite structures are lighter than metals.

2.4.1   Poisson Ratio and Lattice Structures

The Poisson ratio is a characteristic feature of materials which was asserted by S. D. Poisson. Deformation of material in directions perpendicular to the loading direction is called as Poisson ratio [19]. This ratio can be positive or negative. While most materials have a positive Poisson ratio, some natural and artificial materials with a negative Poisson ratio have been found recently. The Poisson's ratio theoretically varies between -1 and 0.5 for elastic isotropic materials. While the ratio increases positively in elastic materials such as rubber, it is close to zero in harder materials. Poisson ratio values of some significant materials are listed in Table 3.

Table 3. Poisson's ratio values for various materials [20].

Material	Poisson Ratio (Upper limit is 0.5)
Aluminum	0.334
Copper	0.285
Brass	0.357
Bronze	0.34
Clay	0.41
Concrete	0.1 - 0.2
Cork	0
Glass	0.22
Granite	0.2 - 0.3
Iron	0.22 - 0.30
Marble	0.2 - 0.3
Polystyrene	0.34
Rubber	0.48 - ~0.5
Steel, cast	0.265
Titanium	0.32

The Poisson ratio is generally denoted by the symbol nu (v) and is defined by the Equation 1 and 2:

$$v = -\varepsilon_E / \varepsilon_B \qquad (1)$$
$$\varepsilon = \Delta_L / L \qquad (2)$$

Where;

v = Poisson ratio

ε_E = Transverse Elongation rate

ε_B = Longitudinal Elongation rate

Δ_L = Change of Length

L = Initial Length

In most engineering materials, there are practical relations between Poisson's ratio and Young's modulus (E) (elasticity), shear modulus (G), and axial stiffness (K) (rigidity) by which material properties can be determined. These relations are shown in Equations 3 and 4.

$$v = \frac{3K - 2G}{6K + 2G} \tag{3}$$

$$G = \frac{3K(1 - v)}{2.(1 + v)} \tag{4}$$

Where;

E – Young's modulus

G – Shear modulus

K – Bulk modulus

Herein, Equation 3 shows the relationship between axial stiffness and shear modulus with Poisson's ratio, while Equation 4 shows the cohesion between shear modulus and Young's modulus with Poisson's ratio. In general, the Poisson's ratio is a significant mechanical property that takes a substantial place in elastic material deformation.

In accordance with Newton's third law of motion, a substance exposed to a force creates a reaction with a force in the opposite direction of the acting force. For instance, when a material is subjected to a tensile force from one axis, it shows elongation behavior in the same axis, while it shows shrinkage in another axis perpendicular to the same axis. Furthermore, when a material is compressed from a particular axis, shrinkage occurs in the same axis, whilst expansion occurs in the other axis. On the other hand, some of the materials show an unconventional situation in the Poisson ratio due to their geometries. In this phenomenon, expansion occurs perpendicular to the stretched axis when the structures are stretched from two particular axes parallel to each other. Similarly, shrink

occurs perpendicular to the stretched axis when structures are compressed from two different axes parallel to each other. This property is called the negative Poisson ratio, and materials with this property are called "Auxetic" materials. This is the main feature that makes auxetic materials special and it has the potential to create new horizons in today's material production industry. Although various materials have this phenomenon, it is not observed in many of them.
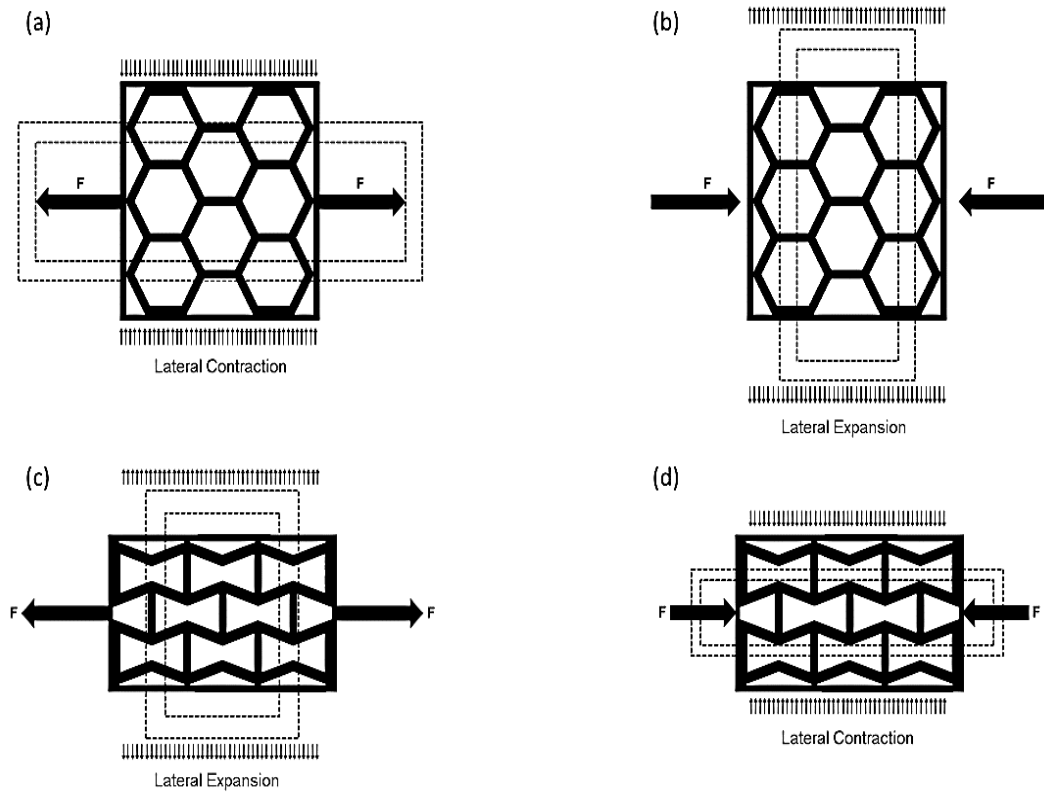
Figure 6. Deformations of conventional and auxetic materials under tensile and compressive forces; (a) Conventional behavior of Honeycomb structure under tension load; (b) Conventional behavior of Honeycomb structure under compression load; (c) Auxetic behavior

Figure 6 compares both conventional and auxetic structures according to their reaction under different forces. As seen in Figure 6a, when conventional materials are subjected to a tensile force from a certain axis, they show shrinking behavior in the axis perpendicular to the tensile axis. Likewise, when conventional materials are compressed from a certain axis, they experience an expansion in the axis perpendicular to the axis on which the compressive force is applied. Figure 6a and Figure 6b are characteristic of materials with positive Poisson ratio. On the other hand, this situation is seen with the opposite behavior in auxetic materials. On the contrary to what is known, when auxetic materials are subjected to a tensile force from one axis, expansion occurs in the other axis which is perpendicular to the tensile axis. Schematics about this situation are shown in Figure 6c and Figure 6d.

2.4.2 Lattice Structures with Positive Poisson Ratio

Poisson's ratio, which is one of the distinguishing features of materials, can vary depending on the shape, geometry, and porous structure of the material. Lattice structures with convex geometries in their structures tend to contract from convex corners when exposed to tensile forces. This situation shows that structures with convex geometry have a positive Poisson's ratio. When the studies in literature are examined, it is seen that honeycomb, diamond, triangle, kagome, and some chiral geometries are the most extensive lattice geometries which exhibit positive Poisson ratio. Detailed examinations of these lattice structures are constituted in the continuation of the study and studies were carried out related to these structures are listed in Tables 4-12. Moreover, specific features of lattice structures such as, materials and production types, test standards, mechanical properties, and references are shown in these tables. In the related studies, some specific values were not specified accurately. Therefore, values which were not given in the related articles are indicated by the dash (-) symbol in these tables.

2.4.2.1 Honeycomb Geometry

In the researches, it has been observed that the most preferred lattice geometry structure is the honeycomb geometry. By altering the length, thickness, and angle values of its branches, the changes in the mechanical properties were examined. Due to its geometric structure, it shows high mechanical properties under compression forces. Therefore, honeycomb geometry exhibits a positive Poisson's ratio. The details of the studies carried out within honeycomb geometry are shown in Table 4 within various subsections such as type of materials and lattices, production methods, test standards, and related studies.

Table 4. Mechanical properties of Honeycomb structures produced from various materials.

Lattice Type	Production Method	Material	Mechanical Properties			Test Standard	Reference
			υ	E (MPa)	σ (MPa)		
Honeycomb	FDM	PLA	-0.5	-	-	-	[21]
Honeycomb	Polyjet	VeroWhite	1	-	-	BS EN 10305-5	[22]
Honeycomb	SLM	Al Alloy	1	-	4.66	-	[23]

Mechanical properties (υ, E, σ) of lattice geometries are also listed in Table 4 as υ is the Poisson ratio, E is the modulus of elasticity and σ represents the compressive strength of materials. The units of modulus and strength are in MPa.

2.4.2.2 Quadrangle (Diamond) Geometry

Diamond geometry is one of the rarely preferred geometries among lattice geometry structures. This geometry exhibits a positive Poisson ratio due to its convex branch structure. When the studies in literature are examined, it is seen that the samples with diamond geometry exhibit better mechanical properties under tensile force compared to other geometries. The studies in literature related to investigation of quadrangular lattice structure are given in Table 5.

Table 5. Mechanical properties of Quadrangle lattice structure produced from various materials.

Lattice Type	Production Method	Material	Mechanical Properties			Test Standard	Reference
			υ	E (MPa)	σ (MPa)		
Quadrangle (Diamond)	SLS	Nylon	1	-	-	-	[24]
Quadrangle (Diamond)	EBM	Ti6Al4V	-	445	75	-	[25]
Quadrangle (Diamond)	Electrical Discharge Machining (EDM)	Ti6Al4V	-	290	11	ASTM C365	[26]

2.4.2.3 Triangular Geometry

Triangular geometry is one of the most frequently used lattice geometries in literature after honeycomb. It is usually deployed as equilateral triangle geometry inside lattice structures. It allows the end-product which is designed to be produced lighter under the same loads. Its properties under tensile and compressive forces are relatively good compared to other geometries. It exhibits a positive Poisson ratio due to its convex branch structure. The studies based on the examination of triangular lattice structure are listed in Table 6.

Table 6. Mechanical properties of Triangular lattice structure produced from various materials.

Lattice Type	Production Method	Material	Mechanical Properties			Test Standard	Reference
			υ	E (MPa)	σ (MPa)		
Triangular	FDM	PLA	-	49.07	1.02	ASTM D695-D638	[27]
Triangular	SLA	L5D1.1	0.25	16.87	0.67	ISO 13314:2011	[28]
Triangular	SLA	Polymer resin	0.2	-	-	-	[29]

2.4.2.4 Kagome Geometry

Kagome structure is a rarely preferred lattice structure in literature. It is constituted by gathering two equilateral triangles opposite each other. In other words, it includes two interbedded triangular unit cells which one of these triangles is in a position rotated as 180 degrees. It generally exhibits a positive Poisson's ratio. Although there are a few

studies related to Kagome geometry in literature, two different studies are found and listed in Table 7.

Table 7. Mechanical properties of Kagome lattice structure produced from various materials.

Lattice Type	Production Method	Material	Mechanical Properties			Test Standard	Reference
			υ	E (MPa)	σ (MPa)		
Kagome	FDM	ABS	-	1.51	18	ASTM D638	[30]
Kagome	SLM	Ti6Al4V	0.5	-	-	-	[31]

2.4.2.5 Square Geometry

Square geometry is one of the most frequently used lattice geometries in the manufacturing of parts where the strength under the same load is provided by a lightweight structure. Four different ligaments are included inside a single square geometry, and these ligaments constitute two distinct parallel ligament groups. Ligaments belonging to distinct groups are perpendicular to one another. Therefore, all interior angles are equal to 90 degrees. Although square geometries may have identical ligament lengths, their ligament lengths may vary.

Square geometries with different ligament lengths are also called rectangular geometries. Moreover, square lattice geometries generally have a null Poisson ratio due to their ligament structure and specific geometries. The literature review of square lattice geometry is given in Table 8.

Table 8. Mechanical properties of Square lattice structure produced from various materials.

Lattice Type	Production Method	Material	Mechanical Properties			Test Standard	Reference
			υ	E (MPa)	σ (MPa)		
Square	FDM	PLA	0	-	-	-	[21]
Square	FDM	Polyethylene (LDPE)	0.05	-	-	-	[32]
Square	SLA	Rubber	-0.6	-	-	-	[33]
Square	SLS	Nylon	0.25	-	-	-	[34]
Square	Polyjet	PolyJet photopolymer	-2	848.3	4	-	[35]

2.4.3 Lattice Structures with Negative Poisson Ratio

Structures with concave geometries expand from the concave corners under the effect of tensile load. Materials that shown this phenomenon are called auxetic materials and they exhibit a negative Poisson ratio. When the literature is examined, it is seen that re-entrant, arrowhead, star, and some chiral geometries have shown negative Poisson ratios under tensional and compressional loads.

2.4.3.1 Re-Entrant Geometry

Re-entrant is the most preferred lattice geometry when the studies in the literature are examined. Due to its geometric structure, when the lengths, thicknesses, and angle values of the branches are altered, extensional changes occur in its mechanical properties.

It is revealed as a result of studies that when the angle values between its branches are changed, the Poisson ratio of the structure can be varied as negative, zero, or positive. The comprehensive literature review of Re-Entrant lattice structure is given in Table 9.

Table 9. Mechanical properties of Re-Entrant lattice structure produced from various materials.

Lattice Type	Production Method	Material	Mechanical Properties			Test Standard	Reference
			υ	E (MPa)	σ (MPa)		
Re-Entrant	FDM	PLA	-0.89	31.95	0.5	-	[36]
Re-Entrant	FDM	ABS	-	10.78	0.88	ASTM C393/C393M-06	[37]
Re-Entrant	Polyjet	Filaflex	-0.23	0.6	-	-	[38]
Re-Entrant	Polyjet	VeroWhite	-0.6	22.5	3	ASTM D695	[39]
Re-Entrant	Polyjet	VeroWhite	-0.4	5	-	-	[40]
Re-Entrant	Polyjet	A digital material DM9760	-0.25	-	0.01	-	[41]
Re-Entrant	SLM	AlSi10Mg	0.44	-	0.55	-	[42]
Re-Entrant	SLM	AlSi10Mg	-0.15	-	0.28	-	[43]

Re-Entrant	SLM	Al Alloy	-1	700	32.5	-	[44]
Re-Entrant	SLM	Al Alloy	-0.5	5000	10	-	[45]
Re-Entrant	SLM	Ti6Al4V	-0.8	-	220	-	[46]
Re-Entrant	SLM / EDM	Ti6Al4V	-0.18	900	80	ASTM F3001/ISO 13314:2011	[47]
Re-Entrant	SLM	304 Stainless Steel	-0.8	117.6	-	-	[15]
Re-Entrant	SLM	Stainless Steel / Nickel	–2.41	-	-	-	[48]
Re-Entrant	SLA / Casting	Al+Epoxy	-1.01	1400	22.2	-	[49]
Re-Entrant	SLA / Wire cut	Al+Epoxy	-0.2	-	0.2	-	[50]
Re-Entrant	SLA / Casting	Al + Resin	-1.18	175	22	-	[51]

2.4.3.2 Arrowhead Geometry

Arrowhead geometry is a very rare lattice structure in literature. It occurs as a consequence of two V geometries gathering at different angles and configurations. Therefore, it is also called double V geometry. It exhibits high strength values under

compressional loads. It generally exhibits a negative Poisson's ratio due to its concave branch structure. The research articles that aspired to the investigation of Arrowhead lattice structure are listed in Table 10.

Table 10. Mechanical properties of Arrowhead lattice structure produced from various materials.

Lattice Type	Production Method	Material	Mechanical Properties			Test Standard	Reference
			υ	E (MPa)	σ (MPa)		
Arrowhead	FDM	ABS	-0.75	440	32.2	-	[52]
Arrowhead	SLA	ABS	-1	5	-	-	[53]
Arrowhead	SLA / Casting	Al + Resin	-1.73	-	12.5	-	[54]
Arrowhead	SLM	316L Stainless Steel	-1.75	100	850	ASTM E8/ASTM E8M-16a	[24]
Arrowhead	Laser Welding	Steel	-1.25	400	120	-	[55]

2.4.3.3 Star Geometry

Another rare lattice structure is star geometry which has substantially exhibits similar properties with the re-entrant geometry. It consists of eight ligaments, and each unit cell is composed of four parallel ligament groups. Each unit cell has four internal and external angles. All ligaments have the same inner angle, which may be represented as Q1. On the other hand, Q2 represents the outside angle of ligaments. Moreover, in the internal structure of the unit cell, ligaments are coincident with each other from two different spots and they have exactly the same length. It mostly exhibits a negative

Poisson's ratio due to its concave ligament structure. The studies about examination of star shaped lattice structure are given in Table 11.

Table 11. Mechanical properties of Star lattice structure produced from various materials.

Lattice Type	Production Method	Material	Mechanical Properties			Test Standard	Reference
			υ	E (MPa)	σ (MPa)		
Star	SLA / Casting	Aluminum alloy 6061O	-0.38	-	8.5	-	[56]
Star	SLA	Acrylic	–0.53	-	-	-	[57]
Star	Analytical Approach	ABS	–0.56	360	-	-	[58]

2.4.3.4 Chiral Geometry

The chiral structure has the most complex geometry among lattice structures. This lattice structure can consist of multiple geometries under the same structure provided that one of the geometries it contains is a circle, and the other geometry can be any desired mesh geometry. Different orientations can be formed according to the variety of geometries it contains, and each of these orientations exhibits different mechanical properties. Tri-chiral, Anti-Trichiral, Tetra-Chiral, and Anti-Tetrachiral lattice geometries are the most common Chiral geometry orientations. It exhibits high strength values under compression forces. Poisson's ratio varies for every different orientation of this structure. The literature review of Chiral lattice structure is given in Table 12.

Table 12. Mechanical properties of various Chiral lattice structures produced from different materials.

Lattice Type	Production Method	Material	Mechanical Properties			Test Standard	Reference
			v	E (MPa)	σ (MPa)		
Anti-Trichiral	FDM	ABS	-0.5	-	0.2	-	[59]
Anti-Trichiral	FDM	ABS	-0.25	-	0.08	-	[60]
Anti-Trichiral	FDM	TPU	-0.55	-	400	ASTM D638/ASTM E8	[61]
Tetra-Chiral	FDM	ABS	0.26	0.94	-	-	[62]
Tetra-Chiral	SLA	UV Curable Resin	–0.94	0.63	-	-	[63]
Anti-Tetra-Chiral	SLS / SLM	AlSi10Mg	-0.93	839.55	-	ASTM D638	[64]
Anti-Tetra-Chiral	Laser Cutting	SUS304 steel	−1.04	-	225.21	-	[65]
Chiral	EBM	Ti6Al4V	0.3	120	1300	-	[66]

2.4.4 Auxetic Materials

Materials with a negative Poisson's ratio is known as auxetic materials. Negative Poisson's ratio values result from geometrical form and are still in the development phase with enhanced production systems. Auxetic materials are becoming more popular as a result of their various beneficial unique characteristics, such as shape memory applications, energy absorption fields, and vibration control critical structures. K. E. Evans created the name "auxetics" from the Greek word "auxetos," which meaning "that may be expanded" [67]. Auxetic materials may be found in a range of forms, including micro and macro structures. Based on deformation mechanism, these structures can be categorized into three groups: A) re-entrant type; B) chiral type; C) rotating (semi-) rigid structures.

Re-entrant basically advert to something that will direct to inward which exactly having a negative angle. Re-entrant shape is illustrated in Figure 7.2.b. The most of the literature reviews have focused on the re-entrant type auxetic structures. Poisson's ratio characteristics of re-entrant structures highly depend on the angle between unit cell ligaments.

A typical chiral shaped auxetic unit cell represents a central circular, or cylindrical unit with tangentially merged ribs and/or ligaments. The principal mechanism of chiral structures is rotating under mechanical loadings, and then supporting ribs stretches or contracts. Chiral structures have also rotational symmetry. Opposite to re-entrant structures, chiral structure Poisson's ratio does not depend on the angle between sub-units. Increasing the number of supporting ribs per circular center unit may increase the stiffness of the whole structure assembly. Figure 7 could give better understanding of the conventional and auxetic structure shapes.

Figure 7. Conventional and auxetic metamaterial structure shapes: 1-) Lattice structures with positive Poisson ratio; (a) Kagome lattice structure; (b) Diamond lattice structure; (c) Honeycomb lattice structure; (d) Square lattice structure; (e) Triangular lattice structure; 2-) Lattice structures with negative Poisson ratio; (a) Arrowhead lattice structure; (b) Re-entrant lattice structure; (c) Star lattice structure; (d) Tetra-chiral lattice structure; (e) Tri-chiral lattice structure.

Rotating semi-rigid structures will be the last category of the auxetic structures in terms of deformation mechanisms. Simplified rotating structure includes rigid squares or circles moving through the load vector applied on the body. While loaded in tensile or compression directions, these structures will be responded as either in expansion or contraction. Beyond the novel mechanical characteristics of auxetic materials like vibration damping, compression and tensile resistance; indentation resistance is also another gaining point. Auxetic materials provide more resistance to indent than other materials with lower plastic deformation. Figure 8 shows that the auxetic material is more likely to flow towards to indentation point, and other materials tend to avoid from the load applied.
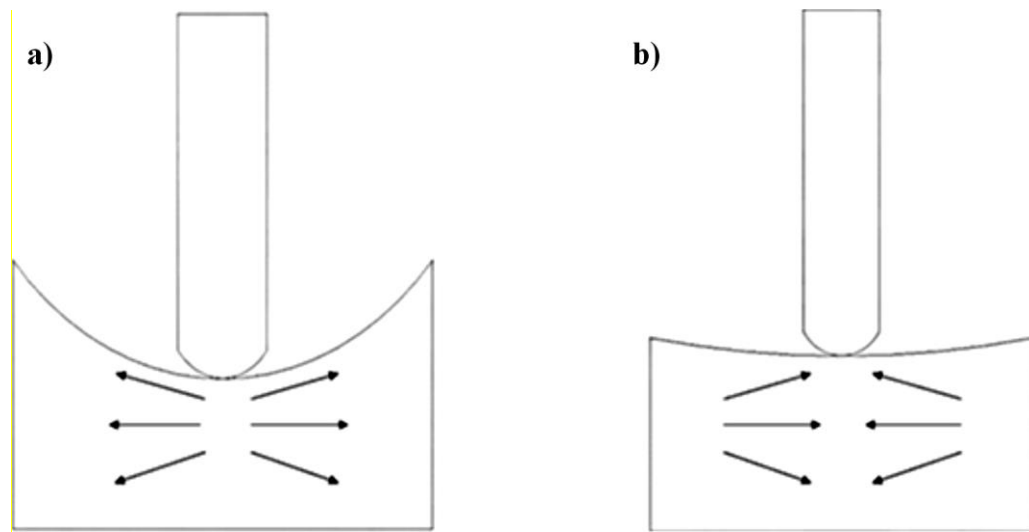
Figure 8. Indentation behaviour of nonauxetic and auxetic materials: (a) Non-auxetic structure; (b) Auxetic structure

In conventional materials, material density decreases just below the impact point affected by the sinking load. In other words, the material in this area spreads around due to the positive Poisson's ratio. In auxetic materials, this situation will be the opposite, since they have a negative Poisson's ratio.

In other words, material density will increase in the part just below the impact point where the load affects. Due to the increase in density in this region, the hardness of the material will increase and consequently the sinking resistance will also increase [68].

2.4.4.1 The History of Auxetic Materials

Despite the fact that worldwide breakthroughs in auxetic materials were more obvious in the 1990s, Roderick Lakes was the first to employ NPR in metallic structures in his work [69]. In the early 1900s, researcher Voigt identified a material with a negative Poisson Ratio in his experimentation specimen with a Poisson Ratio of -0.14. In his research, he discovered that when material is stretched sideways, they expand in the same direction. Voigt could not explain this phenomenon and could not foresee any applications for this property, therefore it was neglected for decades.

Auxetic materials have been used for various engineering applications. For instance, they have a place in engineering materials which are commonly used in packaging, transportation, heat sinks, electrical and electronical equipment's, automotive industry, biomedical, and aerospace engineering applications. Specifically, auxetic chiral structures can be used to prototype morphing wings, and also can be used in composite aero structures designs due to the fact that they show higher shear resistance. Since metals are much heavier than auxiliary composites and auxiliary composites have a higher strength-to-weight ratio than metals, they are more preferred in the aviation industry. Furthermore, auxiliary materials can be used in aviation applications such as thermal protection and noise cancellation applications of turbine engines [69].

Although auxetic materials have been known for more than 100 years, researchers have attracted more attention again since the early 1990s. Until today, many different auxetic materials have been produced such as polymers, metals, ceramics, composites, coatings and fibers. Figure 9 shows the historical development of the number of publications on auxetic materials.
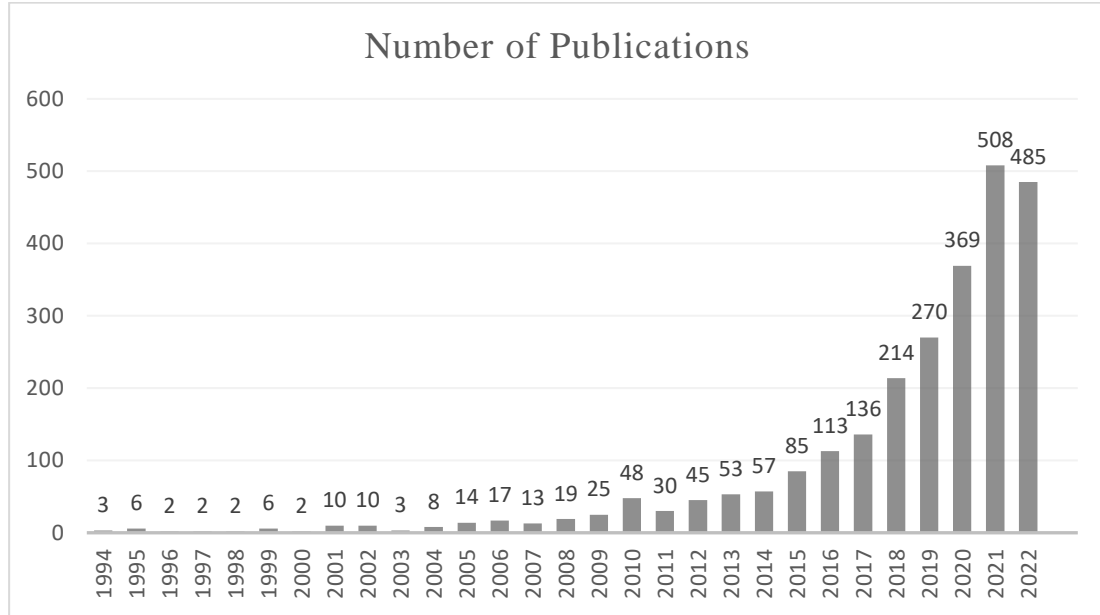
Figure 9. Annual number of publications on auxetic materials published in Web of Science from January 1994 to August 2022.

2.4.4.2 Application Fields of Auxetic Materials

Developments in engineering design, new material research, and manufacturing technique refinement all contribute to new improvements in a variety of fields. One of the primary incentives for advances in engineering research is the health of humans and other living creatures. This thesis summarizes auxetic structure advances, and innovative auxetic structure design. Auxetic structure uses are classified into several groups. However, sports applications and medical & biological applications are chosen as significant issues of application areas of auxetic structures within the subject.

2.4.4.2.1   Biomedical Applications

The negative Poisson ratio is the most essential characteristic of auxetics. Some medical applications require the ability to grow in cross section while stretching and shrink in cross section while compressing. Some surgical operations are effective as a result of auxetic conduct. Human veins, for example, might lose function due to aging and other health issues. As a result, a mechanism that may provide resistance to vein walls against a decrease in vein cross section area must be devised; hence, stent application is one of the most prominent medical applications that exhibits auxetic behavior. Bhullar et al., studied on rotating semi structures, which is a one of the major types of auxetics, for medical stent applications.

Another popular topic in research domains is tissue engineering. Instead of human skin, composite structured auxetics can be employed to generate nonlinear stress-strain interactions. This biological inspiration may be accomplished through the hierarchical layering of auxetics. Furthermore, Evans and Alderson stated that artificial blood veins can be produced in the shape of an auxetic structure to prevent deceleration [70].

2.4.4.2.2   Sports Applications

The human body is vulnerable to the effects of outsourcing. The human head is the most susceptible component, as any contact to the head can result in serious harm or death. Helmets are meant to safeguard human health during sporting events under these scenarios.

Traumatic Brain Injury (TBI) is the most frequent serious injury caused by head strikes. The significance of brain damage is determined mostly by the sport type. Cycling, motor racing, alpine sports, and American football, for example, are all subject to head injuries. Furthermore, projectile-based sports such as ice hockey, baseball, and cricket have a high risk of head and facial injuries.

The most critical protective equipment against serious brain damage are head covering accessories, hence helmet design and engineering are critical to human health. Auxetic materials have the potential to be used as the fundamental structure of protective equipment like helmets. There are additional parameters for professional athlete accessory design. The performance of equipment is an essential technical constraint, since everyone strives to avoid additional weights in order to attain higher mobility. Auxetic structures can be an excellent option for providing both energy absorption and minimal weight. Auxetic materials, like those used in sports, have grown in relevance in this subject in terms of preserving human safety and health. With the high stiffness rate per unit mass provided by auxetic materials, it is conceivable to replace existing materials and designs.

2.5   Aim of the Study

The aim of this study is to investigate the microstructural and mechanical properties of the lattice geometries pursuant to their porous geometries which are known as unit cells, dimensions, and ligament positions under compressional and tensional loads. In the study, elastic modulus, Poisson's ratio, and tensile strength values of structures that are additively manufactured from two specific lattice geometry are examined. In the study, PLA and Titanium powders are used as a raw material to be able to manufacture the specimens. The relative density was manually calculated via Archimedes Principle and compared to literature data. Fourier-transform infrared spectroscopy (FTIR), scanning electron microscopy (SEM), X-ray Diffraction (XRD) analysis was used to define the microstructural characteristics of the additively manufactured specimens. The mechanical properties of the specimens were investigated through diametral tensile & compression and Vickers microhardness tests.

CHAPTER 3

3. MATERIALS AND METHODS

3.1   Creation of Design

It is aimed to design a novel auxetic structure within the scope of this thesis. Considering the studies in the literature, various geometries such as Re-entrant, Honeycomb and Star were examined, and the mechanical properties of these structures inspired the unit cell geometries. In this context, two different unit cells are conducted. First unit cell is obtained with configuration of the re-entrant structure. On the other hand, second unit cell is constituted from the combination of the re-entrant, star and honeycomb structures. Auxetic behavior is expected from these unit cells and their multiplied sandwich structures. Experimental procedure can be summarized into two main parts as shown in Figure 10.
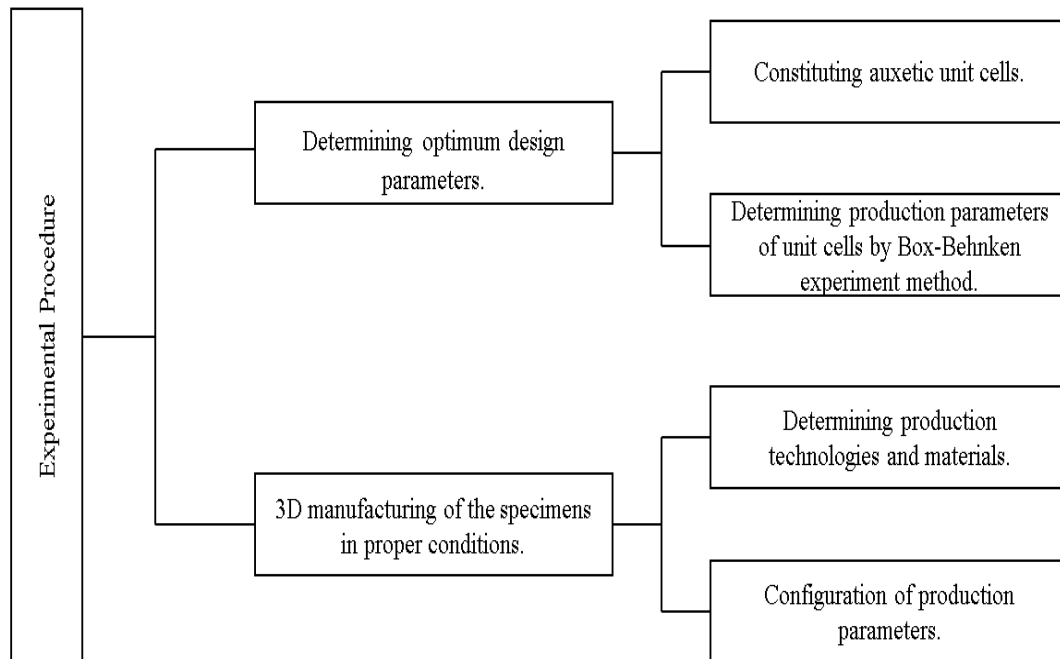
Figure 10. Schematic demonstration of experimental procedure.

3.1.1   Design Parameters of Novel Auxetic Structures Design

The unit cells to be created within the scope of this study were formed first, respectively, and three-dimensional plate structures were obtained by mirroring and deriving the formed unit cells with sequentially sequencing. The primary purpose of the novel auxetic structures constituted is to contribute to the existing models in the literature with a new design. It was stated that the novel three-dimensional structures created showed enhanced mechanical properties. In addition, the mechanical properties of the created models were tried to be superior by changing design parameters, and the missing or open-to-development aspects were identified in order to inspire future studies.

As mentioned before, the first original shape was created by combining re-entrant geometry with different configurations while second unit cell is constituted from the combination of the re-entrant, star and octagonal structures. Representative views of novel structures are shown in Figure 11.
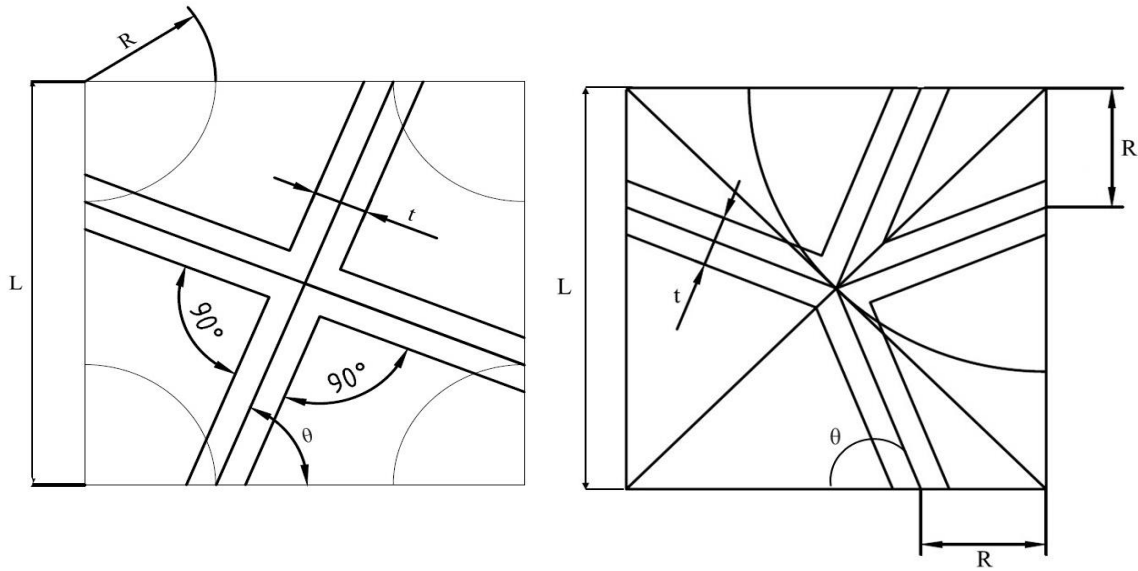
Figure 11. Novel auxetic unit cells.

Within the scope of the thesis, the basic parametric geometrical changes are applied on default novel design. The parameters can be listed as: side length of square cross section (L), thickness of ligament (t), distance between the corner of the square and the center point of the ligament (R), and angle of the inner structures (θ).

Within the context of this study, it was stated that enhancing mechanical characteristics of the structures is possible with the variation of dimensional properties. In other words, given dimensions are the parameters to be changed for having an idea how mechanical design respond to any geometrical changes. At this point, given parameters were selected to obtain different geometric configurations except R which is given in default novel unit cells as 11.9 mm and changes according to alteration of other parameters. In a scenario where each parameter can take three different values in itself, it is desired to obtain geometries in various configurations with combinations of different values. However, the situation that a configuration to be created in this context requires the production of 84 pieces of samples for each shape, necessitating the use of an alternative test design method. Experimental design methods should be applied to reduce the number of samples produced and the number of tests / analyses performed. The number of test samples to be produced in cases where the test design is applied or not is given in Table 13.

Table 13. The number of the samples with / without experimental methods.

Variables		Unit cell A	Unit cell B	Total
With experimental methods	PLA based tensile specimens	15	15	30
	PLA based compression specimens	15	15	30
	Ti6Al4V based tensile specimens	15	15	30
	Ti6Al4V based compression specimens	15	15	30
	Total Number	60	60	120
Without experimental methods	PLA based tensile specimens	84	84	168
	PLA based compression specimens	84	84	168
	Ti6Al4V based tensile specimens	84	84	168
	Ti6Al4V based compression specimens	84	84	168
	Total Number	336	336	672

In this context, statistical experimental design method is studied which is called as ''Box-Behnken Design of Experiment''. In Box-Behnken method, each factor, or independent variable, is placed at one of three equally spaced values, usually coded as −1, 0, +1 [71]. The representations of the geometric parameters which embed in the Box Behnken design of experiment are given in Table 14.

Table 14. Box Behnken design of experiment parameters.

Parameter & Variable			1	0	-1
Length of Geometry (L) (mm)			40	35	30
Layer Angle (θ) (degree)			75˚	68˚	61˚
Layer Thickness (t) (mm)			1.5	1	0.5
Box Behnken Design of Experiment Draft Version				Box Behnken Design of Experiment with Unit Cells Parameters			
	Factors				Factors		
Runs	Layer Thickness	Layer Angle	Length of Geometry	Runs	Layer Thickness	Layer Angle	Length of Geometry
1	-1	-1	0	1	0.5	61˚	35
2	-1	1	0	2	0.5	75˚	35
3	1	-1	0	3	1.5	61˚	35
4	1	1	0	4	1.5	75˚	35
5	-1	0	-1	5	0.5	68˚	30
6	-1	0	1	6	0.5	68˚	40
7	1	0	-1	7	1.5	68˚	30
8	1	0	1	8	1.5	68˚	40
9	0	-1	-1	9	1	61˚	30
10	0	-1	1	10	1	61˚	40
11	0	1	-1	11	1	75˚	30
12	0	1	1	12	1	75˚	40
13	0	0	0	13	1	68˚	35
14	0	0	0	14	1	68˚	35
15	0	0	0	15	1	68˚	35

As can be seen in Table 14, there are 13 different designs that are created by changing three different parameters which are length of the geometry, layer thickness, and layer angle. All other design dimensions are hold as same value while preserving geometric integrity of novel the unit cells. These parameters are for 2D plane dimensions; additional thickness dimension for making design 3D is vary according to specimen type. Design of experiment codes for both tensile and compression samples are shown in Table 15.

Table 15. Design of experiment codes for both tensile and compression samples.

Design of Experiment Codes for Unit Cell within Re-entrant Structure				Design of Experiment Codes for Unit Cell within Re-entrant, Star and Octagonal Structure			
Specimens	Unit cell parameters			Specimens	Unit cell parameters		
	L (mm)	t (mm)	θ (º)		L (mm)	t (mm)	θ (º)
R-L35T05θ61	35	0.5	61	RSO-L35T05θ61	35	0.5	61
R-L35T05θ75	35	0.5	75	RSO-L35T05θ75	35	0.5	75
R-L35T15θ61	35	1.5	61	RSO-L35T15θ61	35	1.5	61
R-L35T15θ75	35	1.5	75	RSO-L35T15θ75	35	1.5	75
R-L30T05θ68	30	0.5	68	RSO-L30T05θ68	30	0.5	68
R-L40T05θ68	40	0.5	68	RSO-L40T05θ68	40	0.5	68
R-L30T15θ68	30	1.5	68	RSO-L30T15θ68	30	1.5	68
R-L40T15θ68	40	1.5	68	RSO-L40T15θ68	40	1.5	68
R-L30T10θ61	30	1	61	RSO-L30T10θ61	30	1	61
R-L40T10θ61	40	1	61	RSO-L40T10θ61	40	1	61
R-L30T10θ75	30	1	75	RSO-L30T10θ75	30	1	75
R-L40T10θ75	40	1	75	RSO-L40T10θ75	40	1	75
R-L35T10θ68	35	1	68	RSO-L35T10θ68	35	1	68
R-L35T10θ68	35	1	68	RSO-L35T10θ68	35	1	68
R-L35T10θ68	35	1	68	RSO-L35T10θ68	35	1	68

First unit cell is coded by R letter due to the fact that it is created by combining re-entrant geometry with different configurations. On the other hand, second unit cell is indicated by RSO letters which is constituted from the combination of the re-entrant, star and octagonal structures.

3.1.2 Sandwich Structures of Auxetic Unit Cells

In the original auxetic design that is planned to be used in real life must be included in the sandwich structure. In this context, the unit cell has been periodically reproduced on two axes and supported by plates that will form the sandwich structure. The replication schemes of two different unit cells and the final sandwich structures are shown in Figure 12. All design variations are repeated in sandwich structure form.
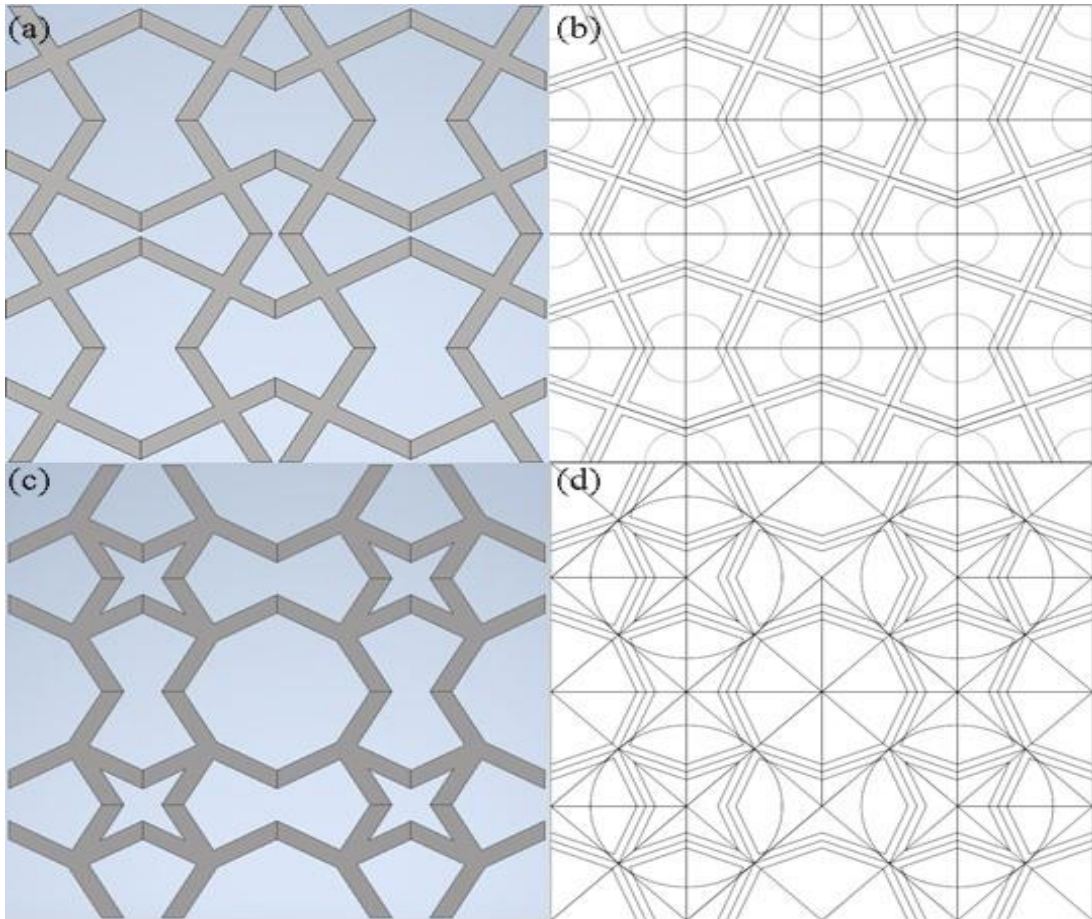
Figure 12. Novel auxetic sandwich structures; (a) 3D sandwich structure form of first novel unit cell; (b) 2D sandwich structure form of first novel unit cell; (c) 3D sandwich structure form of second novel unit cell; (d) 2D sandwich structure form of second novel unit cell;

From the perspective of design, through the innovative unique cell design is achieved using re-entrant, star and honeycomb mechanisms. In this thesis, tensile and

compression displacements were applied each novel geometries and orientations, respectively. Extension versus deformation change was also illustrated. Furthermore, different impact velocities were applied from the upper bodies of sandwich structures to evaluate deformation mechanisms and stress distributions. Experimental and numerical analyses results are shared through the upcoming sections.

3.2   Material Selection and Production Parameters

The ''Filameon'' branded PLA filament and Ti Alloy, Ti6Al4V (Grade 5 ELI ASTM B265-10), were selected as the production materials due to their widespread use in additive manufacturing area. General properties of PLA filament and Ti6Al4V metal powders are represented in Table 16.

Table 16. General properties of PLA filament used in this thesis.

Filameon PLA Filament		
Diameters and Tolerances	The length of 1 kg filament (m)	335 ± 5
	Tolerance (mm)	0.04
Processing Guide	Heated bed temperature (°C)	60 (Optional)
	Nozzle Temperature (°C)	190 – 230
Physical Properties	Melt Flow Rate (g/10min)	6.0g (210 °C / 2.16 Kg)
	Density (g/ cm^3)	1.24
Mechanical Properties	Yield Strength (MPa)	53
	Tensile Elongation (%)	6
	Flexural Strength (MPa)	83
	Rockwell Hardness (R-scale)	108
	Poisson's Ratio	0.35

On the other hand, Ti-based tensile samples were prepared by melting the Ti6Al4V powders via EBM method. Both of the Titanium and PLA based tension samples were manufactured according to ASTM D638-1 standard with the dimensions of 165 x 19 x 3.2 mm^3. Similarly, the preparation of compression samples was carried out with the dimensions of 40 x 40 x 32 mm^3 according to ASTM D695. General composition of Ti6Al4V metal powders is represented in Table 17.

Table 17. Nominal chemical composition of Ti6Al4V titanium alloy in weight percentage.

Weight %	Ti	C	Fe	N	Al	O	V	H	Other
Ti6Al4V	Bal	0.08	0.03	0.05	5.5 – 6.75	0.20	3.5 - 4.5	0.015	0.40

3.2.1 Manufacturing of Tensile Specimens

In this study, both of the PLA and Ti6Al4V based tensile specimens were manufactured through AM process. Test specimens were designed according to ASTM-D638 –Type 1 standart with SOLIDWORKS 2020 that is a computer-aided design program. After the test samples are designed, they are converted to STL file format via the CAD program and transferred to the G-Code program designed for the 3D printers. In this study, Creality Slicer 6.8.2 was used as the G-Code program to produce PLA-based samples. With this program, as shown in Figure 13, where the print will be located on the platform, on which edge of the piece the print will be built, and production parameters are selected.
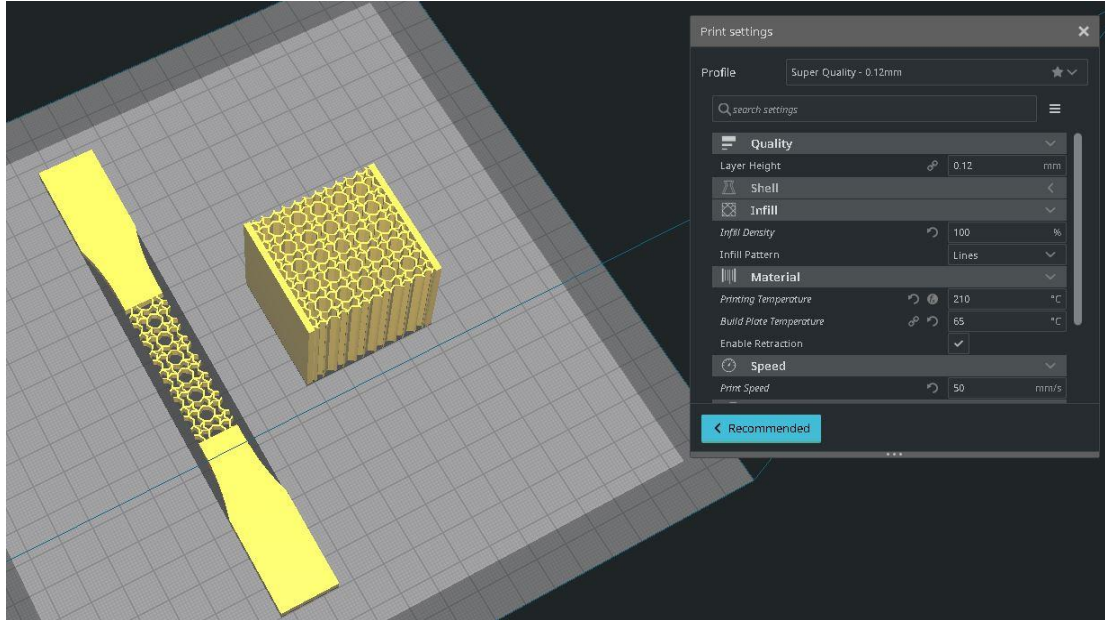
Figure 13. Interface view of Creality Slicer 6.8.2.

As mentioned before, 15 different PLA-based specimens were prepared for each novel unit cell. Although the production of each sample varies depending on the variety of unit cell structures they have, the production of each sample exiled an average of 1.5 hours. Table 18 shows the production parameters given for the samples produced with the Ender 3 V2 model printer.

Table 18. 3D manufacturing parameters of PLA based samples

Material	Layer Height	Infill Density	Printing Temperature	Build Bed Temperature	Print Speed
PLA	0.12 mm	100 %	210 °C	65 °C	50 mm/s

Real life and 3D CAD design images of PLA-based tensile specimens produced using two different novel unit cell within the scope of this thesis are shown in Figure 14.
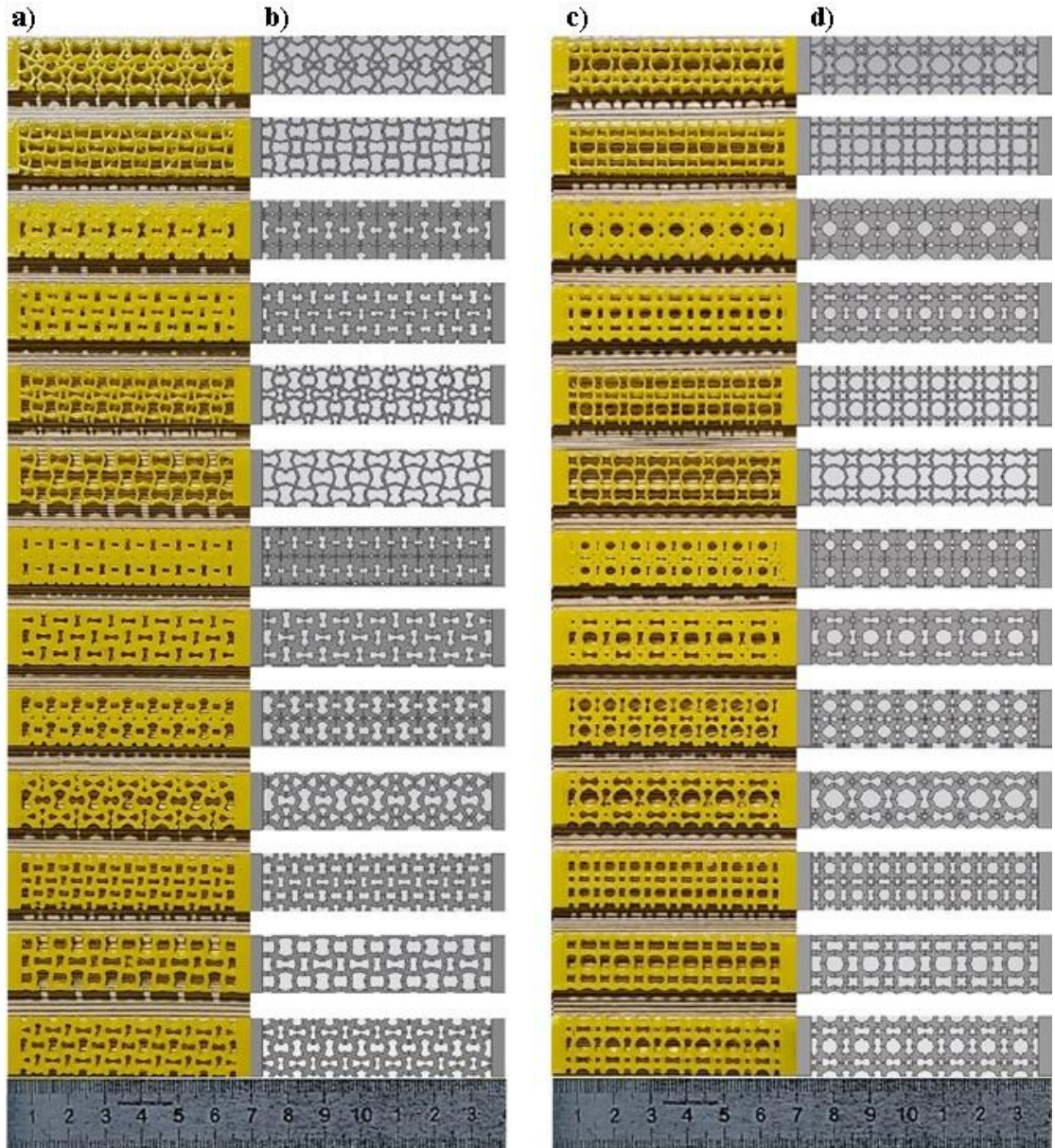
Figure 14. Representation of PLA-based tensile specimens; (a) 3D printed samples of first unit cell which is conducted by re-entrant geometry; (b) 3D CAD designs of first unit cell which is conducted by re-entrant geometry; (c) 3D printed samples of second unit cell which is conducted by re-entrant, star and octagonal geometry; (d) 3D CAD designs of second unit cell which is conducted by re-entrant, star and octagonal geometry.
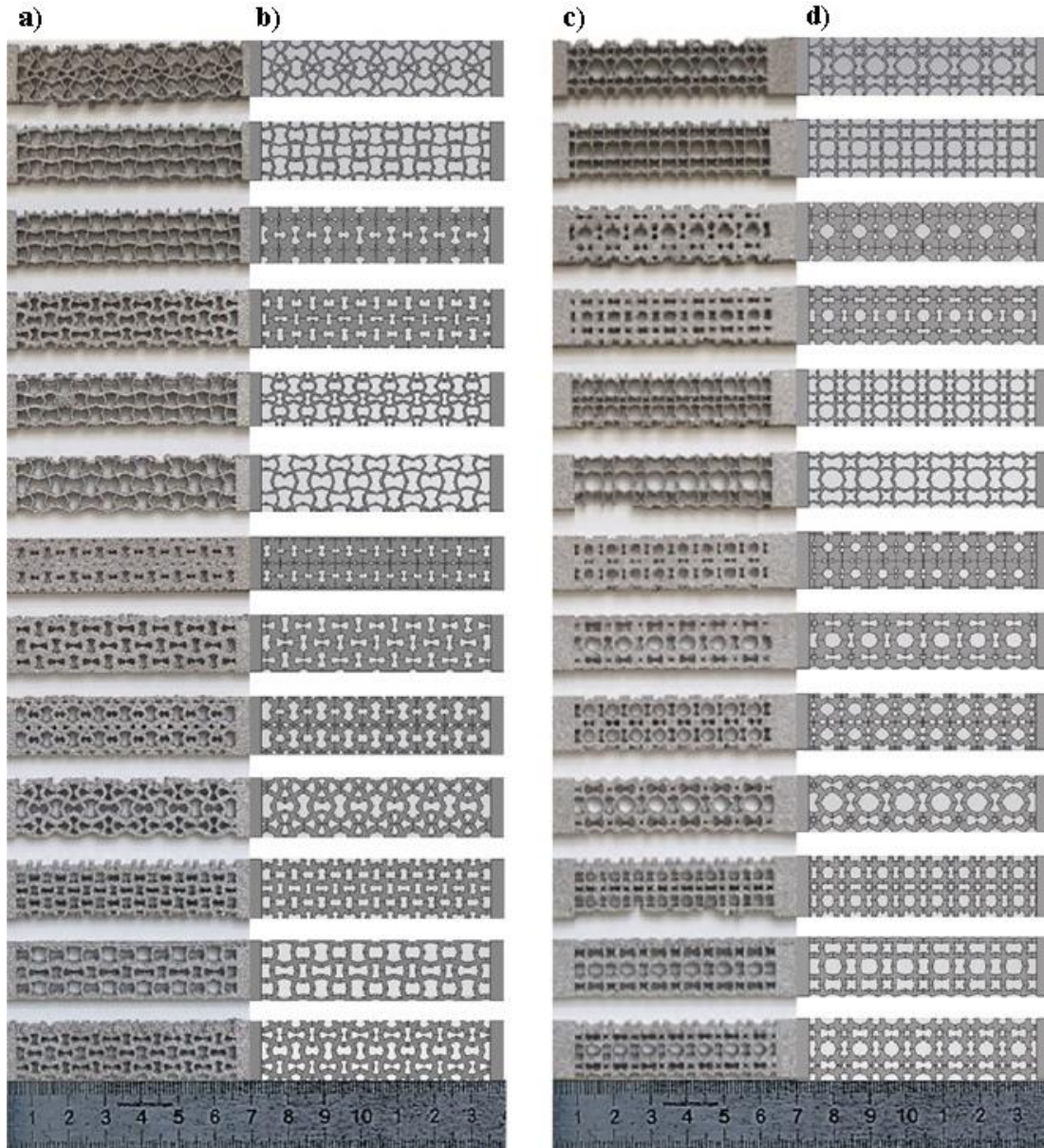
Figure 15. Representation of Ti6Al4V-based tensile specimens; (a) 3D printed samples of first unit cell which is conducted by re-entrant geometry; (b) 3D CAD designs of first unit cell which is conducted by re-entrant geometry; (c) 3D printed samples of second unit cell which is conducted by re-entrant, star and octagonal geometry; (d) 3D CAD designs of second unit cell which is conducted by re-entrant, star and octagonal geometry.

In addition to the production of PLA-based samples, Ti6Al4V-based tensile specimens were also produced within the scope of this study. The manufacturing of the samples was carried out on the GE ARCAM Q20 branded 3D printer under favor of EBM technology. Real life and 3D CAD design images of Ti6Al4V-based specimens are shown in Figure 15.

3.2.2 Manufacturing of Compression Specimens

Within the scope of this study, it is also aimed to examine the reactions of two different unit cells designed in a unique way under compressional load. In this context, both PLA and Ti6Al4V based compression specimens were produced. The samples were designed based on the ASTM D695 standard. Production of PLA-based specimens was carried out in Ender 3 V2 branded 3D printer within FDM method. On the other hand, production of Ti6Al4V-based samples was manufactured in the GE ARCAM Q20 branded 3D printer. 3D CAD design and real-life images of the produced samples are given in Figure 16 and Figure 17.
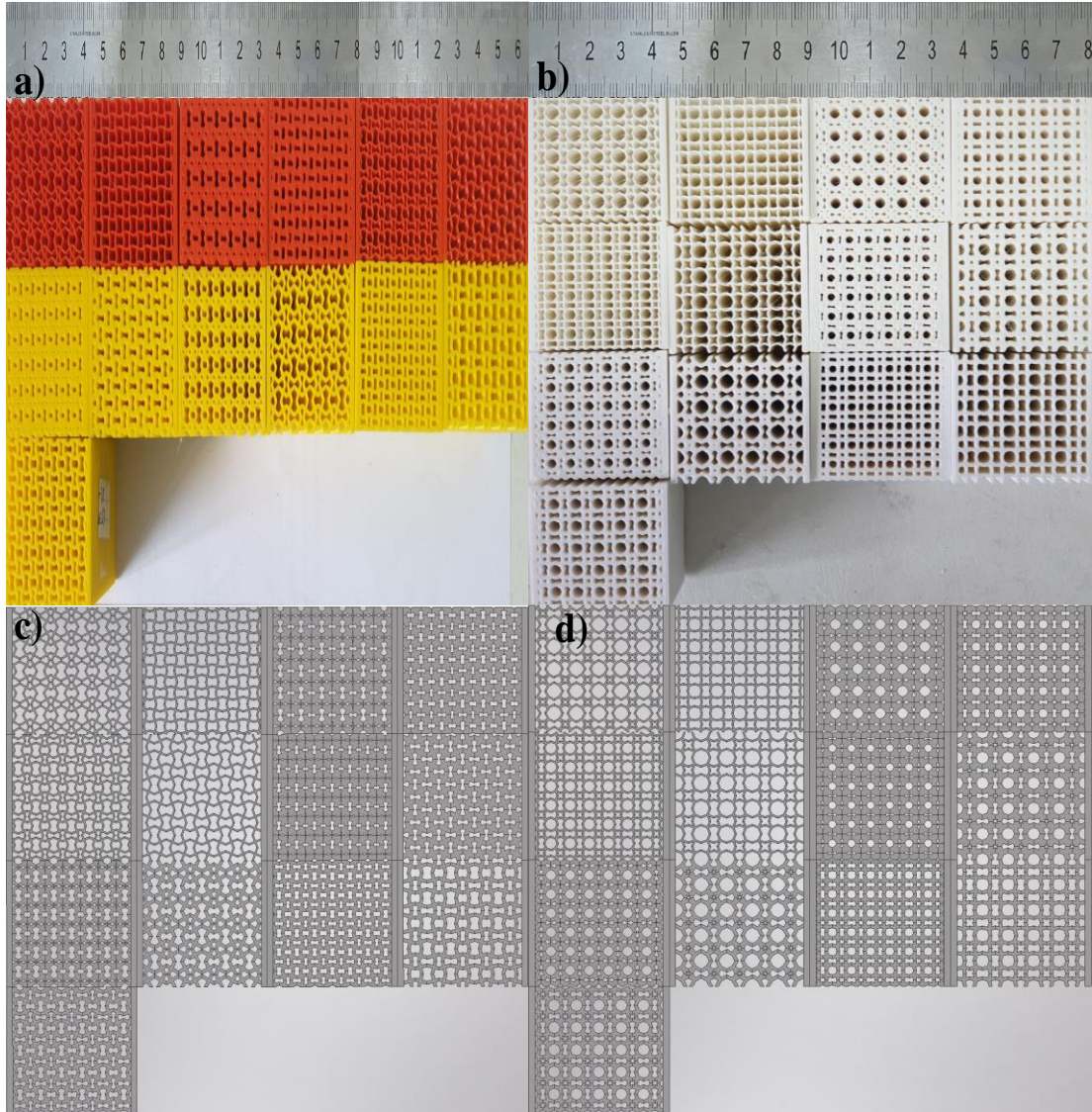
Figure 16. Representation of PLA-based compression specimens; (a) 3D printed samples of first unit cell which is conducted by re-entrant geometry; (b) 3D CAD designs of first unit cell which is conducted by re-entrant geometry; (c) 3D printed samples of second unit cell which is conducted by re-entrant, star and octagonal geometry; (d) 3D CAD designs of second unit cell which is conducted by re-entrant, star and octagonal geometry.
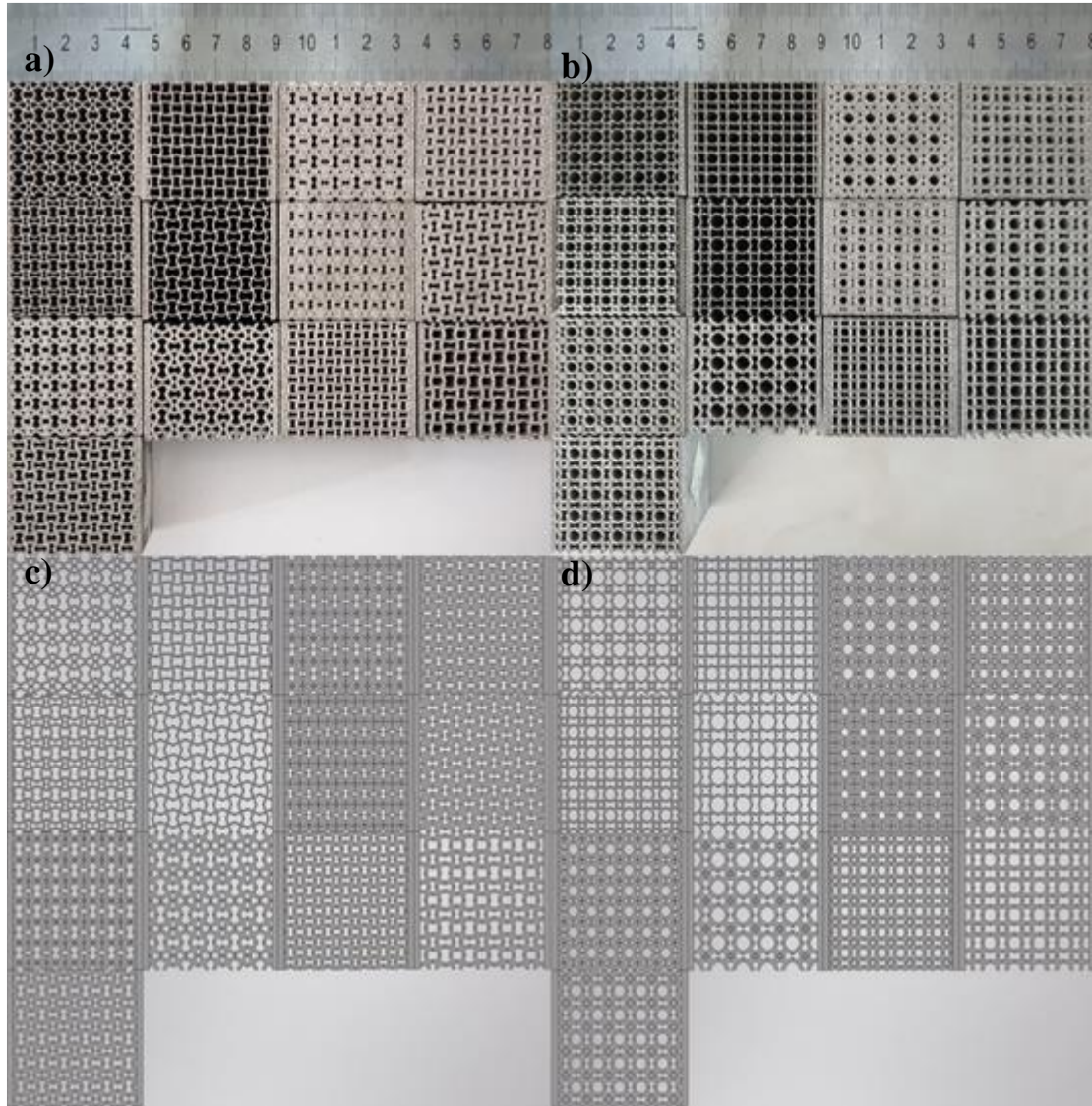
Figure 17. Representation of Ti6Al4V-based compression specimens; (a) 3D printed samples of first unit cell which is conducted by re-entrant geometry; (b) 3D CAD designs of first unit cell which is conducted by re-entrant geometry; (c) 3D printed samples of second un unit cell which is conducted by re-entrant, star and octagonal geometry; (d) 3D CAD designs of second unit cell which is conducted by re-entrant, star and octagonal geometry.

3.3 Mechanical Tests, Characterization Processes of Specimens

3.3.1 Tension and Compression Experiments of Specimens

There are two international standards for the tensile testing of materials. One of them is ISO-527 and the other is ASTM-D638. These standards are similar in terms of finding technical specifications. However, the test speed of the standards and sample sizes may differ. Therefore, results from the two standards might not match exactly. ASTM-D638 test standard was used within the context of this thesis. Specimens were prepared based on the Type-1 form of the ASTM-D638. The dimensions of the sample according to ASTM-D638—Type-1 are given in Figure 18.
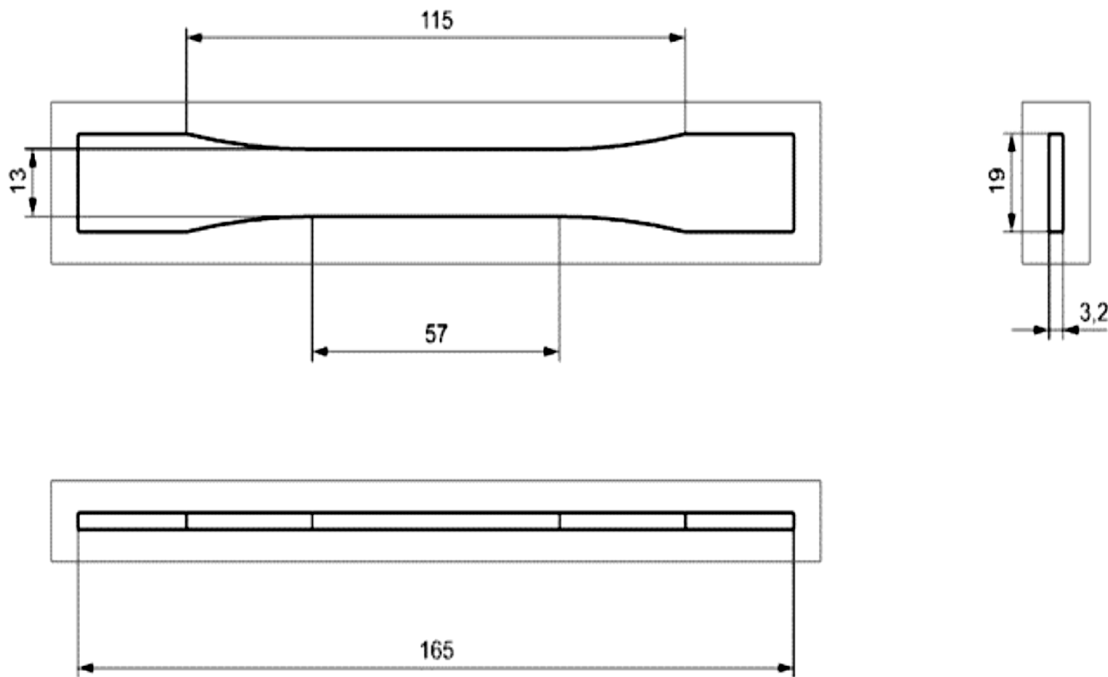
Figure 18. ASTM-D638—Type-1 sample dimensions.

On the other hand, compression specimens were created out on 40x40x40 mm3 cubic samples in accordance with ASTM-D695. The tensile and compressive strength tests in this study were conducted on the testing device which can generate 50 kN tensional and compressional force on the sample. Testing machine is shown in Figure 19.
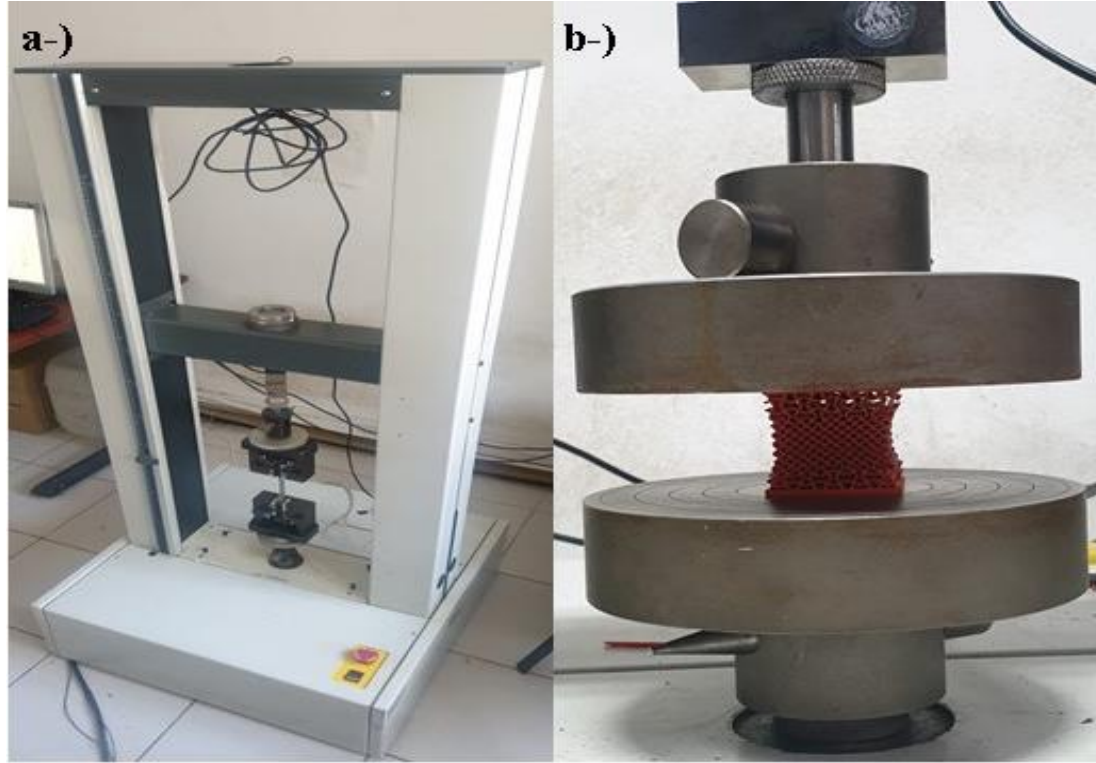
Figure 19. (a) Tensile testing machine used in experimentation; (b) Demonstration of the compression test of the specimen.

Three separate sample are manufactured for each PLA-based unit cell design with different parameters to increase validity of experiments. Therefore, 360 different sample were produced and tested for both tension and compression specimens. However, for the Ti6Al4V-based specimens only one sample is manufactured and tested due to the lack of technical equipment's.

3.3.2 Characterization Processes of Specimens

In order to obtain information about the properties of samples, analysis was performed as summarized in Figure 20.
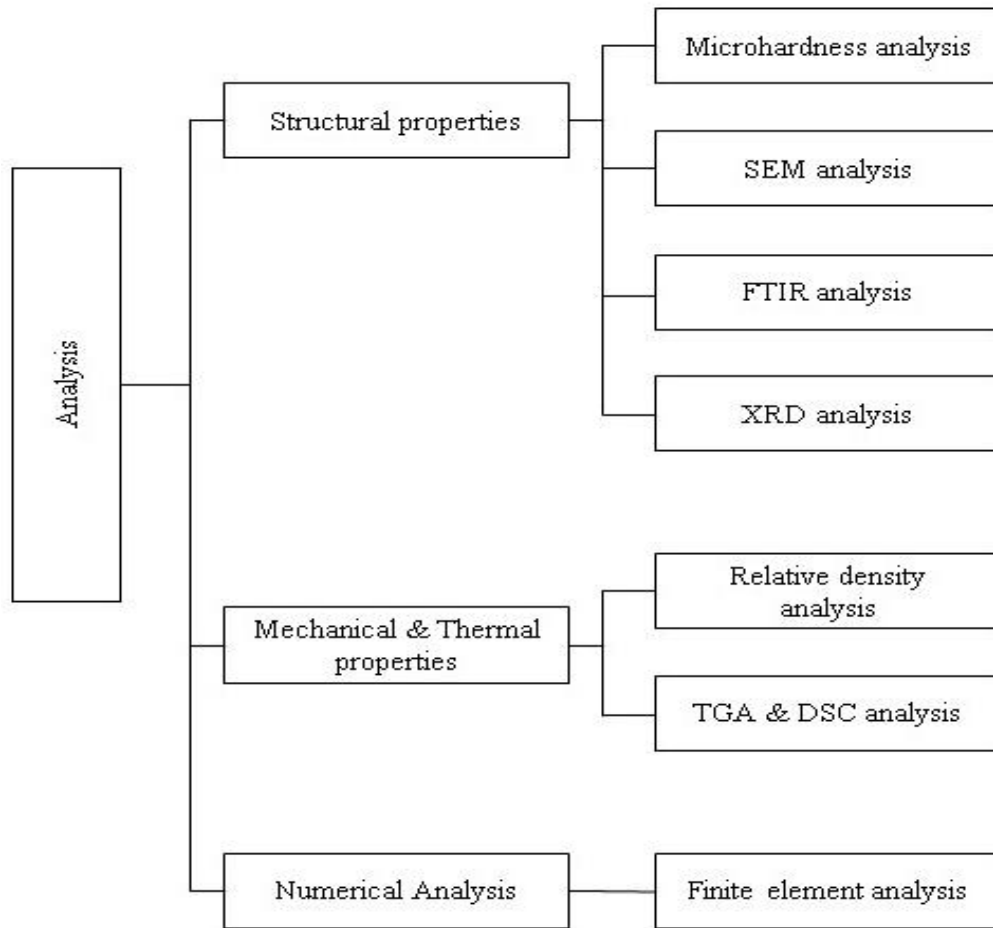
Figure 20. Summary of analysis performed.

3.3.2.1 Structural Properties

3.3.2.1.1 Microhardness Analysis

Vickers Microhardness tests of the samples were conducted by a microhardness tester (HMV-2, Shimadzu, Japan). Before examination, samples were polished by sandpapers with grids from 180 to 1200 (Buehler Ltd, USA). Totally, 15 different measurements were performed from three separate surface of each sample with a diamond indenter which was applied a load of 19.61 N for 15 seconds. The Vickers Micro-hardness values of the samples were measured from X-marked indent shape which occurred after

indentation. The microhardness calculations of the specimens were obtained by applying the HV values obtained as a result of the tests to the formula given below. Furthermore, measurement device and diagonal indent shape observed from PLA compression sample during experiments are given in Figure 21.

$$HV = 0.001854 \frac{P}{d^2} \tag{8}$$

Where;

HV: Vickers hardness (GPA); P: Applied Force (N); d: Average length of diagonal indent
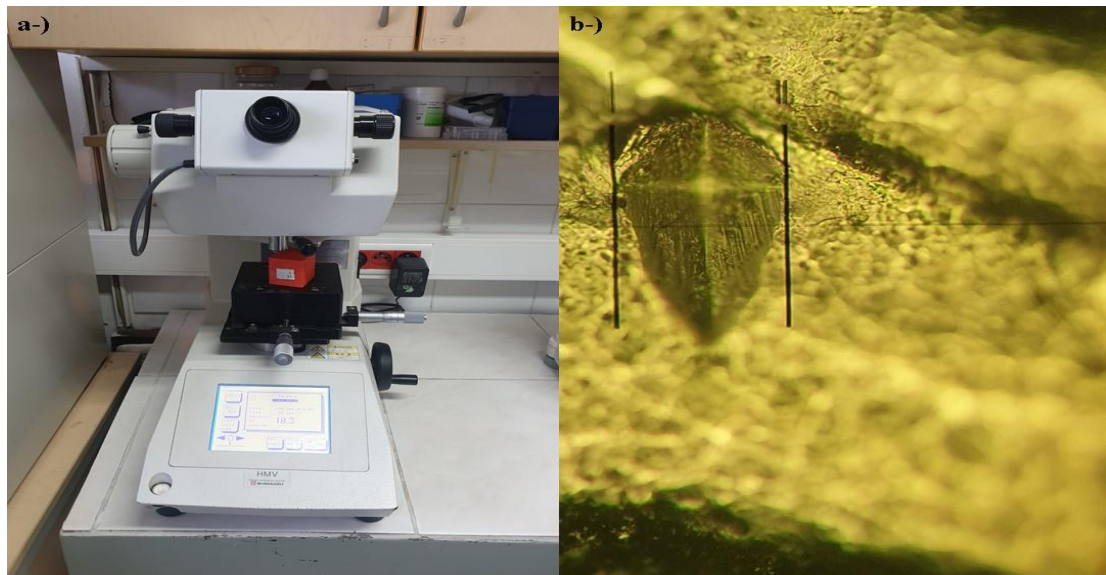
Figure 21. (a) HMV-2, Shimadzu Vickers Microhardness measurement device; (b) Diagonal indent shape observed from PLA compression sample.

3.3.2.1.2 FTIR Analysis

FTIR analyses were used to characterize the bond structure of the PLA polymer and Ti6Al4V alloy. Infrared rays between the wave number of 4000-400 cm^{-1} in the FTIR spectrum were sent into the samples and spectra were recorded using a Perkin Elmer 400, Norwalk, CT, USA.

3.3.2.1.3 XRD Analysis

Within the scope of this study, X-ray diffraction analysis was carried out to investigate the phase analysis of the PLA polymer. XRD analysis was performed by a Rigaku Ultima-IV X-Ray diffraction analysis device. Results were used to determine the phases contained in the samples and the lattice parameters. The samples were scanned in the scanning range of 5° - 75° , with a scanning speed of 0.1°/min.

3.3.2.2 Mechanical & Thermal Properties

3.3.2.2.1 TGA & DSC Analysis

TGA analyzes were carried out in a nitrogen environment, at a heating rate of 10 °C/min in the temperature range of 25-600 °C (Discovery SDT650, TA Instruments). This analysis determined the mass loss of PLA according to the temperature increase. DSC analysis was also performed similarly to TGA analysis. By subjecting the PLA specimen to DSC analysis, the determination of the glass transition temperature of PLA was provided, at a heating rate of 10 °C/min in the nitrogen environment, in the temperature range of 25-600 °C (Discovery SDT650, TA Instruments).

3.3.2.2.2 SEM Analysis

The surface morphology of the additively manufactured samples was observed with a scanning electron microscope at a voltage of 15 kV (Philips FEI Model: Quanta 400F). The specimen was displayed with 1000X, 2000X, 5000X, 10000X, 50000X and 100000X magnification values separately.

3.3.2.3   Numerical Analysis

3.3.2.3.1   Finite Element Analysis

In this thesis, a numerical approach was conducted besides the experimental approach to compare between the experimental and numerical results. In this context, tensile and compression test simulations were constituted via the ANSYS Workbench 2022 R1 platform for the samples designed through SolidWorks. The explicit analysis tool of the program was used for the simulations. The PLA and Ti6Al4V materials were specified for each sample from the program's library before simulations, and boundary conditions for the samples were created. Then, in various meshing trials for the samples, the optimal mesh convergence was seen when the element size was 0.5 mm, and the meshing was performed at this size for all samples.

3.3.2.4   Statistical Analysis

Experiment results were analyzed via the IBM SPSS statistic program and the parameter with the highest effect on the results was determined. In this context, the effect factor values of the unit cell parameters on the mechanical properties of the tensile and compression samples were investigated.

CHAPTER 4

4. RESULTS AND DISCUSSION

4.1 Mechanical Tests

4.1.1 Tension & Compression Tests of PLA-based Specimens

The tensile strength values of the PLA-based tension specimens with two different unit cells manufactured within the scope of this thesis are shown in Table 19. All of the samples in Table 19 were compared with the tensile strength value of a 100% filled specimen. Experimental results from three trials of each sample are averaged and given with the standard deviation values. The results show that the sample with the code T-P-R-L40T05θ68 has the lowest tensile strength. When the tensile strength value of the T-P-R-L30T05θ68, which has the same ligament thickness and angle as the T-P-R-L40T05θ68 coded sample, is examined, it is seen that strength value of the T-P-R-L30T05θ68 are two times higher than T-P-R-L40T05θ68. At this point, it can be concluded that the increase in the side length value of the cross-section in which the unit cell is located causes a decrease in the tensile strength values of the sample. However, when the mechanical properties of other samples with the same ligament thickness and angle values were compared, it can be seen that this observation cannot be true always, on the contrary, the increase in the lateral length values of the cross-section can enhance the mechanical properties of the sample.

On the other hand, it is seen that the sample with the second-lowest tensile strength value is the T-P-R-L35T05θ61. Herein, when the T-P-R-L35T05θ75 coded sample, which has the same cross-section side length and ligament thickness as the aforementioned sample, is examined, it is observed that there is almost a three-time difference in tensile strength. At this point, it has been observed that the increase in the ligament angle value may cause an increase in the tensile strength values. When the mechanical properties of the samples produced from two different unit cells using different parameters are compared,

it is seen that the second unit cell provides higher tensile strength and elastic modulus values at smaller ligament thickness and angle values compared to the first unit cell. On the contrary, the samples designed using second unit cell, exhibit lower tensile strength values at greater ligament thickness and angle values compared to the specimens designed within the first unit cell. Furthermore, experimental results of PLA-based tension samples are given in between Figure 22 and Figure 25.

Table 19. Tensile strength values of PLA-based specimens

Mechanical Properties of Unit Cell within Re-entrant Structure		Mechanical properties of Unit Cell within Re-entrant, Star and Octagonal Structure	
Specimens	**Tensile Strength (MPa)**	**Specimens**	**Tensile Strength (MPa)**
T-P-R-Raw Sample	43.09	T-P-RSO-Raw Sample	42.46
T-P-R-L35T05θ61	2.35 ± 0.68	T-P-RSO-L35T05θ61	3.96 ± 0.36
T-P-R-L35T05θ75	6.89 ± 0.77	T-P-RSO-L35T05θ75	6.96 ± 0.26
T-P-R-L35T15θ61	19.66 ± 0.51	T-P-RSO-L35T15θ61	13.51 ± 1.30
T-P-R-L35T15θ75	12.04 ± 0.53	T-P-RSO-L35T15θ75	6.91 ± 0.44
T-P-R-L30T05θ68	5.61 ± 0.60	T-P-RSO-L30T05θ68	4.28 ± 0.53
T-P-R-L40T05θ68	2.73 ± 0.97	T-P-RSO-L40T05θ68	4.63 ± 0.35
T-P-R-L30T15θ68	15.61 ± 1.84	T-P-RSO-L30T15θ68	10.64 ± 0.80
T-P-R-L40T15θ68	9.99 ± 0.69	T-P-RSO-L40T15θ68	10.27 ± 0.38
T-P-R-L30T10θ61	11.96 ± 1.94	T-P-RSO-L30T10θ61	9.63 ± 0.62
T-P-R-L40T10θ61	4.97 ± 0.44	T-P-RSO-L40T10θ61	7.55 ± 0.57
T-P-R-L30T10θ75	7.15 ± 1.79	T-P-RSO-L30T10θ75	5.52 ± 0.37
T-P-R-L40T10θ75	6.56 ± 0.22	T-P-RSO-L40T10θ75	6.99 ± 0.36
T-P-R-L35T10θ68	14.48 ± 0.78	T-P-RSO-L35T10θ68	4.95 ± 1.03
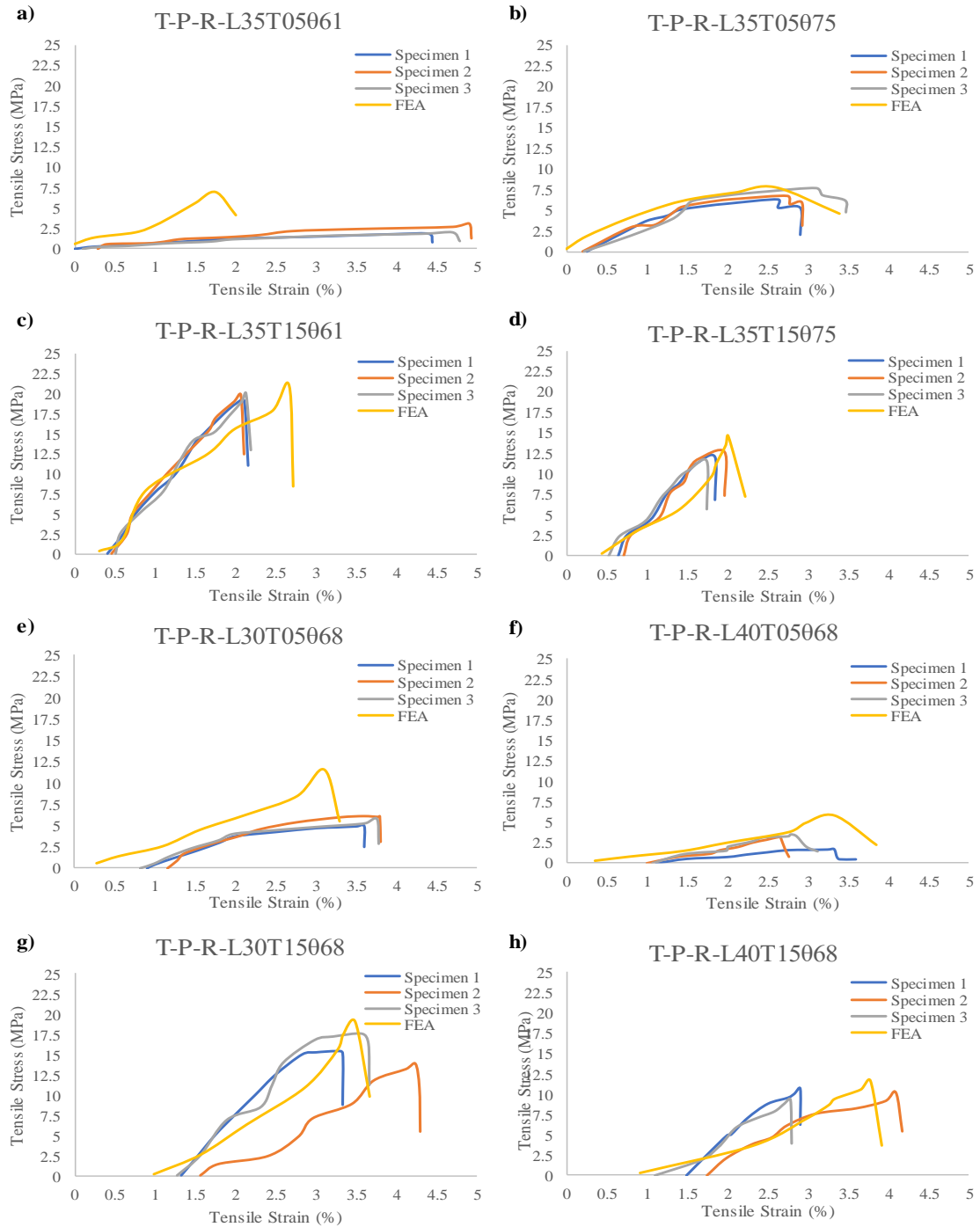
Figure 22. Experimental results of PLA based tension specimens; (a) T-P-R-L35T05θ61, (b) T-P-R-L35T05θ75, (c) T-P-R-L35T15θ61, (d) T-P-R-L35T15θ75, (e) T-P-R-L30T05θ68, (f) T-P-R-L40T05θ68, (g) T-P-R-L30T15θ68, (h) T-P-R-L40T15θ68
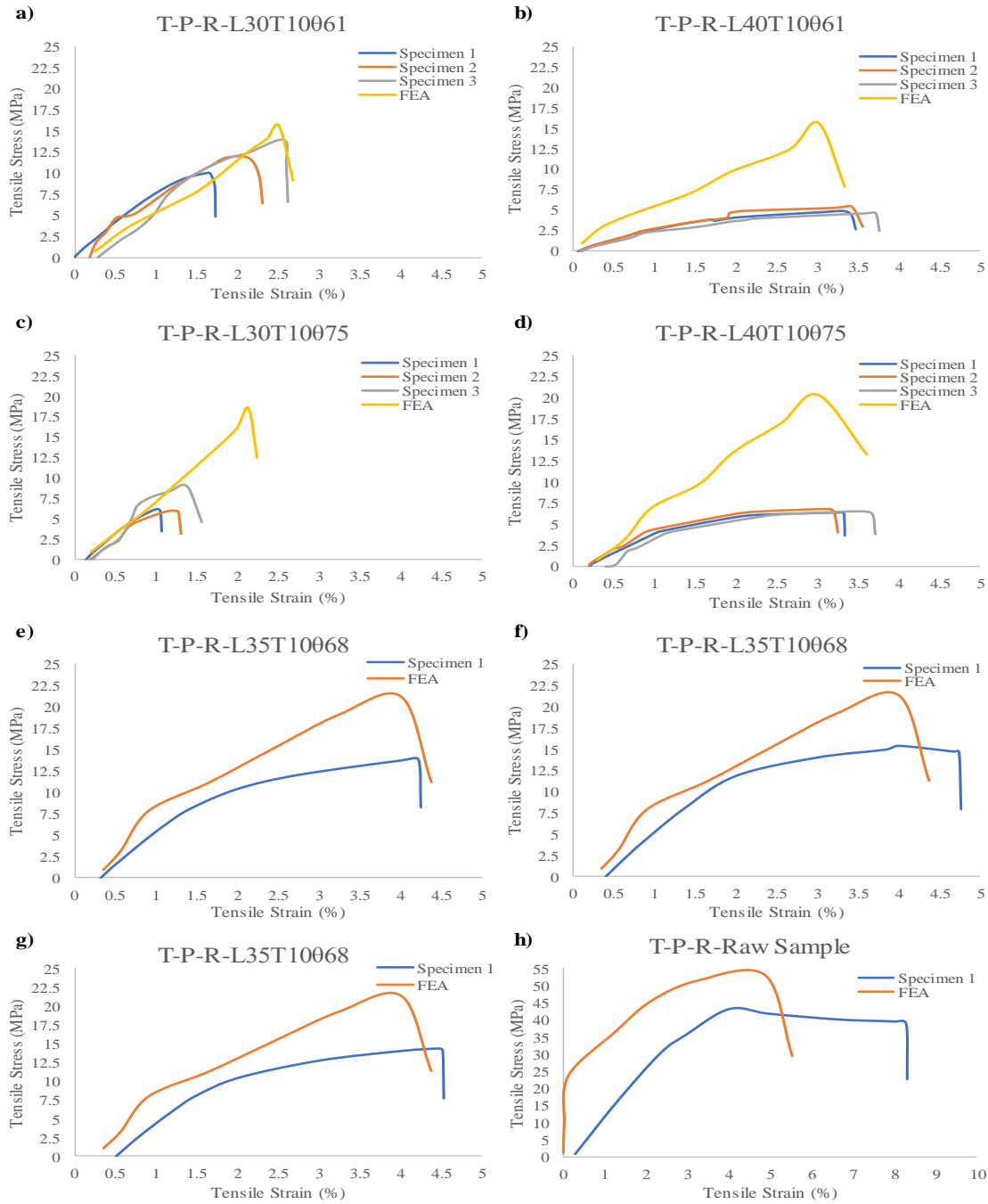
Figure 23. Experimental results of PLA based tension specimens; (a) T-P-R-L30T10θ61, (b) T-P-R-L40T10θ61, (c) T-P-R-L30T10θ75, (d) T-P-R-L40T10θ75, (e) T-P-R-L35T10θ68, (f) T-P-R-L35T10θ68, (g) T-P-R-L35T10θ68, (h) T-P-R-Raw Sample
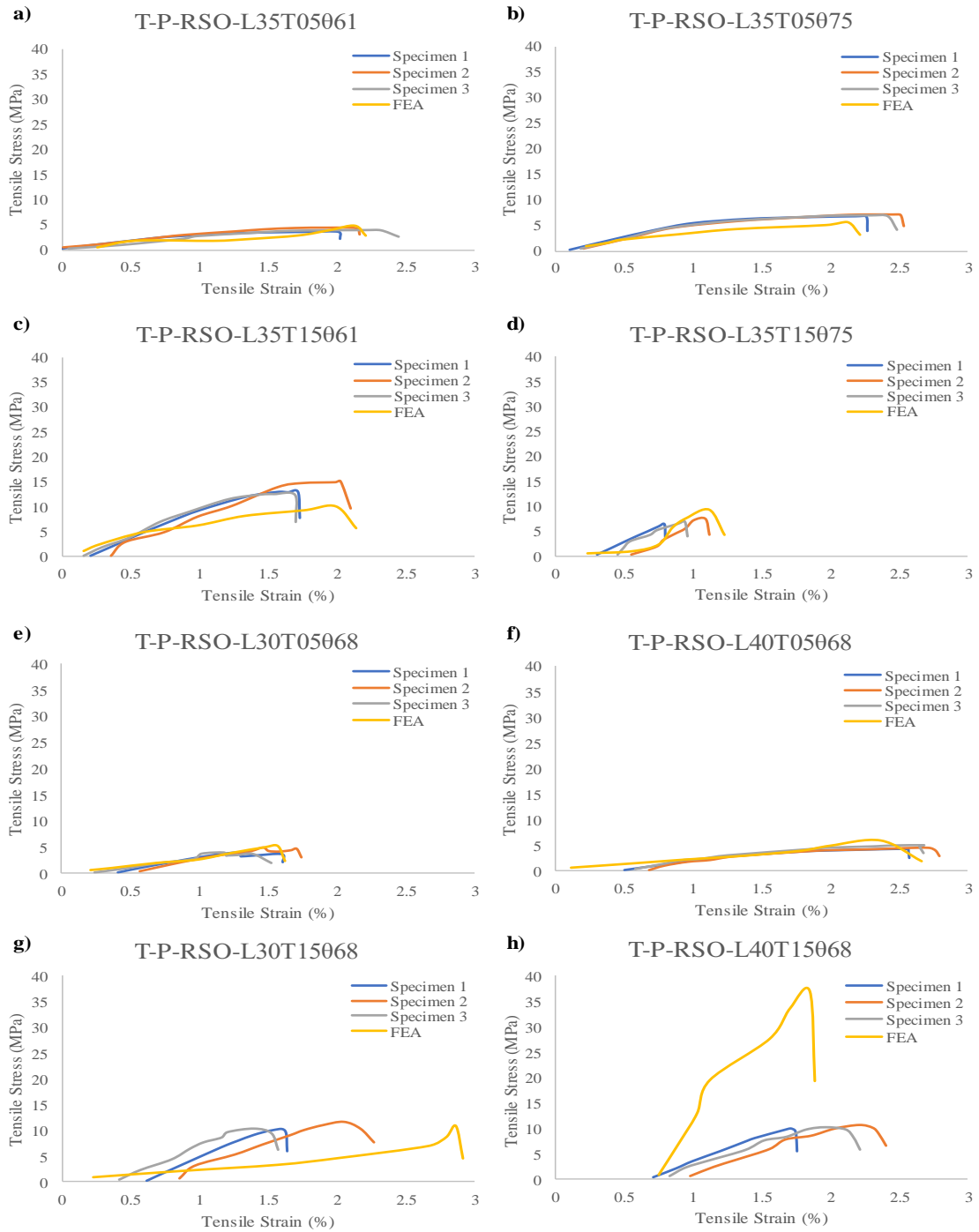
Figure 24. Experimental results of PLA based tension specimens; (a) T-P-RSO-L35T05θ61, (b) T-P-RSO-L35T05θ75, (c) T-P-RSO-L35T15θ61, (d) T-P-RSO-L35T15θ75, (e) T-P-RSO-L30T05θ68, (f) T-P-RSO-L40T05θ68, (g) T-P-RSO-L30T15θ68, (h) T-P-RSO-L40T15θ68
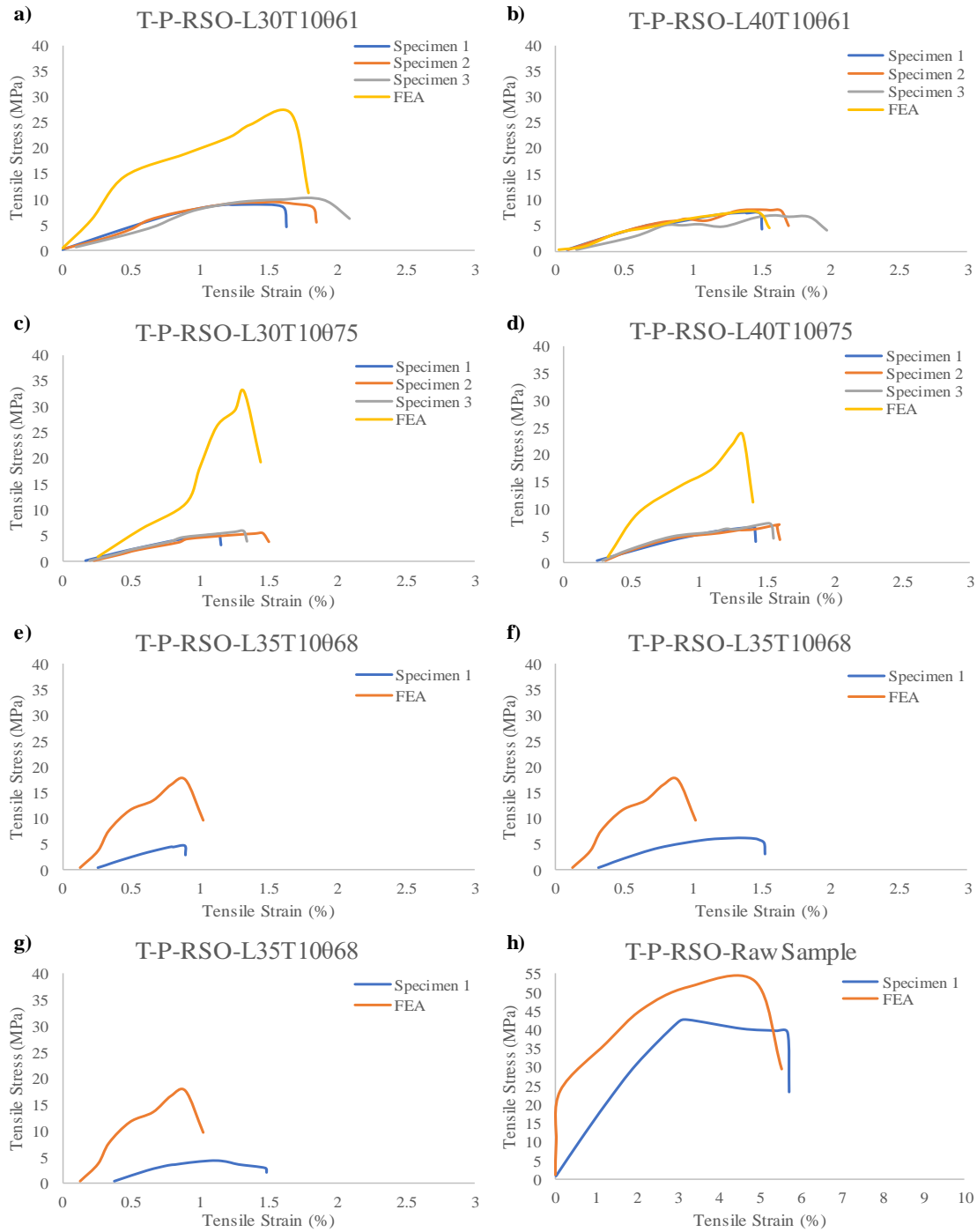
Figure 25. Experimental results of PLA based tension specimens; (a) T-P-RSO-L30T10θ61, (b) T-P-RSO-L40T10θ61, (c) T-P-RSO-L30T10θ75, (d) T-P-RSO-L40T10θ75, (e) T-P-RSO-L35T10θ68, (f) T-P-RSO-L35T10θ68, (g) T-P-RSO-L35T10θ68, (h) T-P-RSO-Raw Sample

74

Additionally, when the tensile strength of the T-P-R-L35T15θ61 coded sample is compared with the 100% filled PLA sample, it is seen that the tensile strength value is 56% lower. The reason for this might be the technical limitations caused by the calibration and sensitivity of the 3d printer used during production and the small cross-sectional areas caused by the lattice geometry cavities in the specimen. Furthermore, the compressive strength and elastic modulus values of the PLA-based compression specimens with two different unit cells are given in Table 20.

Table 20. Compressive strength values of PLA-based specimens

Mechanical Properties of Unit Cell within Re-entrant Structure		Mechanical properties of Unit Cell within Re-entrant, Star and Octagonal Structure	
Specimens	**Compressive Strength (MPa)**	**Specimens**	**Compressive Strength (MPa)**
C-P-R-Raw Sample	2190.38	C-P-RSO-Raw Sample	2008.35
C-P-R-L35T05θ61	542.94 ± 26.79	C-P-RSO-L35T05θ61	365.70 ± 43.99
C-P-R-L35T05θ75	367.71 ± 40.30	C-P-RSO-L35T05θ75	277.86 ± 16.22
C-P-R-L35T15θ61	1201.53 ± 171.52	C-P-RSO-L35T15θ61	1021.2 ± 121.64
C-P-R-L35T15θ75	768.88 ± 57.47	C-P-RSO-L35T15θ75	762.90 ± 69.54
C-P-R-L30T05θ68	354.53 ± 49.57	C-P-RSO-L30T05θ68	405.61 ± 36.97
C-P-R-L40T05θ68	241.06 ± 64.46	C-P-RSO-L40T05θ68	395.20 ± 36.02
C-P-R-L30T15θ68	192.18 ± 8.40	C-P-RSO-L30T15θ68	1309.08 ± 95.52
C-P-R-L40T15θ68	399.87 ± 40.89	C-P-RSO-L40T15θ68	665.28 ± 66.71
C-P-R-L30T10θ61	644.69 ± 131.39	C-P-RSO-L30T10θ61	1148.3 ± 104.67
C-P-R-L40T10θ61	216.13 ± 25.09	C-P-RSO-L40T10θ61	1141.87 ± 99.08
C-P-R-L30T10θ75	643.92 ± 95.24	C-P-RSO-L30T10θ75	736.18 ± 67.11
C-P-R-L40T10θ75	318.18 ± 25.56	C-P-RSO-L40T10θ75	228.35 ± 15.91
C-P-R-L35T10θ68	1553.36 ± 153.34	C-P-RSO-L35T10θ68	654.69 ± 45.62

The compressive strength values of the PLA-based specimens with two different unit cells manufactured within the scope of this thesis are shown in Table 20. Experimental results from three trials of each sample are averaged and given with the standard deviation values. The results show that the sample with the parameters 30 mm cross section length, 1.5 mm ligament thickness and 68 degrees ligament angle, has lowest compressive strength value among the unit cells formed by Re-entrant structure. On the other hand, the sample with the parameters 40 mm cross section length, 1 mm ligament thickness and 75 degrees ligament angle, has lowest compressive strength value among the unit cells formed by Re-entrant , Star and Octagonal structures.

The results show that the sample with the code C-P-R-L40T05θ68 has the lowest compressive strength. When the compressive strength and elastic modulus values of the C-P-R-L30T05θ68, which has the same ligament thickness and angle as the C-P-R-L40T05θ68 coded sample, are examined, it is seen that strength & modulus values of the C-P-R-L30T05θ68 are two times higher than C-P-R-L40T05θ68. At this point, it can be concluded that the increase in the side length value of the cross-section in which the unit cell is located causes a decrease in the tensile strength values of the sample. However, when the mechanical properties of other samples with the same ligament thickness and angle values were compared, it can be seen that this observation cannot be true, on the contrary, the increase in the lateral length values of the cross-section will increase the mechanical properties of the sample. Moreover, experimental results of PLA-based compression samples are given in between Figure 26 and Figure 29.

Among the studies the minimum sample height was stated as 19 mm in the study by Damanpack et al., [72]. They formed the specimens with PLA using honeycomb lattice structure appropriate with the ASTM D638 standard and they determined the elastic modulus of the specimens. Furthermore, they obtained maximum tensile strength value as a 0.48 MPa. Additionally, in a study by Ravari et al., the samples are constituted in accordance with the ASTM-D638 standard and formed by the triangular lattice structure

[73]. PLA is used as a production material of samples. Samples were subjected to tensile tests and the tensile strength value of the sample with the highest strength was found to be 49.07 MPa [73].

Furthermore, in another study that is laid out by Quan et al., PLA is used as production material and samples were constituted by using re-entrant lattice structure [36]. In addition, maximum tensile strength value is obtained as 31.95 MPa in this study. Based on their results, it is seen that when PLA transforms into a lattice shape, it's modulus of elasticity extremely decreases. This circumstance indicates that lattice geometry structures have low rigidity, high strain percentage value for PLA material. These results also show that lattice geometry structures that are produced with PLA have low compressive strength and show brittle property. Hence, it can be seen that they have maximum deformation under minimum compression load [36].

As a result of experimental tests, parameters for the simulations are attained, modified, and imported into FEM codes to represent the behavior of the material. The FEM study employed isotropic elasticity and plasticity to evaluate the deformation threshold of the tension and compression specimens without causing failures, irreversible deformations, or deterioration. As seen in between Figure 22 and Figure 37, results showed that how the flexural test and the findings of the quantitative analysis have strong relationships.
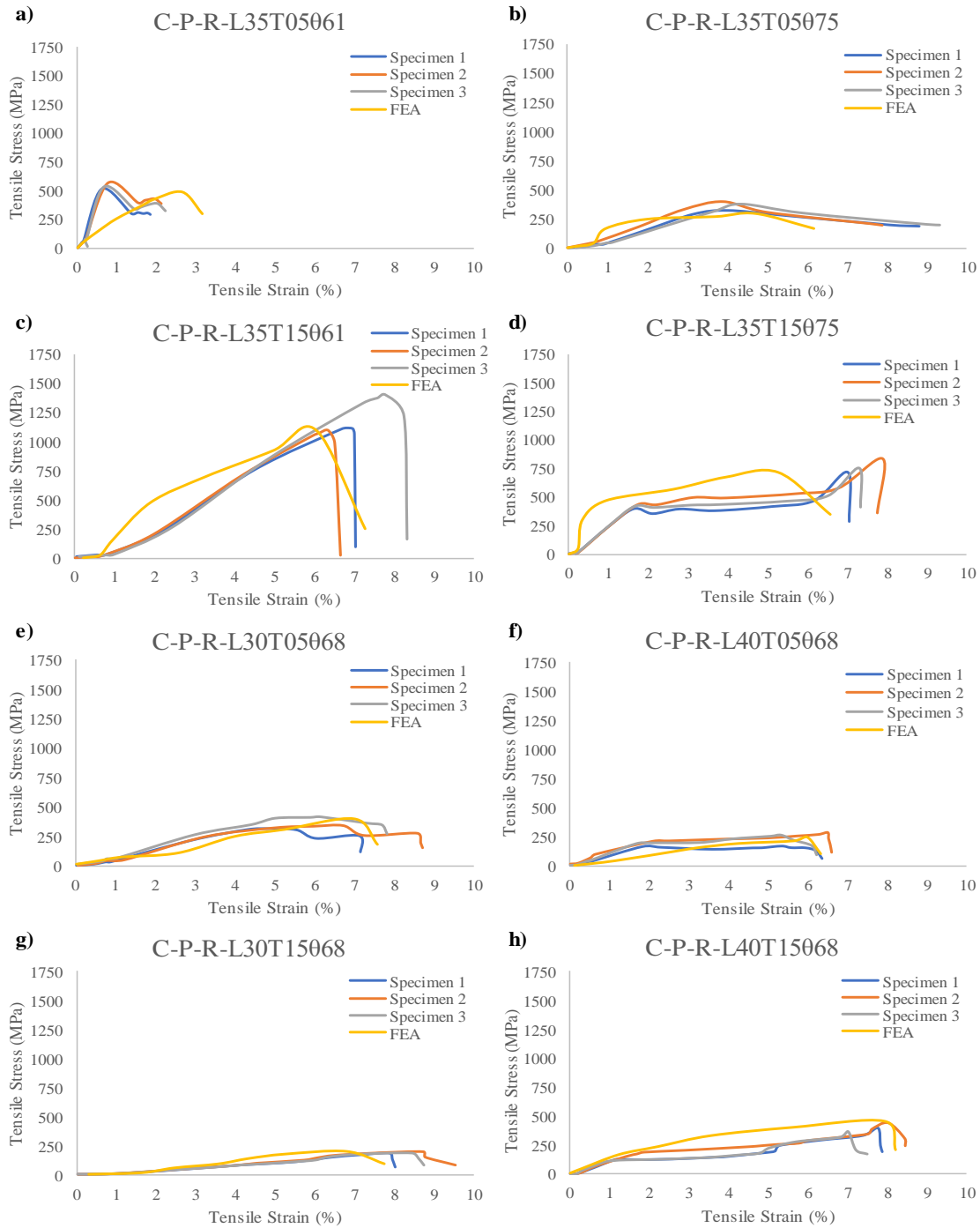
Figure 26. Experimental results of PLA based compression specimens; (a) C-P-R-L35T05θ61, (b) C-P-R-L35T05θ75, (c) C-P-R-L35T15θ61, (d) C-P-R-L35T15θ75, (e) C-P-R-L30T05θ68, (f) C-P-R-L40T05θ68, (g) C-P-R-L30T15θ68, (h) C-P-R-L40T15θ68
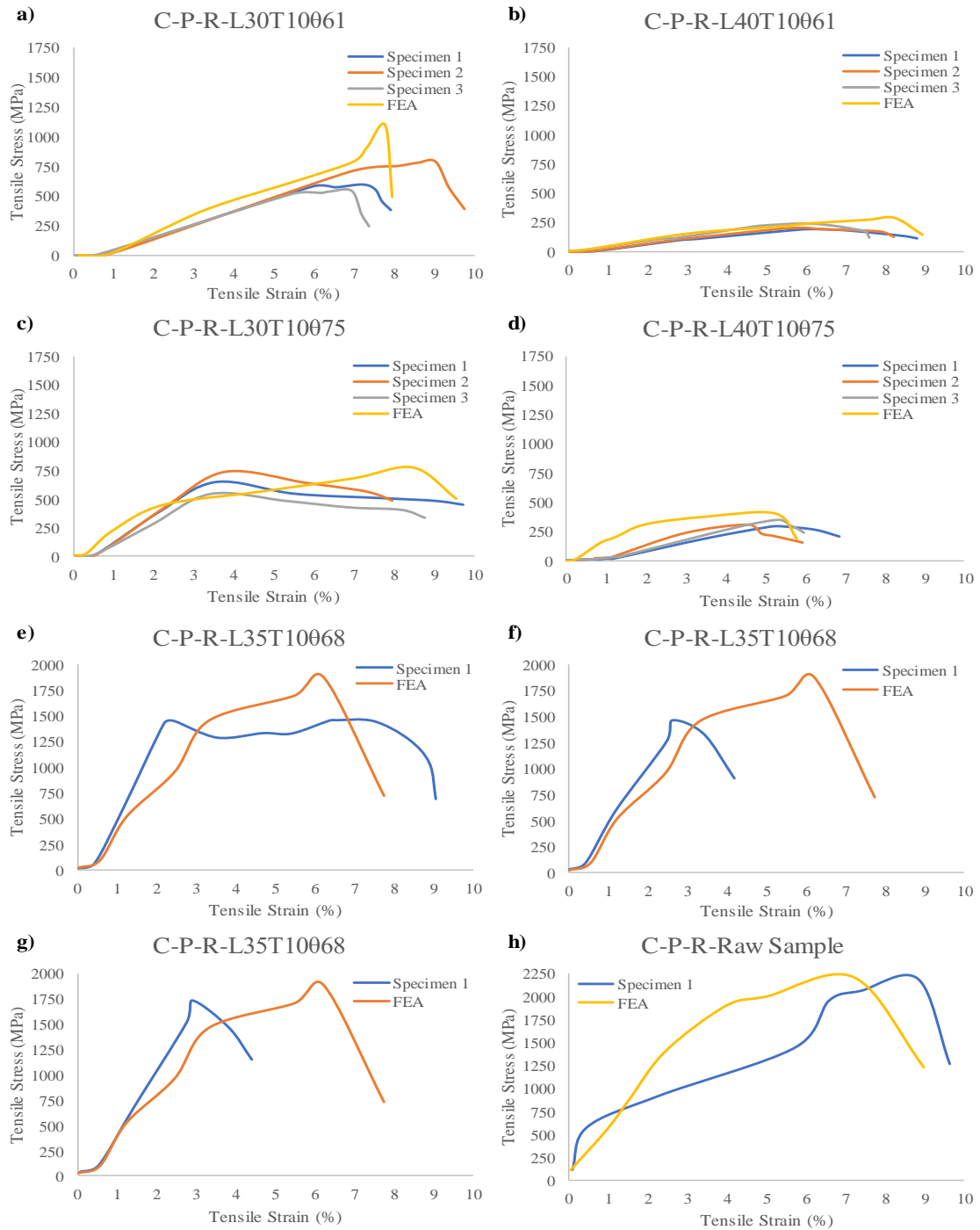
Figure 27. Experimental results of PLA based compression specimens; (a) C-P-R-L30T10θ61, (b) C-P-R-L40T10θ61, (c) C-P-R-L30T10θ75, (d) C-P-R-L40T10θ75, (e) C-P-R-L35T10θ68, (f) C-P-R-L35T10θ68, (g) C-P-R-L35T10θ68, (h) C-P-R-Raw Sample
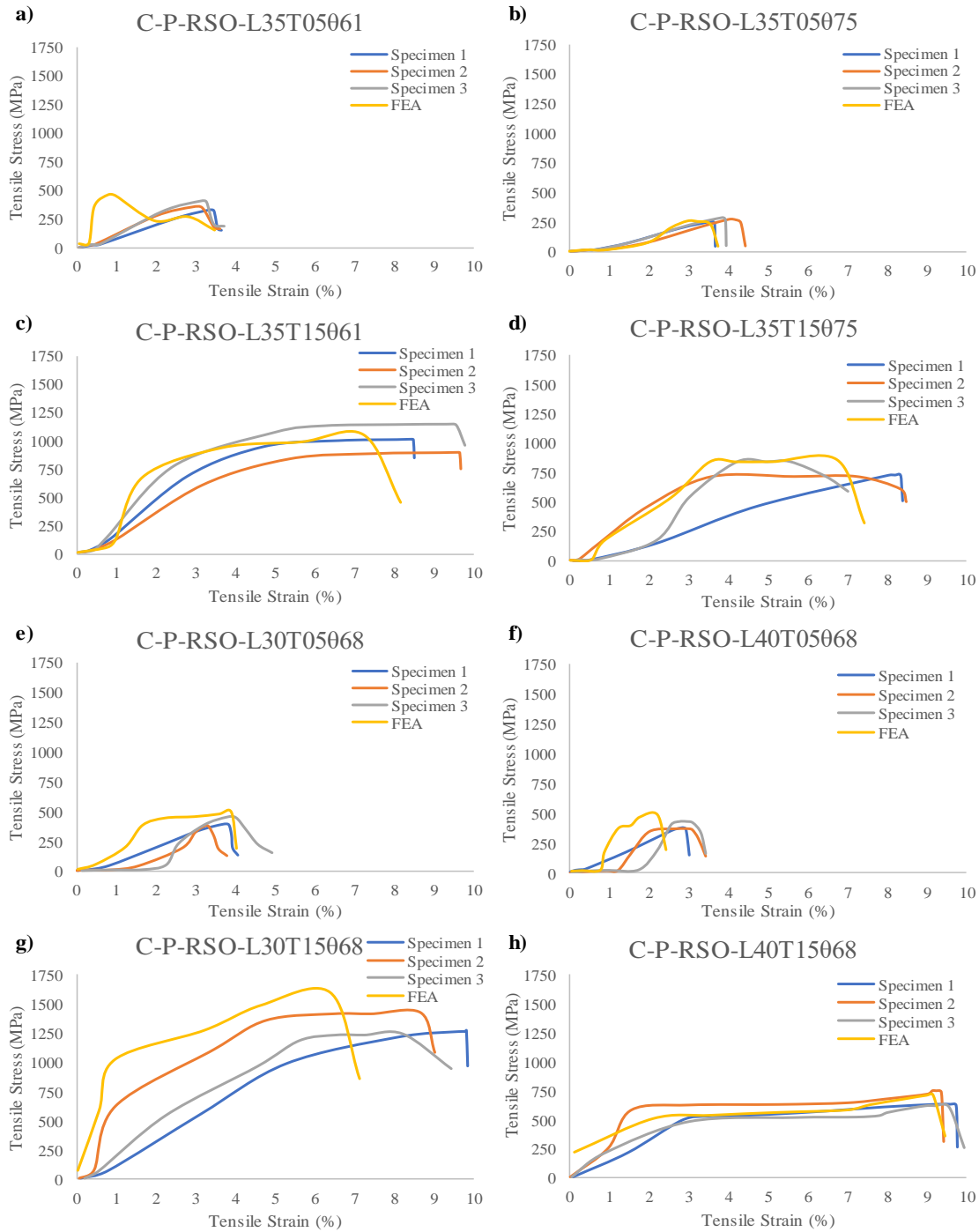
Figure 28. Experimental results of PLA based compression specimens; (a) C-P-RSO-L35T05θ61, (b) C-P-RSO-L35T05θ75, (c) C-P-RSO-L35T15θ61, (d) C-P-RSO-L35T15θ75, (e) C-P-RSO-L30T05θ68, (f) C-P-RSO-L40T05θ68, (g) C-P-RSO-L30T15θ68, (h) C-P-RSO-L40T15θ68
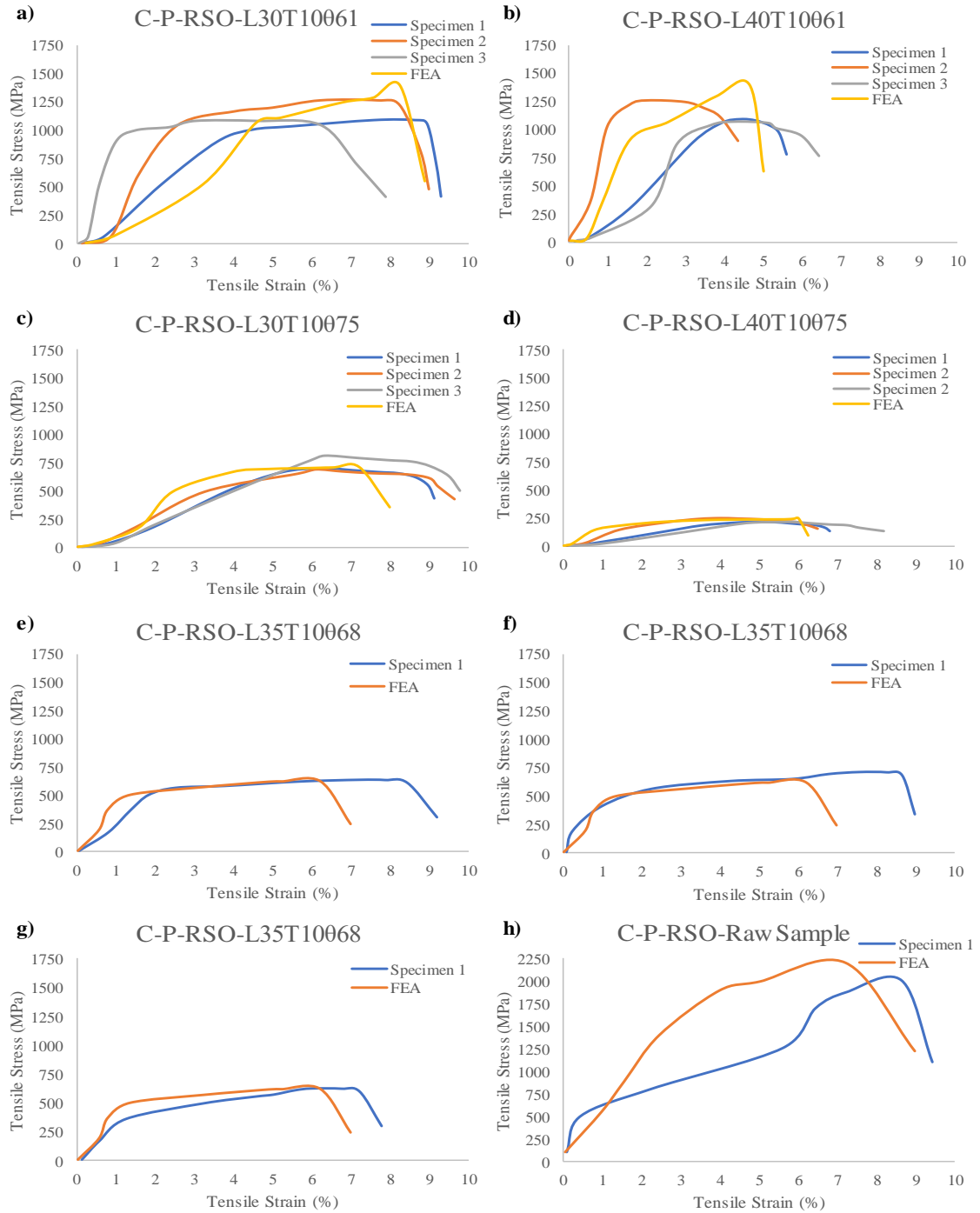
Figure 29. Experimental results of PLA based compression specimens; (a) C-P-RSO-L30T10θ61, (b) C-P-RSO-L40T10θ61, (c) C-P-RSO-L30T10θ75, (d) C-P-RSO-L40T10θ75, (e) C-P-RSO-L35T10θ68, (f) C-P-RSO-L35T10θ68, (g) C-P-RSO-L35T10θ68, (h) C-P-RSO-Raw Sample

4.1.2 Tension & Compression Tests of Ti6Al4V-based Specimens

The tensile strength and elastic modulus of the Ti6Al4V-based tension specimens with two different unit cells manufactured within the scope of this thesis are shown in Table 21. All of the samples in Table 21 were compared with the tensile strength and elastic modulus value of a 100% filled specimen.

Table 21. Tensile strength values of Ti6Al4V-based specimens

Mechanical Properties of Unit Cell within Re-entrant Structure		Mechanical properties of Unit Cell within Re-entrant, Star and Octagonal Structure	
Specimens	Tensile Strength (MPa)	Specimens	Tensile Strength (MPa)
T-Ti-R-Raw Sample	198.56	T-Ti-RSO-Raw Sample	204.86
T-Ti-R-L35T05θ61	39.90	T-Ti-RSO-L35T05θ61	20.08
T-Ti-R-L35T05θ75	43.86	T-Ti-RSO-L35T05θ75	41.20
T-Ti-R-L35T15θ61	32.06	T-Ti-RSO-L35T15θ61	40.82
T-Ti-R-L35T15θ75	46.88	T-Ti-RSO-L35T15θ75	58.14
T-Ti-R-L30T05θ68	45.61	T-Ti-RSO-L30T05θ68	30.53
T-Ti-R-L40T05θ68	24.39	T-Ti-RSO-L40T05θ68	14.87
T-Ti-R-L30T15θ68	157.39	T-Ti-RSO-L30T15θ68	164.60
T-Ti-R-L40T15θ68	113.30	T-Ti-RSO-L40T15θ68	80.77
T-Ti-R-L30T10θ61	61.48	T-Ti-RSO-L30T10θ61	81.65
T-Ti-R-L40T10θ61	70.45	T-Ti-RSO-L40T10θ61	32.64
T-Ti-R-L30T10θ75	49.18	T-Ti-RSO-L30T10θ75	76.45
T-Ti-R-L40T10θ75	56.51	T-Ti-RSO-L40T10θ75	40.35
T-Ti-R-L35T10θ68	86.19	T-Ti-RSO-L35T10θ68	67.04

Ti6Al4V tensile test specimens were produced according to ASTM D638 in the horizontal direction. Tensile specimens were sandblasted before the tests in order to remove the surface roughness because EBM printed parts had a significant degree of surface roughness.

The results of the tensile tests performed on samples made of Ti6Al4V are shown in Figures 30 through 33. The results show that the length of the cross-sectional area and the angle of the ligaments were not dominant factors for Young's modulus, and yet higher ultimate tensile strength results are encountered in the 40 mm and 68-degree building orientations. Young's modulus was measured with no significant variation according to ligament thickness in a sample coded by T-Ti-R-L35T1575 and T-Ti-R-L30T0568. However, 35 mm and 61-degree structure orientations had relatively low strength values.

The strength value for 30 mm cross-section length specimen was more significant and better than that of the 40 mm cross-section length specimen with value of 164.6 MPa and 80.77 MPa for T-Ti-RSO-L30T15θ68 and T-Ti-RSO-L40T15θ68 build orientations, respectively.

It can be concluded that mechanical properties obtained from simulations are higher than those of the experimental test results. Due to the EBM manufacturing process and material inhomogeneity, this situation may be explained by the absence of fusion, oxidation, excessive surface roughness, leftover sections, and surface deformation resulting from the support separation process. The impact of local deformation brought on by excessive surface roughness may be used to explain why the strength values for 1 mm and 1.5 mm thicknesses differ. For specimens with a 1.5 mm thickness, which can withstand larger local deformations, the effective load-supporting area is bigger. Furthermore, superior mechanical performance in the 75-degree design orientation can be attributed to layers that are placed in the same direction.

Figure 30. Experimental results of Ti6Al4V based tension specimens; (a) T-Ti-R-L35T05θ61, (b) T-Ti-R-L35T05θ75, (c) T-Ti-R-L35T15θ61, (d) T-Ti-R-L35T15θ75, (e) T-Ti-R-L30T05θ68, (f) T-Ti-R-L40T05θ68, (g) T-Ti-R-L30T15θ68, (hT-Ti-R-L40T15θ68

Figure 31. Experimental results of Ti6Al4V based tension specimens; (a) T-Ti-R-L30T10θ61, (b) T-Ti-R-L40T10θ61, (c) T-Ti-R-L30T10θ75, (d) T-Ti-R-L40T10θ75, (e) T-Ti-R-L35T10θ68, (f) T-Ti-R-L35T10θ68, (g) T-Ti-R-L35T10θ68, (h) T-Ti-R-Raw Sample

Figure 32. Experimental results of Ti6Al4V based tension specimens; (a) T-Ti-RSO-L35T05θ61, (b) T-Ti-RSO-L35T05θ75, (c) T-Ti-RSO-L35T15θ61, (d) T-Ti-RSO-L35T15θ75, (e) T-Ti-RSO-L30T05θ68, (f) T-Ti-RSO-L40T05θ68, (g) T-Ti-RSO-L30T15θ68, (h) T-Ti-RSO-L40T15θ68
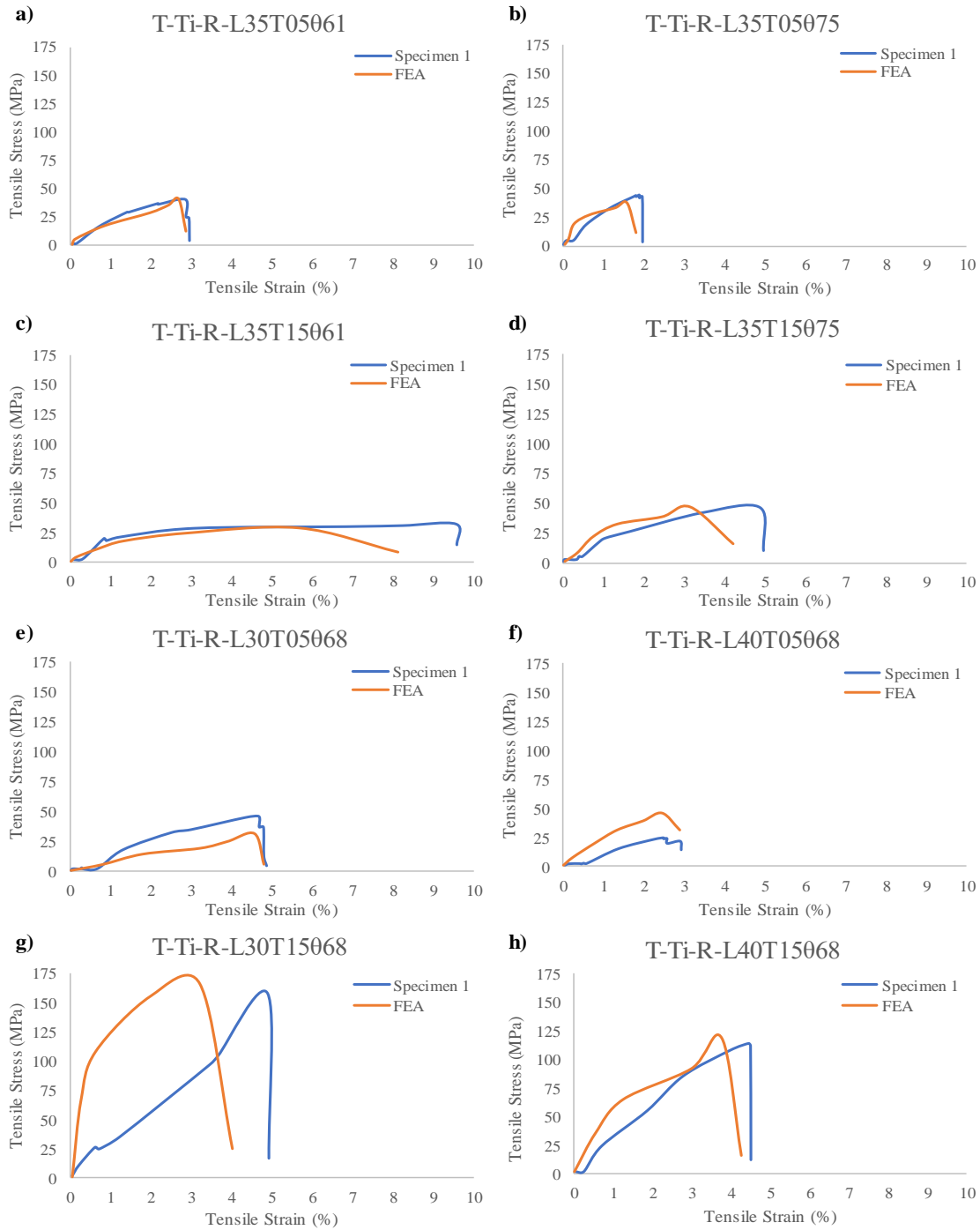
Figure 33. Experimental results of Ti6Al4V based tension specimens; (a) T-Ti-RSO-L30T10θ61, (b) T-Ti-RSO-L40T10θ61, (c) T-Ti-RSO-L30T10θ75, (d) T-Ti-RSO-L40T10θ75, (e) T-Ti-RSO-L35T10θ68, (f) T-Ti-RSO-L35T10θ68, (g) T-Ti-RSO-L35T10θ68, (h) T-Ti-RSO-Raw Sample

Furthermore, the tensile strength and elastic modulus values of the Ti6Al4V-based compression specimens with two different unit cells are given in Table 22. Moreover, experimental results of Ti6Al4V-based samples are given between Figure 30 and Figure 37.

Table 22. Compressive strength values of Ti6Al4V-based specimens

Mechanical Properties of Unit Cell within Re-entrant Structure		Mechanical properties of Unit Cell within Re-entrant, Star and Octagonal Structure	
Specimens	**Compressive Strength (MPa)**	**Specimens**	**Compressive Strength (MPa)**
C-Ti-R-Raw Sample	7999.26	C-Ti-RSO-Raw Sample	7206.54
C-Ti-R-L35T05θ61	2065.56	C-Ti-RSO-L35T05θ61	1452.78
C-Ti-R-L35T05θ75	2200.20	C-Ti-RSO-L35T05θ75	1251.23
C-Ti-R-L35T15θ61	4869.14	C-Ti-RSO-L35T15θ61	1258.53
C-Ti-R-L35T15θ75	3495.93	C-Ti-RSO-L35T15θ75	3021.59
C-Ti-R-L30T05θ68	2305.05	C-Ti-RSO-L30T05θ68	2204.30
C-Ti-R-L40T05θ68	2133.47	C-Ti-RSO-L40T05θ68	2390.70
C-Ti-R-L30T15θ68	2367.80	C-Ti-RSO-L30T15θ68	3121.08
C-Ti-R-L40T15θ68	3168.71	C-Ti-RSO-L40T15θ68	2753.46
C-Ti-R-L30T10θ61	4000.66	C-Ti-RSO-L30T10θ61	2774.83
C-Ti-R-L40T10θ61	1961.16	C-Ti-RSO-L40T10θ61	2687.63
C-Ti-R-L30T10θ75	2607.57	C-Ti-RSO-L30T10θ75	2137.33
C-Ti-R-L40T10θ75	2346.99	C-Ti-RSO-L40T10θ75	2605.72
C-Ti-R-L35T10θ68	2705.63	C-Ti-RSO-L35T10θ68	3014.52

It is discovered from the results of the compression experiment that certain EBM-printed Ti4Al6V components exhibit isotropic elastic and plastic anisotropic characteristics. The production of re-entrant and octagonal lattice structures, whose flat surfaces are parallel to the building plate surface, is also explained by the fact that 61-degree production exhibits consistent mechanical performance in comparison to the 75-degree production orientation due to the variations in strength.

The numerical models may be utilized to simulate the stress and compression scenario of re-entrant, star, and octagonal auxetic structures since the consistency between the numerical and experimental data is seen to be within an appropriate range. The results of FEM and experiments diverge in the plateau area, when rotation and movement of unit cells, plastic deformation, and fractures occurred in addition to elastic deformation. This is seen in the graphics, where the initial zone solely exhibits elastic deformation. Experimental data exhibit fluctuating behavior more frequently than FEM results in the plateau area. The excessive surface roughness and discontinuity on the surface of the unit cells, which led to choking and instant lateral displacement of the cells under compressional stresses but were not visible in the FEM analysis, may be attributed for this circumstance. It may be argued that comparable behavior can be caught in the approximation's points in relation to the investigation of the beginning of densification.

A change in ligament thickness can also affect the unit cell's auxetic properties and deformation pattern. The 1.5 mm thick re-entrant cell did not exhibit lateral distortion. Additionally, the beginning of the nonlinear deformation and the beginning of the maximum tensile strength were identified and confirmed by experimental findings. The unit cell with the 0.5 mm ligament thickness performs better in the tension test in terms of FEA values, whereas the 1.5 mm unit cell performs better in terms of experimental values.

Figure 34. Experimental results of Ti6Al4V based compression specimens; (a) C-Ti-R-L35T05θ61, (b) C-Ti-R-L35T05θ75, (c) C-Ti-R-L35T15θ61, (d) C-Ti-R-L35T15θ75, (e) C-Ti-R-L30T05θ68, (f) C-Ti-R-L40T05θ68, (g) C-Ti-R-L30T15θ68, (h) C-Ti-R-L40T15θ68
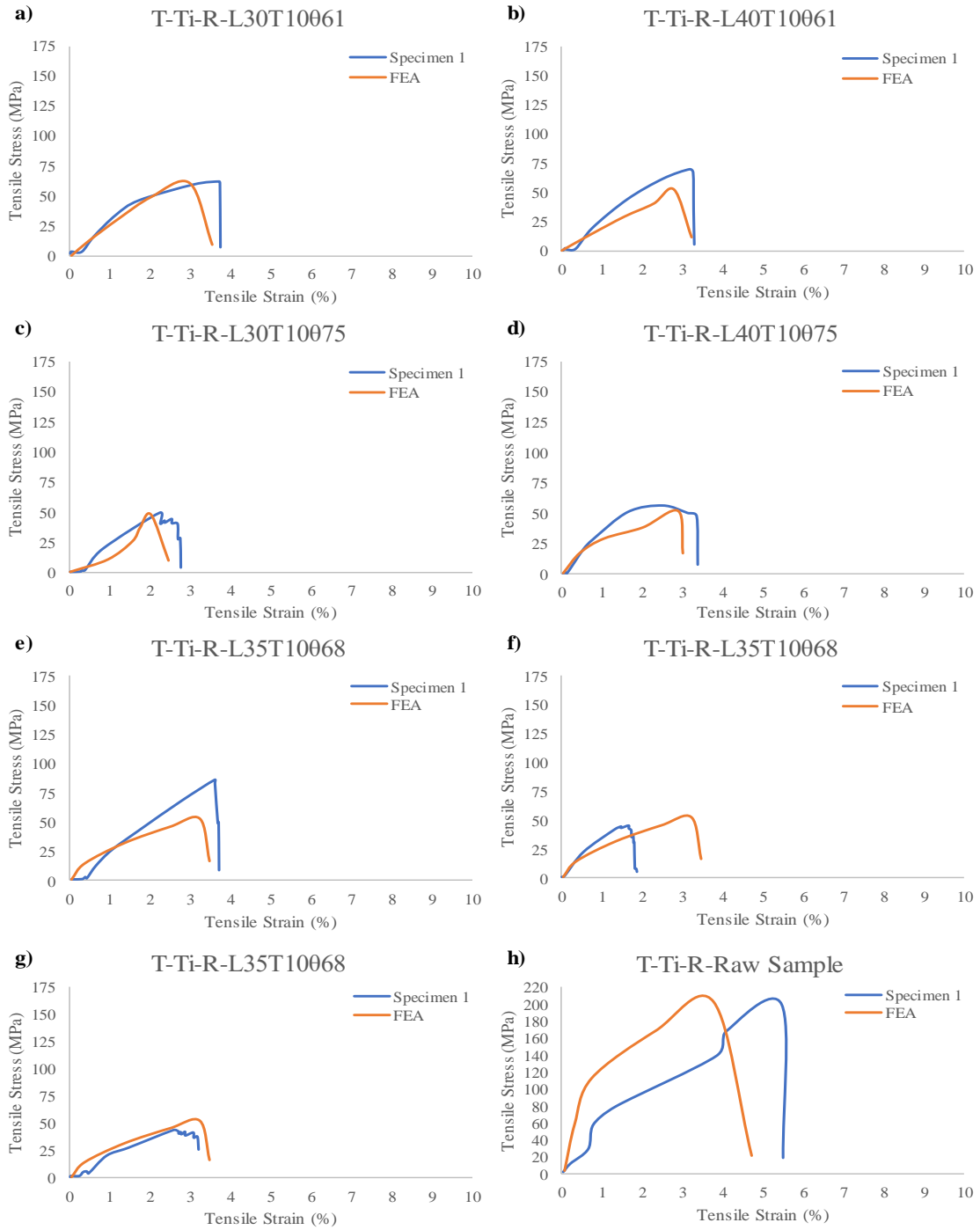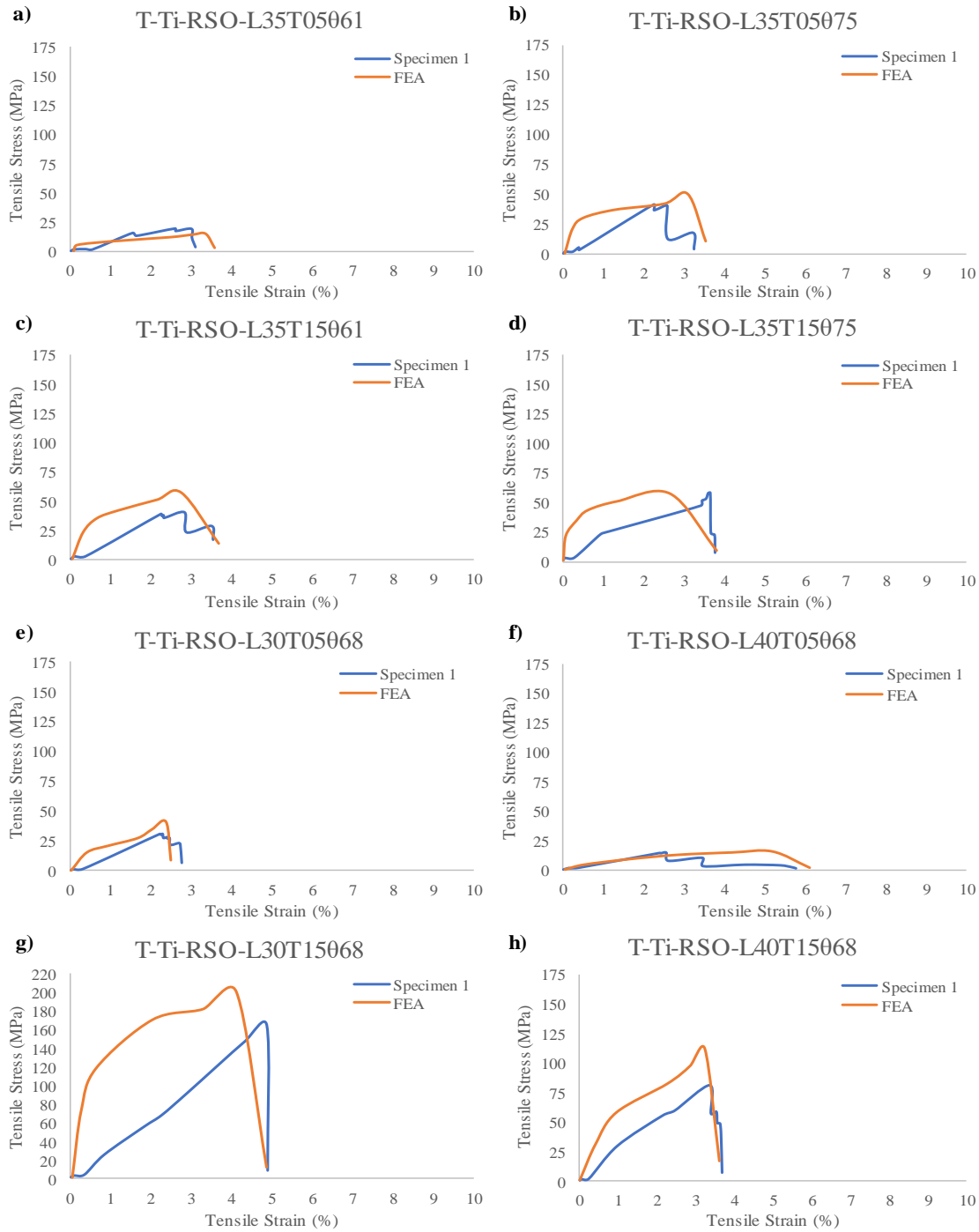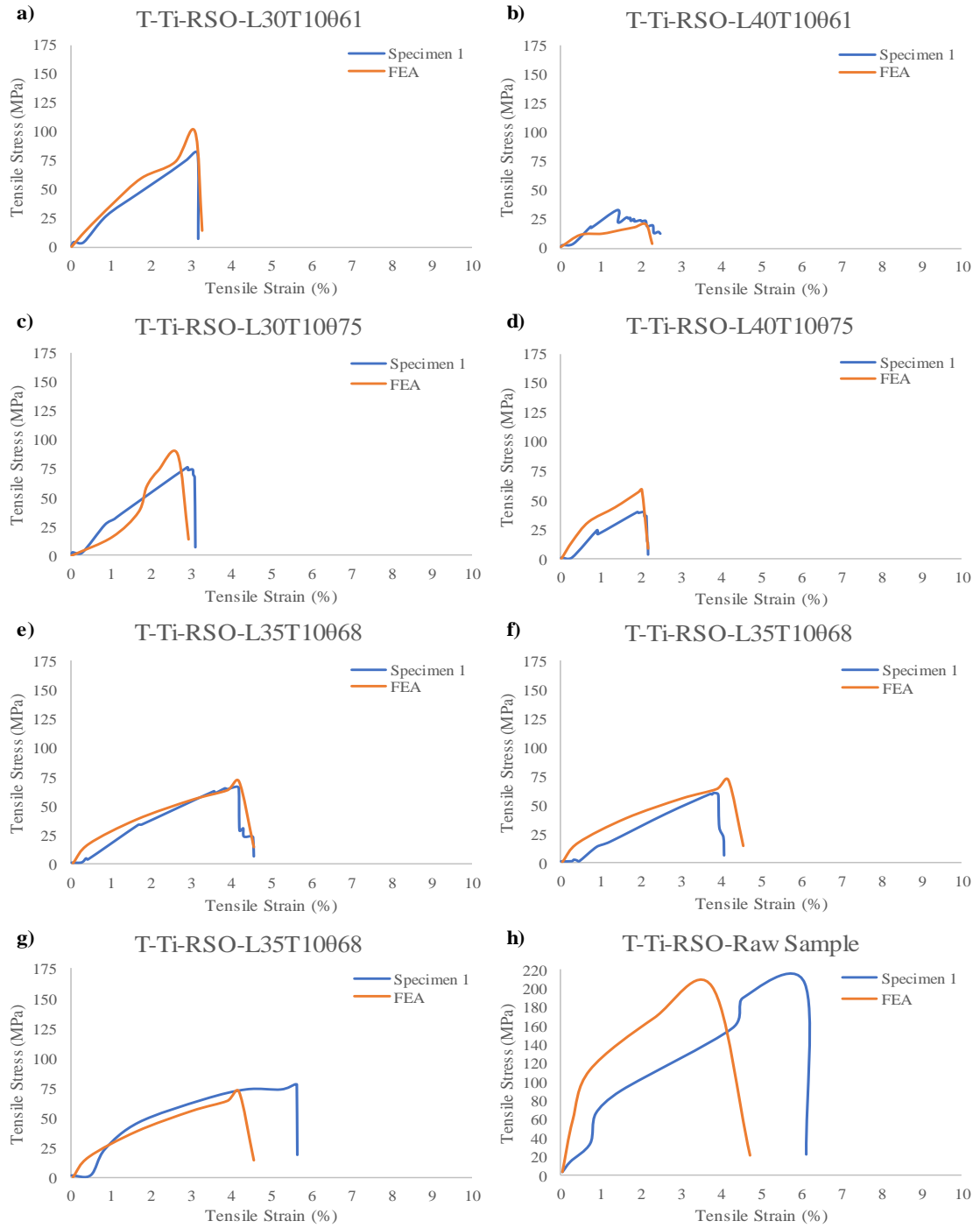
Figure 35. Experimental results of Ti6Al4V based compression specimens; (a) C-Ti-R-L30T10θ61, (b) C-Ti-R-L40T10θ61, (c) C-Ti-R-L30T10θ75, (d) C-Ti-R-L40T10θ75, (e) C-Ti-R-L35T10θ68, (f) C-Ti-R-L35T10θ68, (g) C-Ti-R-L35T10θ68, (h) C-Ti-R-Raw Sample
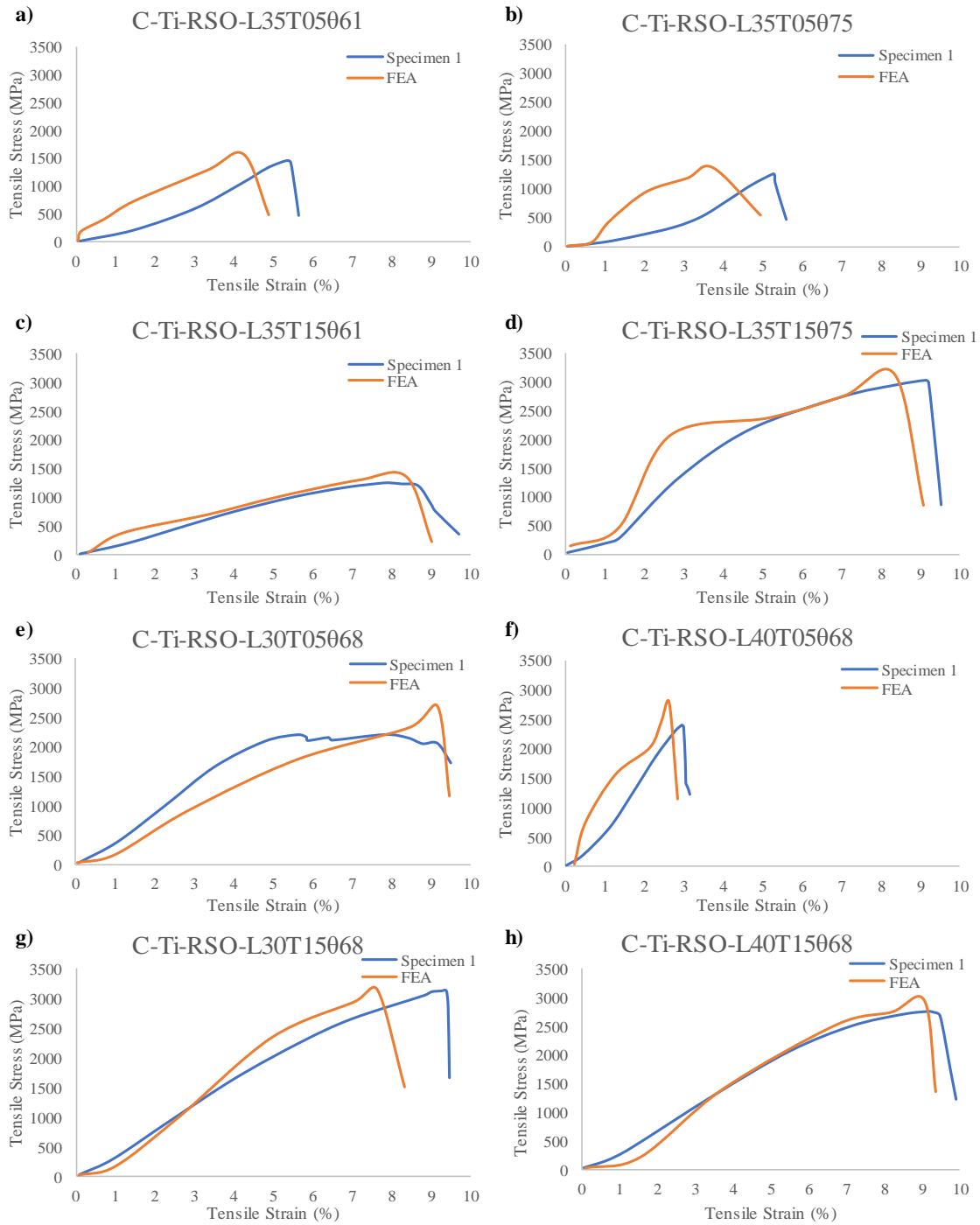
Figure 36. Experimental results of Ti6Al4V based compression specimens; (a) C-Ti-RSO-L35T05θ61, (b) C-Ti-RSO-L35T05θ75, (c) C-Ti-RSO-L35T15θ61, (dC-Ti-RSO-L35T15θ75, (e) C-Ti-RSO-L30T05θ68, (f) C-Ti-RSO-L40T05θ68, (g) C-Ti-RSO-L30T15θ68, (h) C-Ti-RSO-L40T15θ68
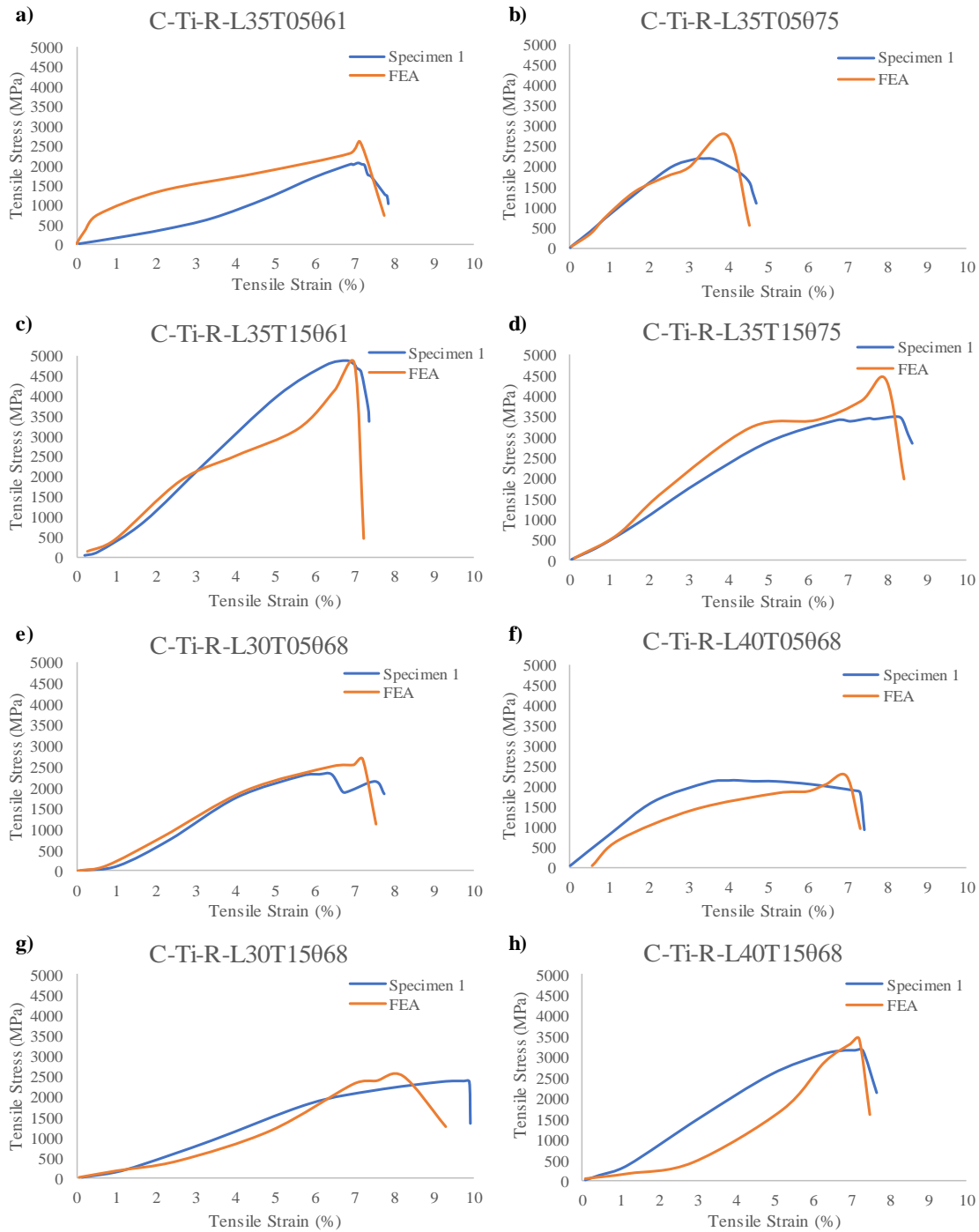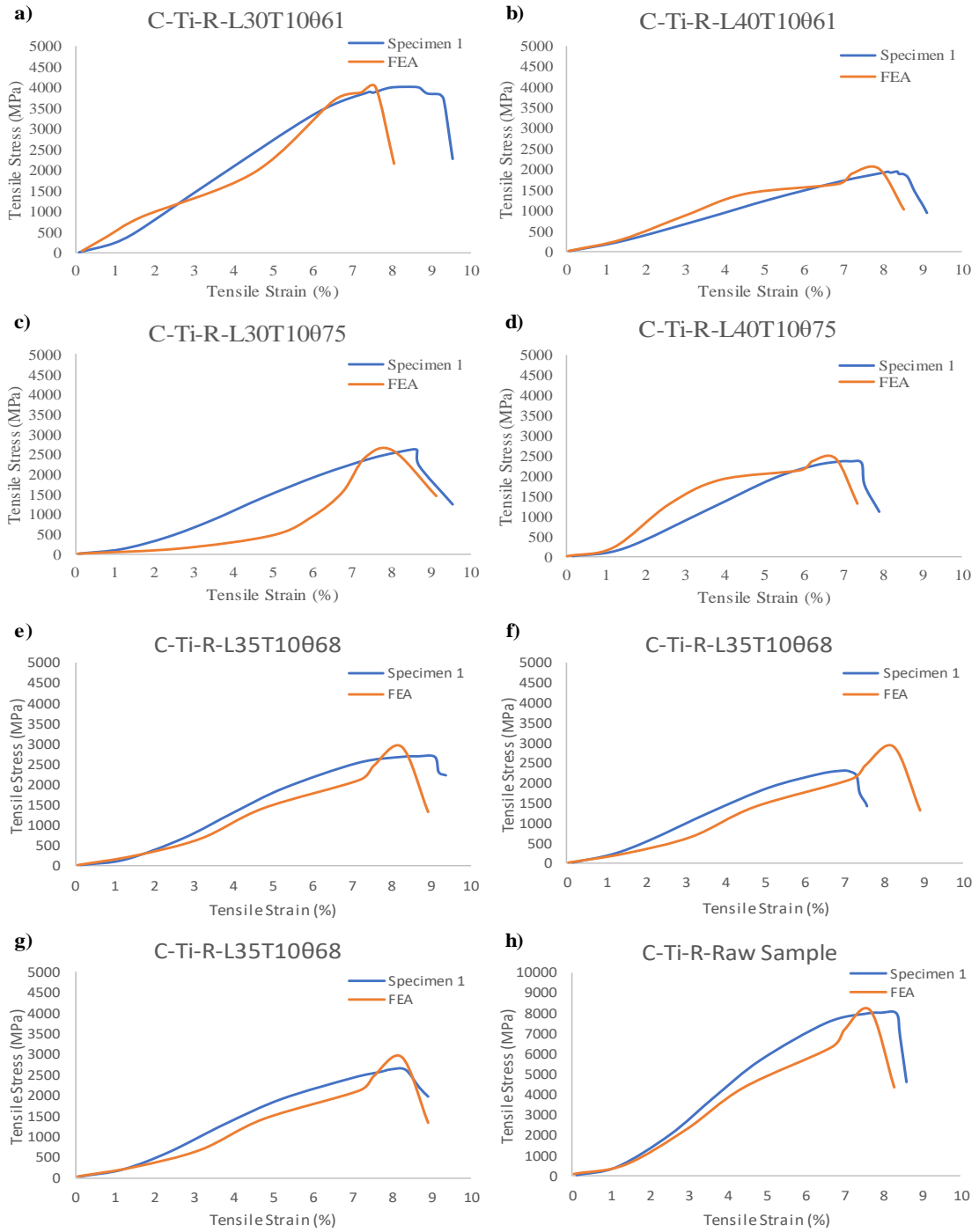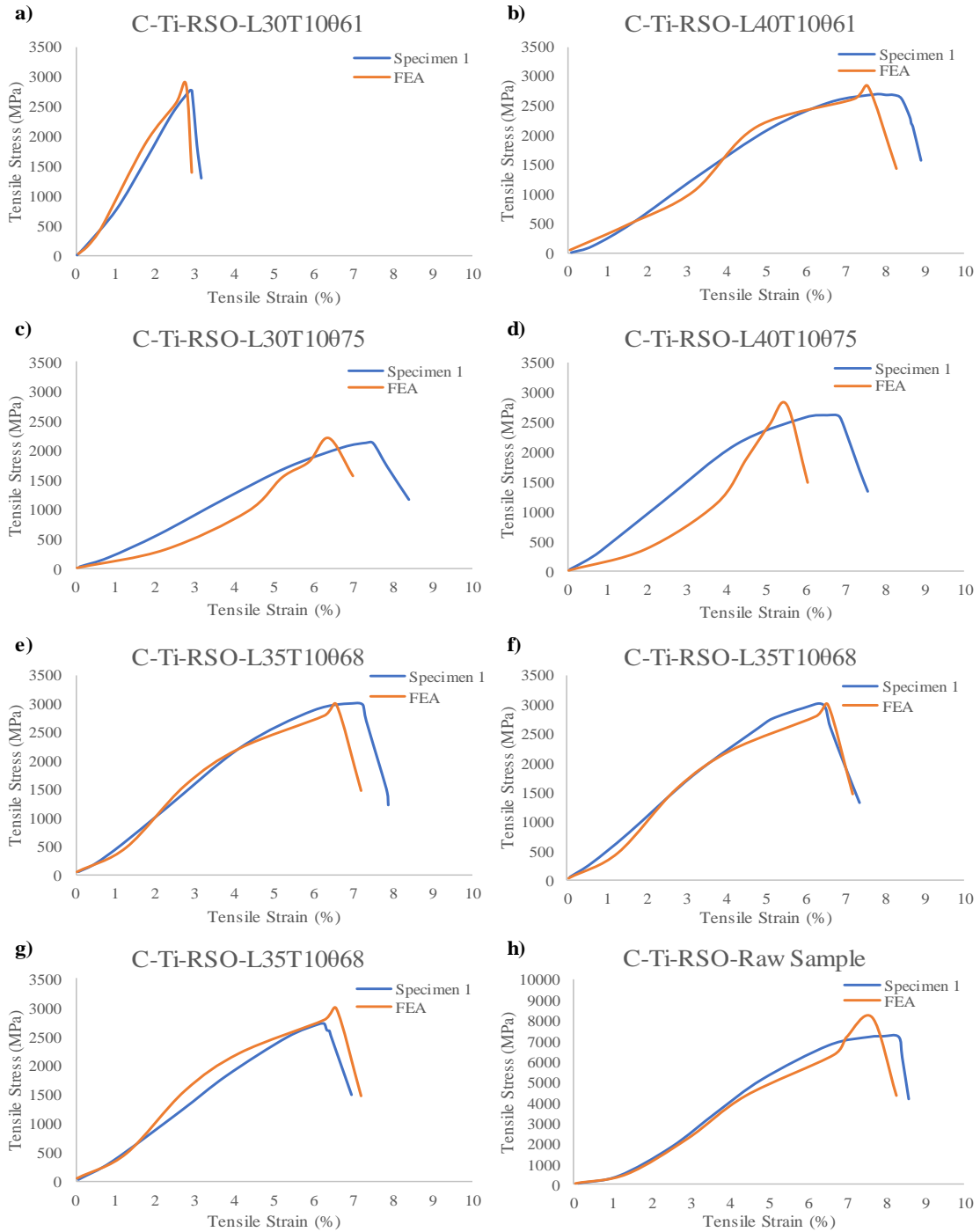
Figure 37. Experimental results of Ti6Al4V based compression specimens; (a) C-Ti-RSO-L30T10θ61, (b) C-Ti-RSO-L40T10θ61, (c) C-Ti-RSO-L30T10θ75, (d) C-Ti-RSO-L40T10θ75, (e) C-Ti-RSO-L35T10θ68, (f) C-Ti-RSO-L35T10θ68, (g) C-Ti-RSO-L35T10θ68, (h) C-Ti-RSO-Raw Sample

93

4.1.3 Statistical Analysis of Experiment Results

Experiment results were analyzed with the help of IBM SPSS statistical program and the parameter with the highest effect on the results was determined. Accordingly, the effect factor values of the unit cell parameters on the mechanical properties of the tensile and compression samples are shown in Table 23. When impact factors are examined, it is seen that the variable that most affects the tensile strength values of the samples is the **t** (thickness of the ligaments) variable. On the other hand, it is seen that the parameter that has the least effect on the tensile strength of the samples is the variable **A** (angle between ligaments).

Table 23. Impact factor values of unit cell parameters

Variables	t	L	θ	t*L	t*θ	L*θ
T-P-R	0.597	0.182	0.02	0.842	0.865	0.276
T-P-RSO	0.591	0.001	0.099	0.653	0.966	0.186
C-P-R	0.114	0.434	0.019	0.942	0.912	0.836
C-P-RSO	0.46	0.146	0.224	0.657	0.786	0.505
T-Ti-R	0.297	0.115	0.238	0.982	0.922	0.367
T-Ti-RSO	0.384	0.296	0.097	0.977	0.702	0.376
C-Ti-R	0.376	0.109	0.126	0.78	0.73	0.415
C-Ti-RSO	0.318	0.2	0.192	0.663	0.962	0.608
Average Values	0.392	0.185	0.126	0.812	0.855	0.446

When the analysis results were examined, it was observed that the thickness value of the ligaments forming the unit cells has the highest effect on the tensile or compressive strengths of the samples. In addition, it is seen that the multiplied value of the variables of ligament thickness and cross-sectional area of the unit cell has the highest effect factor value on Young's strength values of the samples. On the other hand, a deviation caused by the combination of ligament thickness and angle variables of the unit cells led to the largest average effect factor in Young's strength values of the samples.

As a result, among the parameters that constitute the two different unit cells discussed in this study, the parameter that has the most effect on the strength values of the unit cells was determined as ligament thickness. Then, the length value of the cross-sectional area of the unit cell was determined as the second parameter with the most impact. The parameter that has the least effect on the mechanical strength values of the samples is the ligament angle value variable.

Based on the impact factor data obtained as a result of the analysis, the scenarios that may occur in the strength values of the samples as a result of the variations in the parameters are given below.

• If the length of the cross-sectional area increases ⟶ Strength value of sample decrease

• If the thickness of the ligament increase ⟶ Strength value of sample increase as well

• If the angle of the ligament increases ⟶ Strength value of sample increase at smaller values of ligament thickness, decrease at larger values of ligament thickness

• The comparison chart showing which parameter affects the strength values of the samples more in case the parameters change is as follows.

Change in the thickness of the ligament > Change in the length of the cross-sectional area > Change in the angle of the ligament.

4.2 Structural Analysis

4.2.1 Microhardness Analysis

The micro-hardness distribution of PLA and Ti6Al4V based samples are given in Table 24. The microhardness of the as-received PLA is around 86.72 ± 6.22 HV while the microhardness value of Ti6Al4V is 315.72 ± 5.37 HV. When the microhardness values obtained in the study are examined, they show compatibility with the data obtained in other studies in literature. For instance, in a study by Yan et al., the microhardness value of Ti6Al4V material was found as 327.4 ± 6.1 HV [74]. This value shows a difference of approximately 3% when compared to the average microhardness value obtained in this study. Furthermore, in another study by Edwards and Ramulu, the microhardness value of Ti6Al4V metal was observed as 315.1 HV [75].

Table 24. Microhardness values of PLA and Ti6Al4V based tension and compression specimens

Sample Code	Vickers Microhardness (HV)	Average Value (HV)
T-P-R	87.35	91.12 ± 5.33
T-P-RSO	94.89	
C-P-R	84.98	82.32 ± 3.76
C-P-RSO	79.66	
T-Ti-R	321.15	319.02 ± 3.01
T-Ti-RSO	316.89	
C-Ti-R	304.32	311.42 ± 10.04
C-Ti-RSO	318.52	

4.2.2 FTIR Analysis

The FTIR spectra of pristine PLA are shown in Figure 38. For C=O stretching (peaks of ester), $-CH_3$ asymmetric (stretching group), $-CH_3$ symmetric (stretching group), and C-O stretching, the PLA exhibits distinctive stretching frequencies at 1747.00, 2996.21, 2945.47, and 1079.76 cm^{-1}, respectively. It has been determined that the bending frequencies for $-CH_3$ asymmetric and $-CH_3$ symmetric are 1452.00 cm^{-1} and 1381.00

cm^{-1}, respectively [76]. This thesis study aimed to investigate PLA characteristic behavior that corresponds to literature studies results in terms of Fourier Transform Infrared analysis.
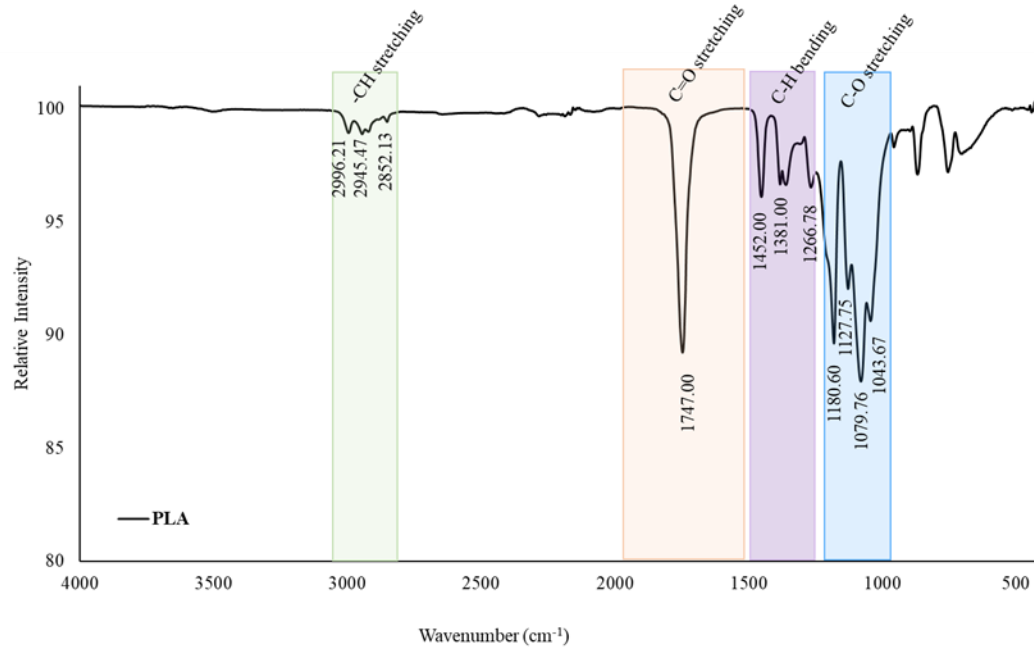
Figure 38. Fourier transform infrared (FTIR) spectra of PLA.

The Figure 39 depicts the FTIR spectra of Ti6Al4V. The spectra show peaks around 3759.25 cm^{-1} for the O-H stretching vibrations and 3651.43 cm^{-1} for the bending vibrations of the adsorbed water molecules. Additionally, tension can be indicated by the peak range absorption band at 3651.43 cm^{-1}. As the calcination temperature increases, the intensity of these peaks lowers, indicating that a significant amount of the water that had been adsorbed by TiO$_2$ has been removed (not shown in the figure) [77]. The principal transmittance peaks in the spectrum are located at 2640.30 cm^{-1}, 2551.42 cm^{-1}, 1365.40 cm^{-1}, and 1036.26 cm^{-1}, respectively, and are connected to C-H stretching, CH$_2$ symmetry stretching, CH$_2$ bending deformation, and C-O swing in-plane vibration [78]. Moreover, the Ti-O tension band is indicated by the peak at 667.78 cm^{-1}, which also relates to the distinctive peak of TiO2 [79].
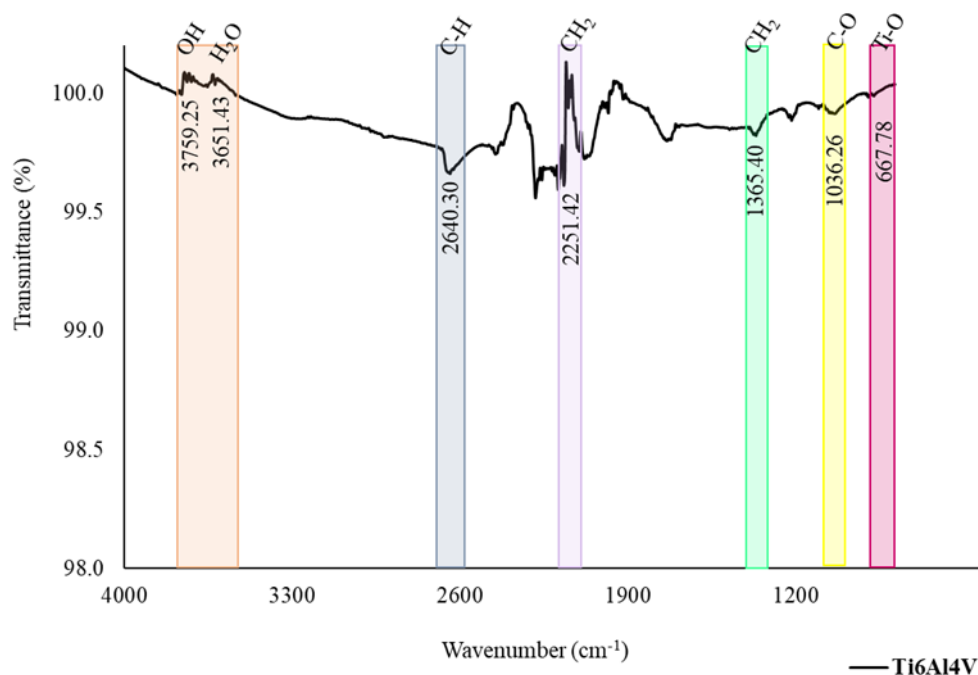
Figure 39. Fourier transform infrared (FTIR) spectra of Ti6Al4V.

4.2.3 XRD Analysis

By using XRD, the structures of pure PLA were examined in Figure 40. The peak intensities seen in the XRD patterns in (semi)crystalline/(semi)crystalline polymer blends typically vary on the concentration of each polymer. The pristine PLA's XRD pattern in the current investigation displayed two distinct peaks at 2θ, 16°, and 29.8° [80]. Analysis revealed an intensity with such a broad peak at about 2θ=16º, confirming that the PLA did not undergo a polymorphic crystalline transition [81] and also can be related to PLA's semi crystalline structure. The structure cannot be amorphous because the PLA did not exhibit any distinctive peaks [82]. For PLA, it was found that the diffraction intensity peaks at about 2θ=29.8º [83] and the strength of this peak varied.

XRD patterns of the samples mainly show -Ti peaks, which is typical for Ti-6Al-4V. It also is understood that the two phases that have been discovered are α and βTi [84].

According to the Fig., the Ti-6Al-4V substrate was responsible for the main standard Ti peaks at 2θ values of 36.08 °, 39.51 °, and 43.29 ° [85]. The plane of aluminum oxide (Al_2O_3, the most intense diffraction for corundum) is thought to be responsible for the peak near 2θ=43.29°. Since there were no further phases found by XRD, can be indicated that the space-holder was entirely eliminated and that there was no chemical reaction or contamination during the sintering cycle's decomposition [84].
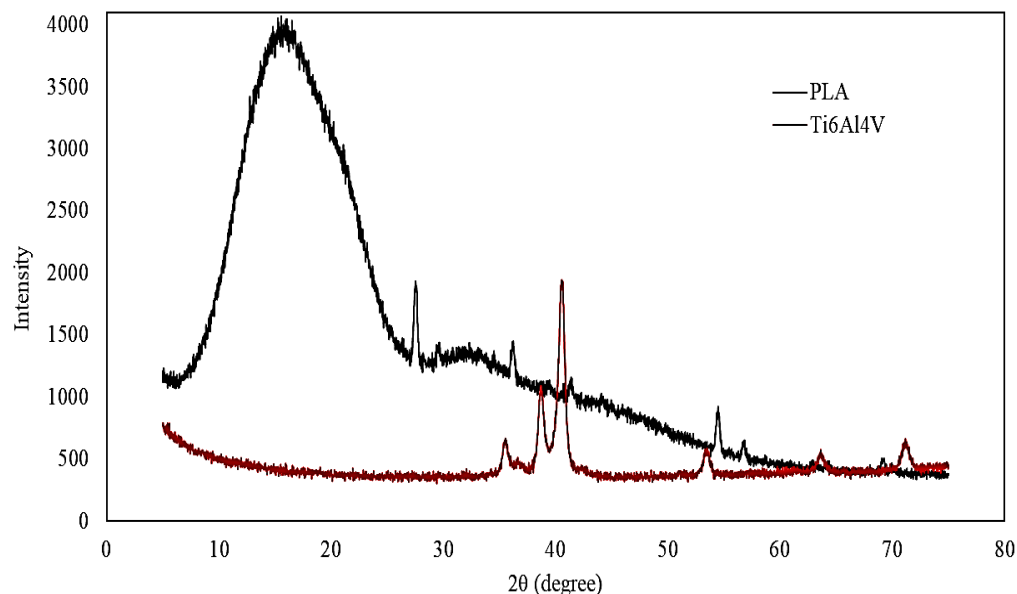
Figure 40. XRD patterns of PLA polymer and Ti6Al4V alloy.

4.3   Mechanical & Thermal Analysis

4.3.1   TGA & DSC Analysis

DSC analysis results of PLA-based samples are shown in Figure 41. According to the results, the glass transition temperature (T_g) of PLA material was observed as 60 °C. In addition, it is seen that PLA begins to crystallize at a temperature of 126.5 degrees (T_c). In addition, the cold crystallization temperature of PLA indicates that the sample has a semi-crystalline structure. It was determined that the sample started to melt at a

temperature value of 154.8 degrees (T_m). The highest melting rate of the PLA-based sample is observed at 368.5 degrees, which is the maximum degradation value.

According to studies in literature, in a study investigating the optimization of PLA and ABS materials for 3d printers, the T_g value of the PLA material was found to be 62.1 °C, and the T_m value was 151.77 °C [86]. Considering the fact that the PLA filaments used in the two studies are different brands, it can be concluded that these values are compatible with the values in this study. In another study examining the thermal and mechanical properties of PLA and another composite material with silicon additives, the T_g value of PLA material was 56.1 °C, T_c value was 110.1 °C, and T_m value was 151.66 °C [87]. It is thought that the reason of the difference in temperature values in these studies is due to the difference in the production and utilization conditions of the PLA material used. In another study examining the microstructures of carbon nanotube / PLA composites used in the additive manufacturing method, the highest melting rate of PLA was measured as 374 °C [88]. To sum up, it is observed that the results of this thesis study are in accordance with the results of the studies in the literature.
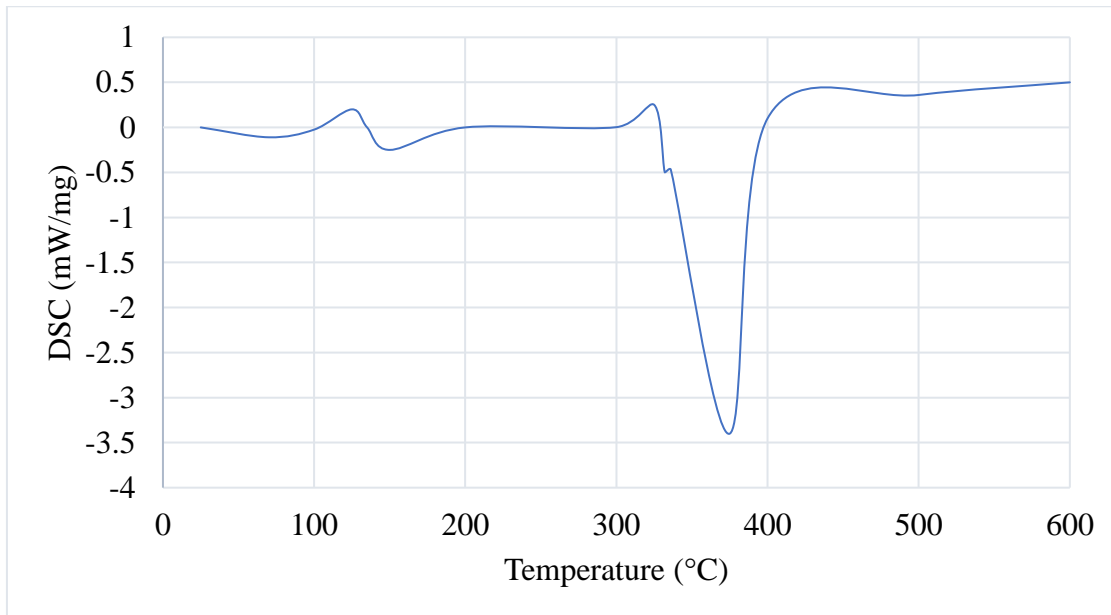
Figure 41. Differential Scanning Calorimetry Analysis of PLA

TGA results of PLA-based samples are shown in Figure 42. At this point, the TGA results can be interpreted together with the DSC results. In this context, when the curve indicated by the blue colored line in Figure 42 is examined, the fact that the PLA material progresses almost horizontally before it starts to melt shows that the sample is thermally stable and the moisture content is low which means dry. According to the results, it was determined that the sample started to melt at a temperature value of 154.8 °C (T_m).

When the studies in the literature were examined, in a study examining the thermal properties of PLA material, the temperature at which the melting rate reached the maximum value was measured as 349 °C [89]. In another study where TGA measurement of PLA material was made, this value was measured as 382.4 °C degrees [90]. In another study by Zheng et al., this value was found to be 360 °C [91]. When the results of the studies in the literature and the PLA-based samples analyzed in this thesis are compared, it is seen that the results obtained in this study are in accordance with the literature.
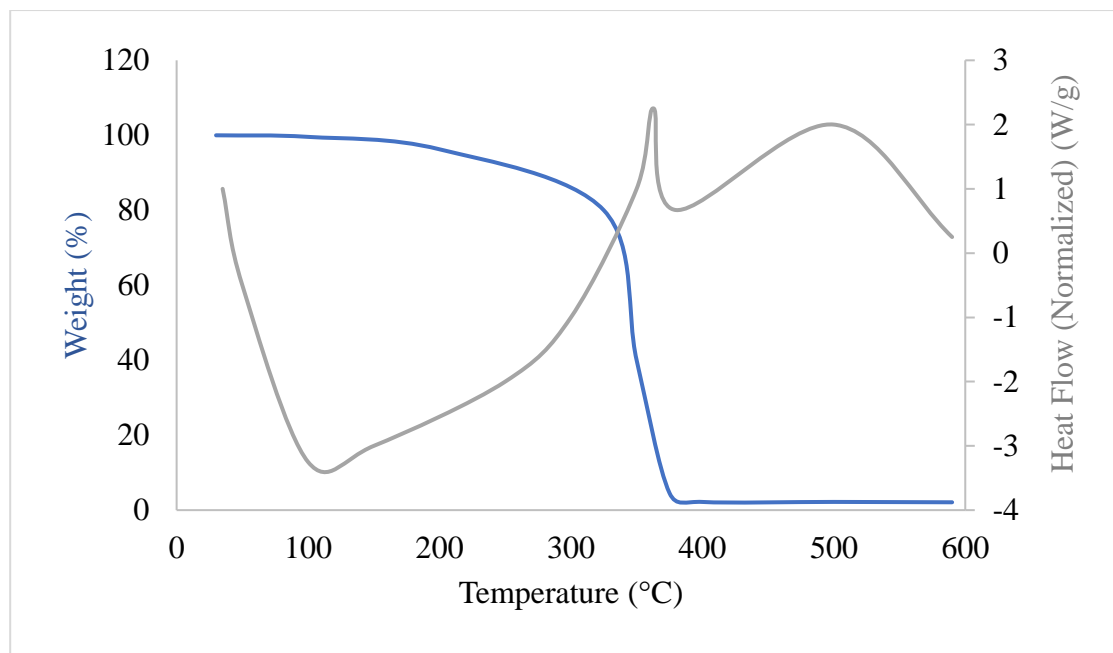
Figure 42. Thermogravimetric Analysis of PLA

4.3.2 SEM Analysis

SEM images of as received and tested PLA samples are shown in Figure 43. The surface of the PLA plate as admitted is fairly smooth as shown in Figure 43 (b). The zigzag tendency of stress-strain curves was influenced further by the layer-by-layer printing of FDM.

Figure 43. SEM images showing cross sectional morphology of PLA samples after experiments; (a) 100x magnitude SEM image of PLA sample, (b) 10000x magnitude SEM image of PLA sample, (c) EDS Spectra of PLA

SEM images of as received and tested PLA samples are shown in Figure 43. The surface of the PLA plate as admitted is fairly smooth as shown in Figure 43 (b). The zigzag tendency of stress-strain curves was influenced further by the layer-by-layer printing of FDM.

Voids can be occurring in 3D printed components as a result of inadequate bonding between adjacent particles during the deposition process [92]. The various placements of these porous cracks cause varying fracture propagation pathways in these structures. Furthermore, as demonstrated in Figure 43, the pores caused internal cavities in structure. Due to the poor intermolecular interactions between the fibers and the polymer matrices, the void defects can create additional residual stress as weak spots inside the manufactured sample.

EDS Spectra of as received and tested thin films are shown in Figure 43 (c). The EDS spectrum in Figure 43 (c) demonstrated that the PLA utilized as a substrate is essentially constituted of C-Kα. The presence of rough surface on the sample was corroborated by the EDS spectra in Figure 43 (c). Furthermore, O and Au peaks were discovered.

SEM images of as received and tested Ti6Al4V samples are shown in Figure 44. EDS Spectra of as received and tested Ti6Al4V thin films are shown in Figure 44 (c). The EDS spectrum in Figure 44 (c) demonstrated that the Ti6Al4V utilized as a substrate is essentially constituted of TiKα. The presence of rough surface on the sample was corroborated by the EDS spectra in Figure 44 (c). Furthermore, Si and Al peaks were discovered.
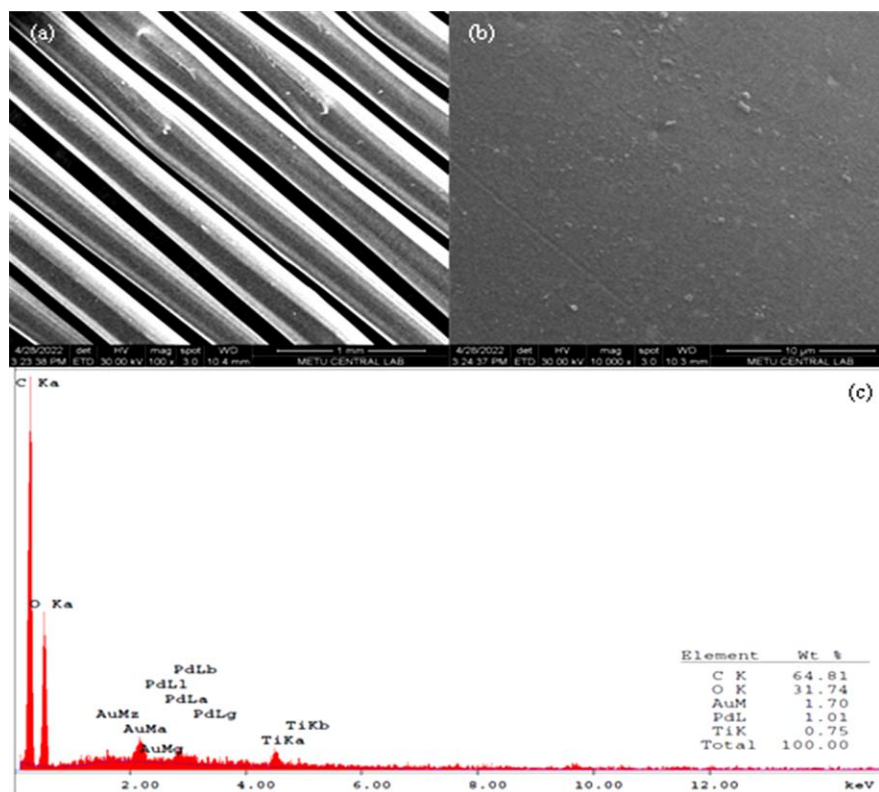

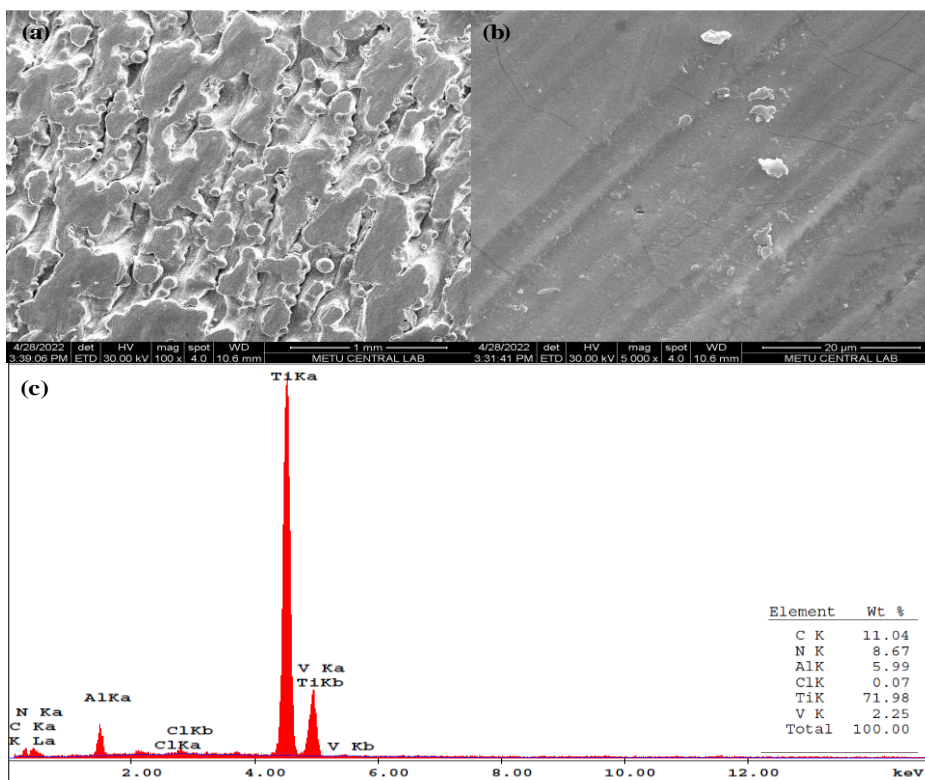
Figure 44. SEM images showing cross sectional morphology of Ti6Al4V samples after experiments; (a) 100x magnitude SEM image of Ti6Al4V sample, (b) 5000x magnitude SEM image of PLA sample, (c) EDS Spectra of Ti6Al4V

4.4   Numerical Analysis (FEA)

In literature, most of the studies have analyzed the samples numerically via various computer software in an attempt to validate the experimental data. Finite Element (FE) models have been generally constructed via Abaqus® or ANSYS Benchmark platforms. In order to constitute simulations, mesh needs to be created, consisting of up to millions of tiny pieces which ideally constitute the shape of the structure. Thus, calculations can be performed for each single element and, by combining these individual results, final result of the structure can be obtained. Thereafter, the boundary conditions of the model should be determined and assigned. At this point, boundary conditions may be different depending on the test methods to be applied in the simulation. In this section, particular numerical solutions were conducted which compare the experimental results of lattice geometry structures according to finite element simulations and analytical predictions. At this point, examinations were conducted on 120 different samples. Numerical results of whole samples are given in between Figure 45 and Figure 52.

When the literature was examined, a study that investigated the mechanical properties of re-entrant geometries with finite element analysis, tensile strength value of the sample with a vertical length of 100 mm, a horizontal length of 100 mm, and a branch angle of 45 degrees was found to be 205.1 MPa. [48]. Furthermore, in another study, the tensile strength of lattice geometries with a vertical length of 8 mm, a horizontal length of 12 mm, and a branch angle of 45 degrees was measured as 6,45 MPa [43]. Moreover, in another study, the tensile strength of lattice geometries with a vertical length of 20 mm, a horizontal length of 10 mm, and a branch angle of 30 degrees was measured as 2,43 MPa [94]. Lastly, in a study, the compressive strength of lattice geometries with a vertical length of 10 mm, a horizontal length of 5 mm, and a branch angle of 60 degrees was measured as 57,5 MPa [40].
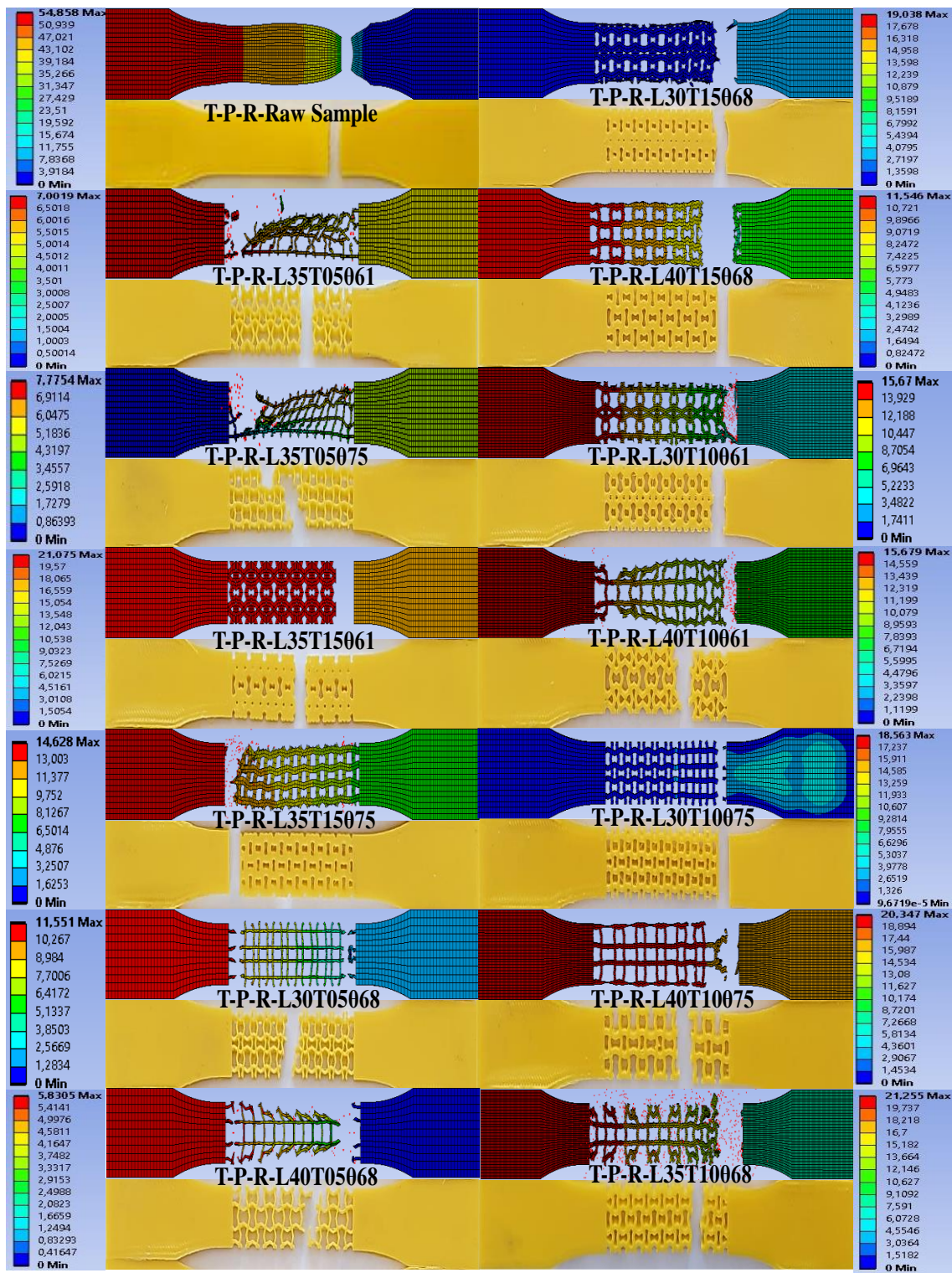
Figure 45. FEA results of PLA based tension specimens

Figure 46. FEA results of PLA based tension specimens
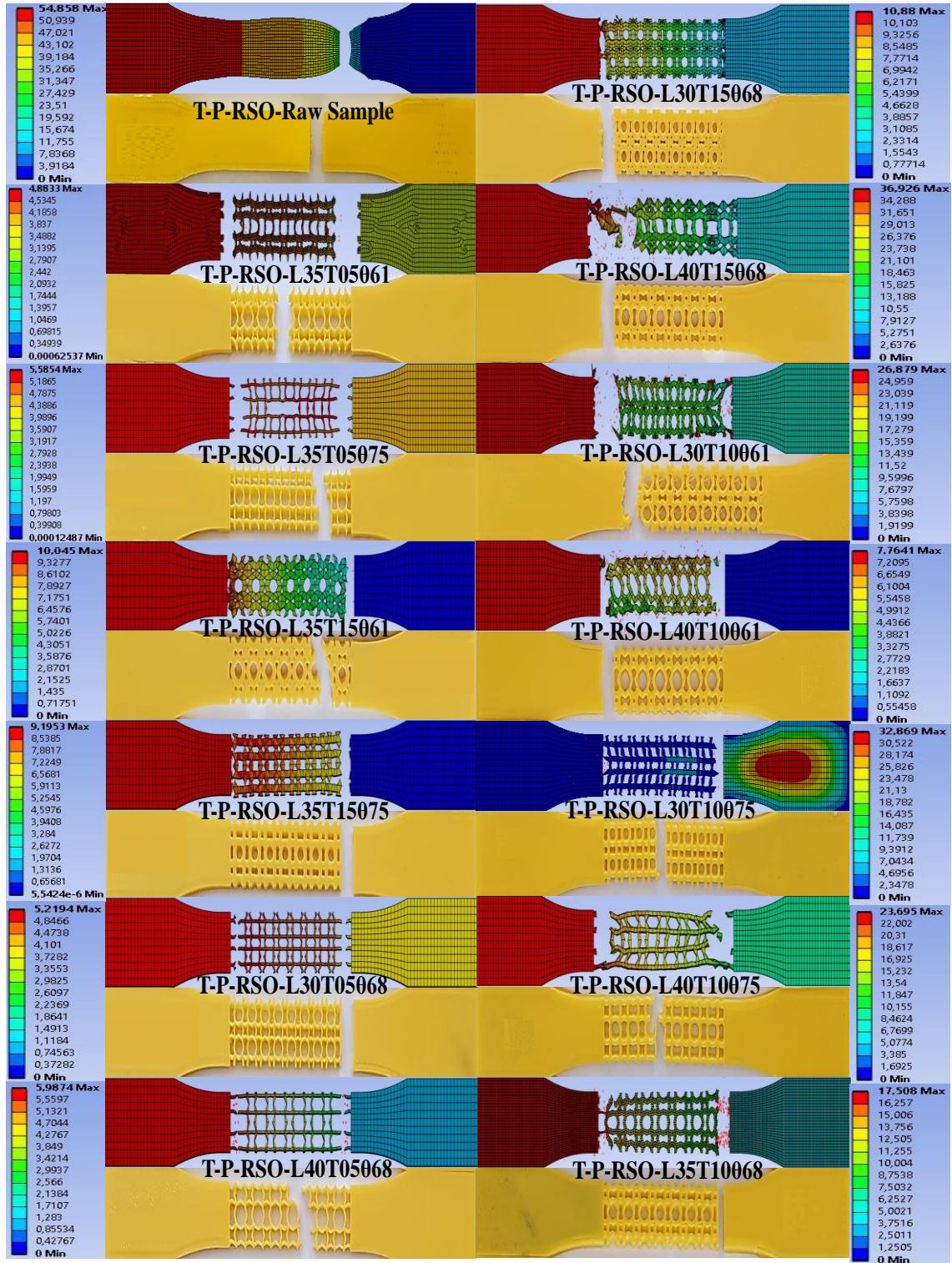
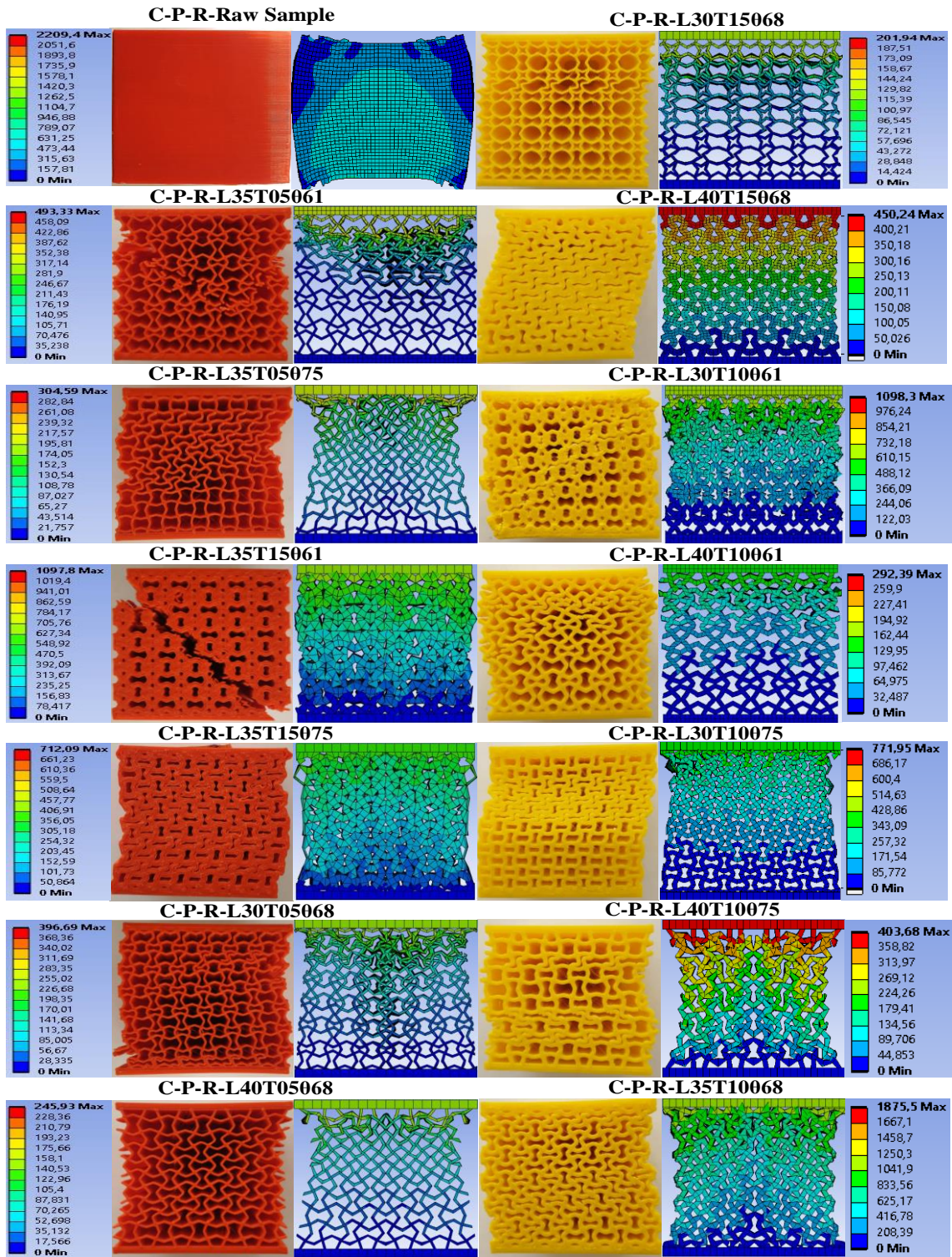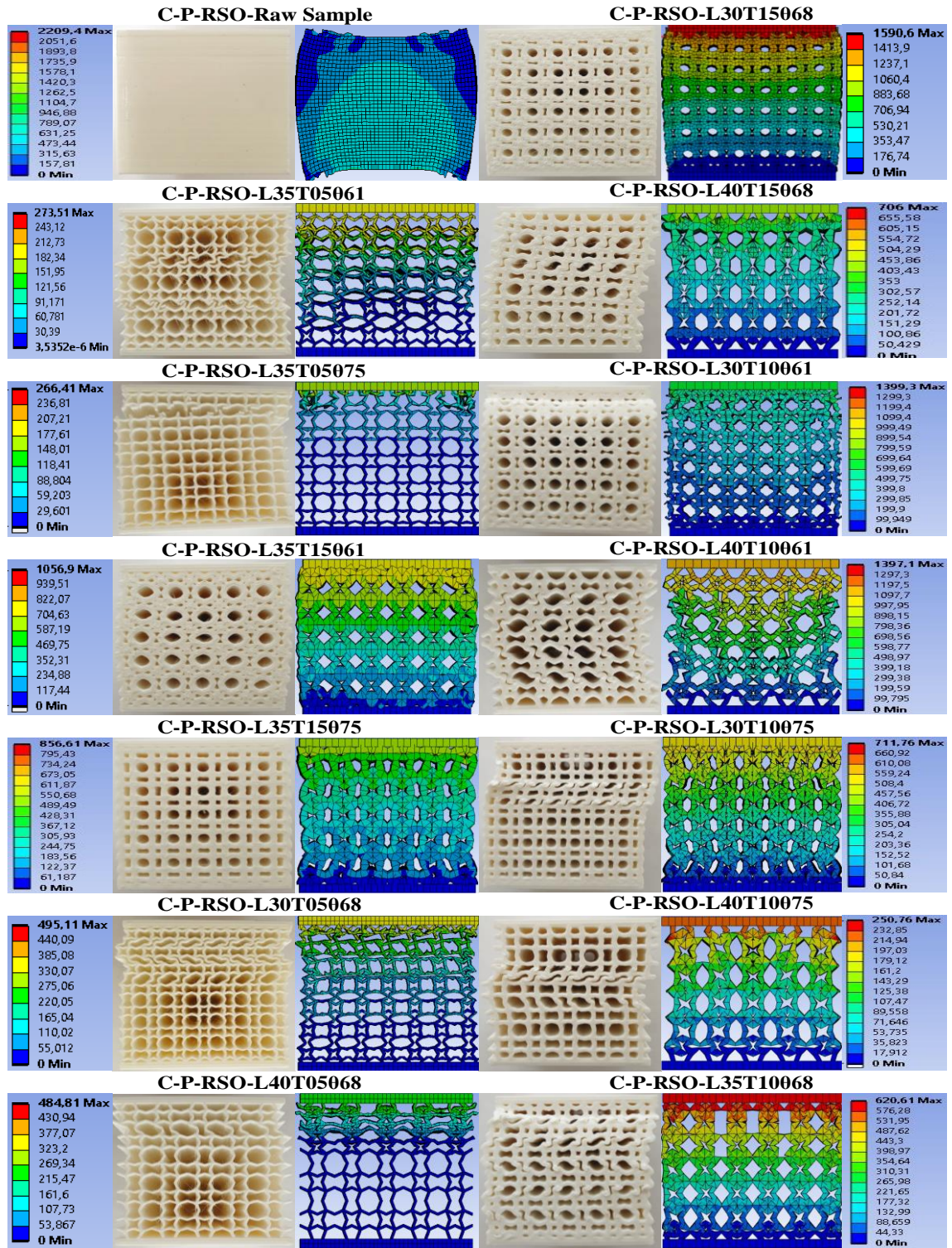**Figure 47.** FEA results of PLA based compression specimens

Figure 48. FEA results of PLA based compression specimens
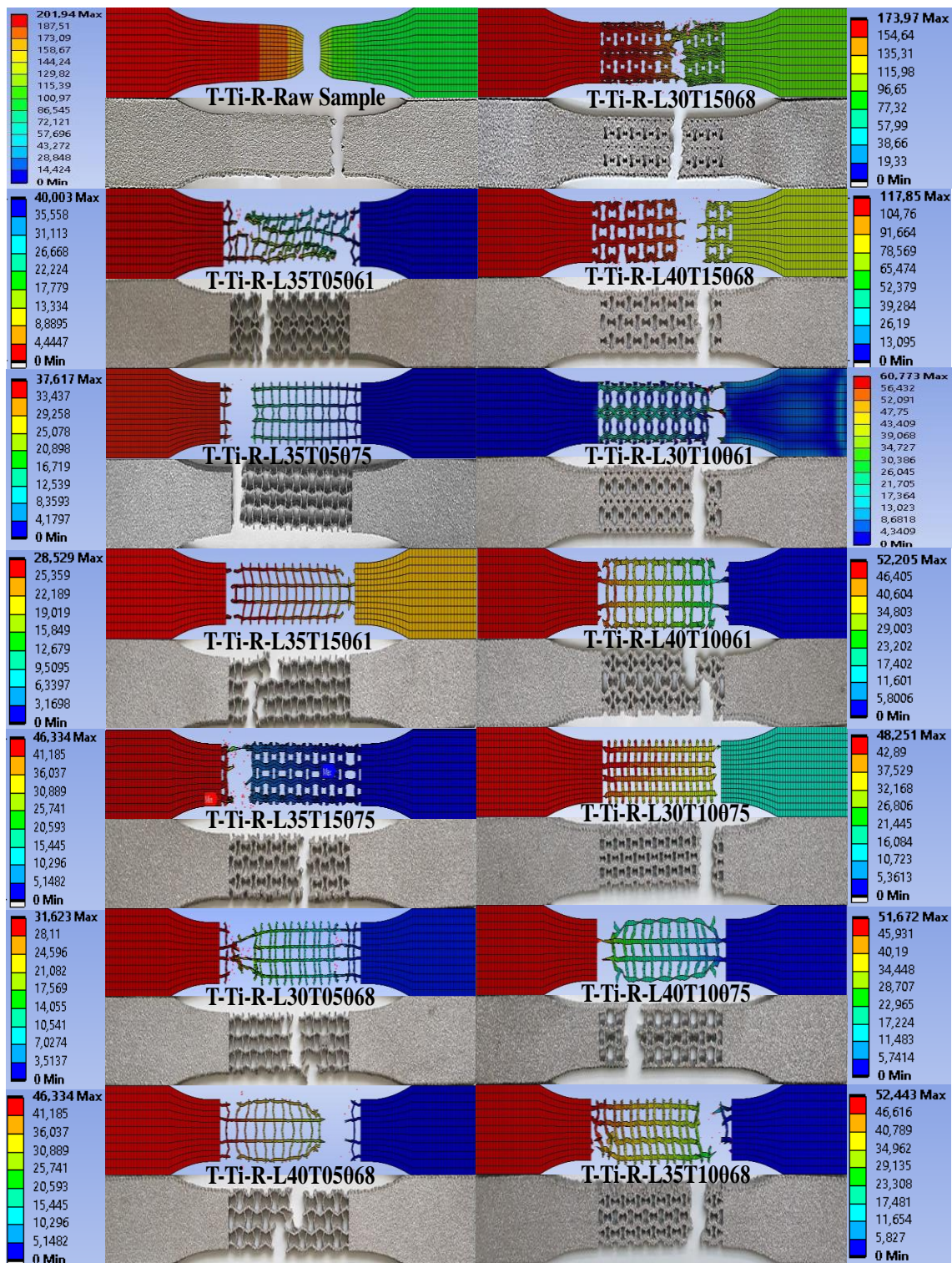
Figure 49. FEA results of Ti6Al4V based tension specimens
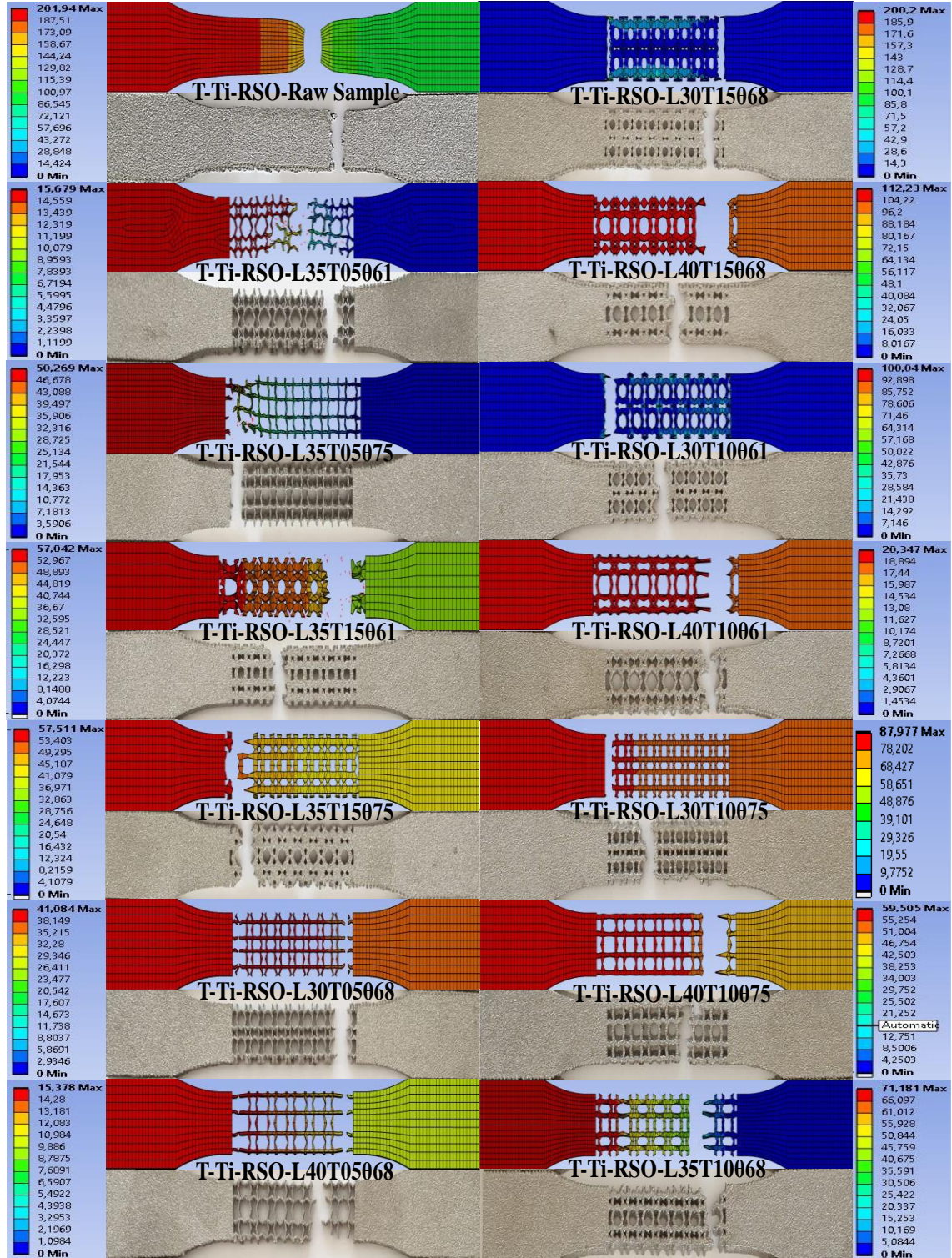
Figure 50. FEA results of Ti6Al4V based tension specimens

111
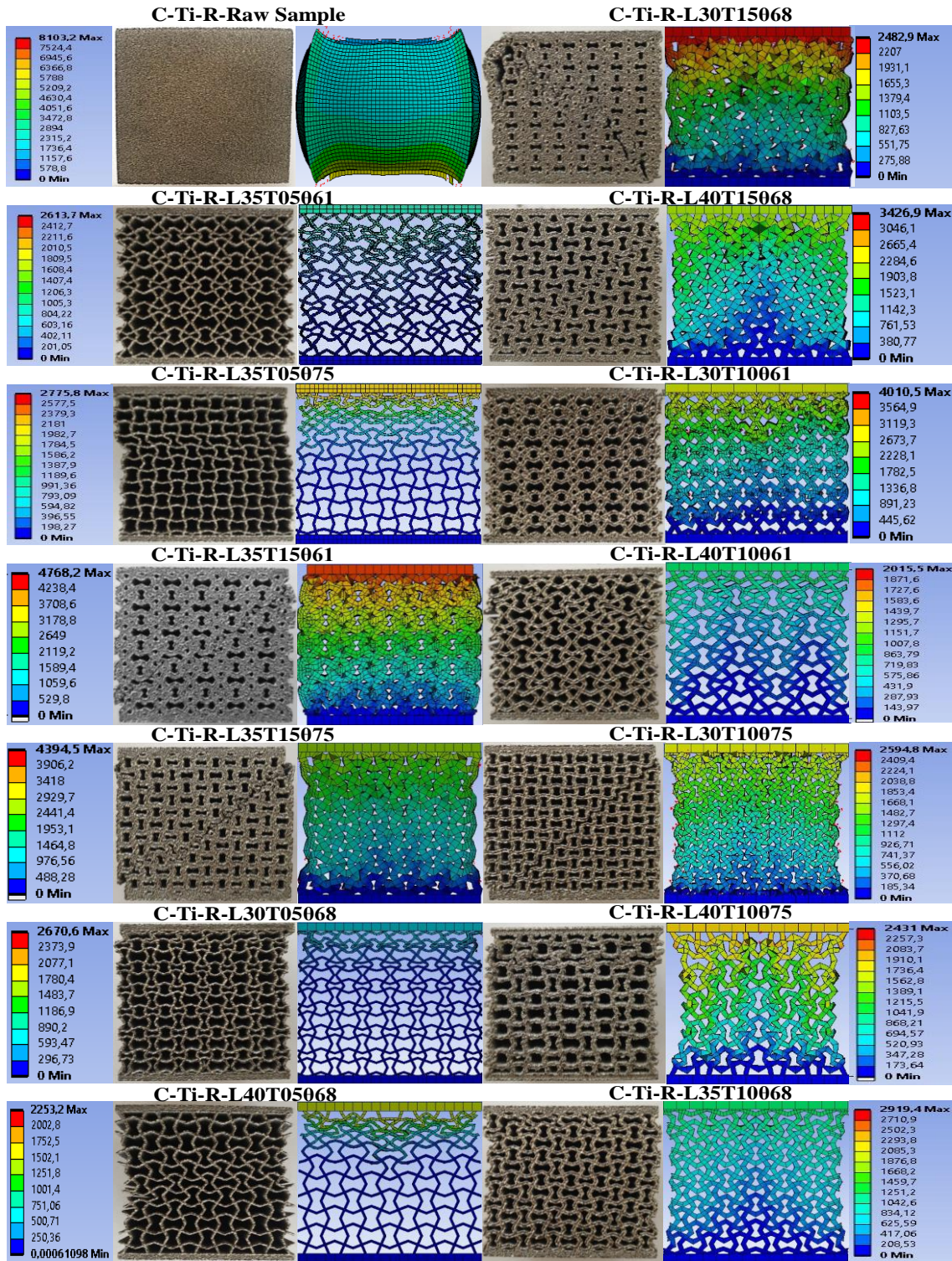
Figure 51. FEA results of Ti6Al4V based compression specimens
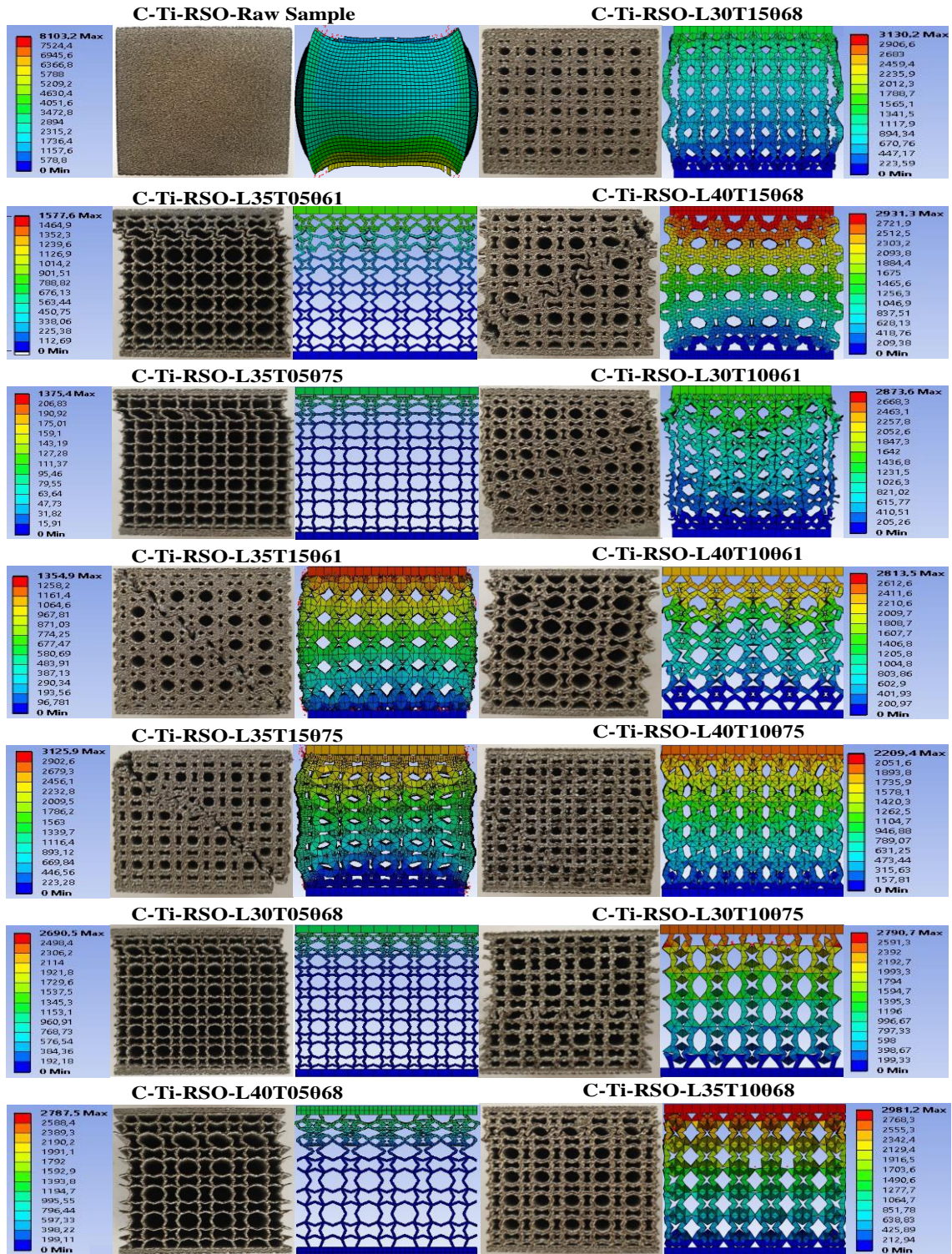
Figure 52. FEA results of Ti6Al4V based compression specimens

In literature, most of the studies have analyzed the samples numerically via various computer software in an attempt to validate the experimental data. Finite Element (FE) models have been generally constructed via Abaqus® and ANSYS Benchmark platforms. In order to constitute simulations, mesh needs to be created, consisting of up to millions of tiny pieces which ideally constitute the shape of the structure. Thus, calculations can be performed for each single element and, by combining these individual results, final result of the structure can be obtained. Thereafter, the boundary conditions of the model should be determined and assigned. In this point, boundary conditions may be different depending on the test methods to be applied in the simulation. In this section, particular studies were examined which compare the experimental results of lattice geometry structures according to finite element simulations and analytical predictions. At this point, examinations were conducted on six different studies which consist of detailed mechanical properties of lattice structures.

To compare experimental and numerical results, a comprehensive investigation of deformation process of the samples was performed. It can be said that, the deformation behaviors of the samples in the experimental environment and the numerical environment were quite similar. A deviation between the experimental results and the numerical results is determined around 10-15%.

Table 25 represents comparison of mechanical properties of lattice geometry structures with three subsections. Most of the studies in literature, consist of experimental results with the finite element simulations and analytical approaches. However, many of the parameters and results that are obtained from simulations and predictions were not included to studies in this context, the most detailed studies were listed which comprehensively compare the experimental data with the results of both simulations and analytical approaches. The studies of Quan et al., Auricho et al., and Fu et al., showed the comparisons in a detailed way [36, 93, 94]. At this point, researchers compared the data they obtained as a result of their experiments with both the data they obtained from simulation environment and from analytical approaches.

114

Table 25. Comparison of in-plane properties of lattice geometry structures produced with various materials

Reference	Lattice Type	FEA Results		Experimental Results		Comparison
		Tensile Strength σ (MPa)	Poisson Ratio (υ)	Tensile Strength σ (MPa)	Poisson Ratio (υ)	Error δυ (%)
[36]	Re-entrant	34,02	-0,92	31,95	-0,89	6,48
[93]	Tetra-Chiral	2,26	0,27	0,94	0,26	4
[94]	Tetra-Chiral	1.16	-0.84	0.54	−0.94	10.20
[95]	Anti-Tetra-Chiral	828.31	-0.95	839.55	-0.93	2.15
[96]	Re-entrant	1489,36	-0.53	700	-1	47
[97]	Peanut Hole	4,53	−1,177	-	-1,107	6,36

On the other hand, although in most of the studies compared the experimental results with numerical and analytical results, the data obtained are not specified numerically. For instance, in the study of Yao et al., although the estimations and evaluations conducted pursuant to the numerical analysis results were consistent with the experimental results, there was discrepancy between the FEA results and the experimental results for the samples used [98]. It was concluded that the Poisson ratio, hardness and strength values calculated by FEA were higher than the values obtained as a result of the experiments. In this context, obtained data were interpreted graphically instead of numerically. Additionally, Simpson and Kazancı conducted a comparison between the deformation patterns observed experimentally and obtained computationally through the FE simulations for each of the tubes and obtained data were presented as force-displacement curves for each TW tube [99].

To compare experimental and numerical results, a comprehensive investigation of deformation process of the samples was performed. All figures in between the Figure 45 and Figure 52 compare the results of both unit cells for this purpose. These findings illustrate the deformation patterns of various structural types as well as the impact of material reinforcing. Each cell design comprises an initial elastic region with a linear stress-strain curve as each cell deforms consistently.

When all the data obtained in general are examined, there are differences between the experimental results and the simulation results. The reasons for these deviations can be shown as the low quality of the filament used during the production of the samples, the performance of the 3d printer used, the lack of sensitivity during production, the produced sample not being stored under appropriate storage conditions, the incorrect calibration of the experimental setup, the gripper jaws not tight enough, rolling and cutting errors, etc. In addition, situations such as insufficient computer processors, mesh quantity, and quality that cannot meet the desired conditions can be shown among the reasons for the existing differences.

When the literature is examined, Fu et al., investigated the compressive behavior of Ti6Al4V based compression specimens which are composed of re-entrant structure. Furthermore, they obtained the compressive strength value of specimen as 700 MPa from the real-life experiments whilst the FEA result of this value is 1489,36 MPa [94]. The error between the experiments and simulations results were founded as 47%. As a result of this study, they concluded that, this huge discrepancy between experimental and simulation results might be due to misprinting issues, which also demonstrates how printing quality impacts the mechanical reactions of structures [94]. In addition to this, Ma et al., studied to compare experimental and numerical results of Ti6Al4V based and anti-tetra chiral structured compression samples [95]. As a result of the experiments, they found the compressive strength of the sample as 839.55 MPa, and as a result of the numerical modeling, they obtained the same value as 828.31 MPa [95]. At this point, the error was calculated as 2.15% in their study, and it can be concluded that, there is a small discrepancy between their results [95].

116

When this study is compared with similar studies in literature, it has been observed that the comparison results of the obtained data indicated a very low deviation. For instance, when the experimental and numerical results of PLA-based samples were compared, the mean value of the error was found as 6.42%. On the other hand, when both experimental and numerical results of Ti6Al4V-based re-entrant structured samples were compared, the mean value of the error was found as 9.99%. It is seen that these values are quite similar with the values in literature. Thus, it can be concluded that the numerical results demonstrate consistently strong agreement with the experimental results including both and accompanying displacements. Furthermore, the modeled deformations correlate with the experimental results at both the micro and macro scales. As a result, the FEA modeling methodologies applied in this study are verified.

When the results obtained are examined, although it is observed that the experimental and numerical results are consistent with each other, the differences in the numerical results show that the samples cannot be produced with 100% accuracy. This problem is due to the fact that AM methods cannot provide stable product quality. For instance, in AM methods, there are too many parameters that affect the quality of production. Production optimizations of these parameters are still not fully realized. For example, even the parameter on which coordinates of the table in the printer will produce the sample to be produced in a 3d printer greatly affects the quality of the production. In this context, this situation can be shown as the biggest reason for the deviations in the results of the experiments conducted within the scope of this thesis. In short, although AM methods make a great contribution to the conceptual design stages of projects in many fields today, they are unproven production methods that are not yet used in the parts production stages in the aviation, automotive and medical industries where critical parts are produced.

CHAPTER 5

SUMMARY AND FUTURE WORKS

In this thesis study, two different unit cells were created by using different auxetic geometries in literature. Various geometry combinations were obtained by changing the lattice geometry parameters of the cells created, and tensile and compression specimens were created using these geometries via different additive manufacturing methods. In other words, the lattice geometries were placed in two different unit cells and these unit cells were produced using FDM and EBM methods. Within the scope of this thesis, the mechanical tests of the specimens were carried out and the results obtained as a result of the tests were examined and the changes in the mechanical properties of the lattice geometry structures depending on the parameter variation were investigated. In addition, the characterizations of the manufactured samples were carried out using methods such as microhardness, relative density, FTIR, XRD, TGA & DSC and SEM. In addition, simulations were performed in numerical environment in order to verify the results obtained in the experimental environment. The results show that the mechanical strength of the specimens with the lattice geometry constituted by using auxetic geometries is higher than the mechanical strength values of the samples with the lattice geometries formed using the traditional geometries.

In future studies, the Poisson ratios of the samples can be investigated, and whether they exhibit an auxetic behavior can be examined. Besides, by increasing the number of experiments using Ti6Al4V-based samples, the deviations in the results can be better evaluated. On the other hand, the production of the samples can be carried out in a 3d printer with high calibration and resolution, low nozzle diameter, and low speeds, since the designed geometries are complex and sensitive. In addition, finite element analyzes were limited to computer processor performance. More precise results should be obtained at higher mesh quality and quantity using a more powerful computer. In future

studies, different geometry designs can be made using different auxetic structures. Moreover, each parameter (angle, edge, thickness) of the designed geometries should be investigated in detail with the help of finite element analysis. To sum up, future studies can be enriched by investigating specific features such as Poisson's ratio, bending strength, and impact strength apart from tensile and compression strength as mechanical properties.

REFERENCES

[1]   G. Rasiya, A. Shukla, K. Saran, Additive manufacturing-A review, Materials Today: Proceedings. Vol. 47, (2021), pp. 6896-6901, https://doi.org/10.1016/j.matpr.2021.05.181.

[2]   M. Jiménez, L. Romero, I.A. Domínguez, M.D.M. Espinosa, M. Domínguez, Additive manufacturing technologies: An overview about 3D printing methods and future prospects, Complexity. Vol. 2019, (2019), 9556938, https://doi.org/10.1155/2019/9656938.

[3]   Z. Liu, Q. Lei, S. Xing, Mechanical characteristics of wood, ceramic, metal and carbon fiber-based PLA composites fabricated by FDM, Journal of Materials Research and Technology. Vol. 8, (2019), pp. 3743–3753, https://doi.org/10.1016/j.jmrt.2019.06.034.

[4]   A. Bhatia, A.K. Sehgal, Additive manufacturing materials, methods and applications: A review, Materials Today: Proceedings. (2021). https://doi.org/10.1016/j.matpr.2021.04.379.

[5]   X. Gao, N. Yu, J. Li, Influence of printing parameters and filament quality on structure and properties of polymer composite components used in the fields of automotive, in: K. Friedrich, R. Walter, C. Soutis, S.G. Advani, Ing. Habil. B. Fiedler (Eds.), Structure and Properties of Additive Manufactured Polymer Components, Woodhead Publishing. Part. 2 (2020) pp. 303–330, https://doi.org/https://doi.org/10.1016/B978-0-12-819535-2.00010-7.

[6]   J.C. Najmon, S. Raeisi, A. Tovar, 2 - Review of additive manufacturing technologies and applications in the aerospace industry, in: F. Froes, R. Boyer (Eds.), Additive Manufacturing for the Aerospace Industry, Elsevier. (2019), pp. 7–31, https://doi.org/https://doi.org/10.1016/B978-0-12-814062-8.00002-9.

[7]   O. Özsolak, Eklemeli imalat yöntemleri ve kullanılan malzemeler, International Journal of Innovative Engineering Applications. Vol. 3, (2019), pp. 9–14, https://dergipark.org.tr/tr/pub/ijiea/issue/48178/570535.

[8]   S. Bodnárová, S. Gromošová, R. Hudák, J. Rosocha, J. Živčák, J. Plšíková, M. Vojtko, T. Tóth, D. Harvanová, G. Ižariková, Ľ. Danišovič, 3D printed polylactid acid based porous scaffold for bone tissue engineering: An in vitro study, Acta of Bioengineering and Biomechanics. Vol. 21 (2019), pp. 121-133 https://doi.org/10.5277/ABB-01407-2019-02.

[9]   J.H. Park, J.K. Yoon, J.B. Lee, Y.M. Shin, K.W. Lee, S.W. Bae, J.H. Lee, J.J. Yu, C.R. Jung, Y.N. Youn, H.Y. Kim, D.H. Kim, Experimental tracheal replacement using 3-dimensional bioprinted artificial trachea with autologous epithelial cells and chondrocytes, Scientific Reports. Vol. 9 (2019), pp. 2103-2114, https://doi.org/10.1038/s41598-019-38565-z.

[10]   M. Dawoud, I. Taha, S.J. Ebeid, Mechanical behaviour of ABS: An experimental study using FDM and injection moulding techniques, Journal of Manufacturing Processes.   Vol.   21,   (2016),   pp.   39–45. https://doi.org/10.1016/j.jmapro.2015.11.002.

[11]   A.P. Valerga Puerta, D.M. Sanchez, M. Batista, J. Salguero, Criteria selection for a comparative study of functional performance of Fused Deposition Modelling and Vacuum Casting processes, Journal of Manufacturing Processes. Vol. 35, (2018), pp. 721–727. https://doi.org/10.1016/j.jmapro.2018.08.033.

[12]   ASTM F2792-12, Standard Terminology for Additive Manufacturing Technologies, ASTM International. West Consh (2012).

[13]   O.A. Mohamed, S.H. Masood, J.L. Bhowmik, Optimization of fused deposition modeling process parameters: a review of current research and future prospects, Advances   in   Manufacturing.   Vol.   3,   (2015),   pp.   42–53. https://doi.org/10.1007/s40436-014-0097-7.

[14]   J.S. Chohan, R. Singh, K.S. Boparai, R. Penna, F. Fraternali, Dimensional accuracy analysis of coupled fused deposition modeling and vapour smoothing operations for biomedical applications, Composites Part B: Engineering. Vol. 117, (2017), pp. 138–149, https://doi.org/10.1016/j.compositesb.2017.02.045.

[15]   X.T. Wang, B. Wang, X.W. Li, L. Ma, Mechanical properties of 3D re-entrant auxetic cellular structures, International Journal of Mechanical Sciences. Vol. 131–132 (2017), pp. 396–407, https://doi.org/10.1016/j.ijmecsci.2017.05.048.

[16]   J.Z. Manapat, Q. Chen, P. Ye, R.C. Advincula, 3D printing of polymer nanocomposites via stereolithography, Macromolecular Materials and Engineering. Vol. 302 (2017), https://doi.org/10.1002/mame.201600553.

[17]   R. Anitha, S. Arunachalam, P. Radhakrishnan, Critical parameters influencing the quality of prototypes in fused deposition modelling, Journal of Materials Processing Technology. Vol. 118, (2001), pp. 385–388, https://doi.org/10.1016/S0924-0136(01)00980-3.

[18]   D.L.D. Bourell, J.J. Beaman, M.C. Leu, D.W. Rosen, A brief history of additive manufacturing and the 2009 roadmap for additive manufacturing: looking back and looking ahead, US-Turkey Workshop, (2009).

[19]   L.J. Zukor, Nature and properties of engineering materials. Z. D. Jastrzebski. Wiley, New York-London, Journal of Applied Polymer Science. Vol. 4, (1960), pp. 372-373, https://doi.org/10.1002/app.1960.070041224.

[20]   R. Critchley, I. Corni, J.A. Wharton, F.C. Walsh, R.J.K. Wood, K.R. Stokes, A review of the manufacture, mechanical properties and potential applications of auxetic foams, Physica Status Solidi (B) Basic Research. Vol. 250, (2013), pp. 1963-1982, https://doi.org/10.1002/pssb.201248550.

[21]   O.S. Carneiro, A.F. Silva, R. Gomes, Fused deposition modeling with polypropylene, Materials and Design. Vol. 83, (2015), pp. 768-776, https://doi.org/10.1016/j.matdes.2015.06.053.

[22] J. Simpson, Z. Kazancı, Crushing investigation of crash boxes filled with honeycomb and re-entrant (auxetic) lattices, Thin-Walled Structures. Vol. 150, (2020), pp. 106676-106690, https://doi.org/10.1016/j.tws.2020.106676.

[23] X. Hou, Z. Deng, K. Zhang, Dynamic crushing strength analysis of auxetic honeycombs, China Acta Mechanica Solida Sinica. Vol. 29, (2016), pp 490-501, https://doi.org/10.1016/S0894-9166(16)30267-1.

[24] H. Yang, B. Wang, L. Ma, Mechanical properties of 3D double-U auxetic structures, International Journal of Solids and Structures. Vol. 180–181, (2019), pp. 13–29, https://doi.org/10.1016/j.ijsolstr.2019.07.007.

[25] Y. Wu, L. Yang, The effect of unit cell size and topology on tensile failure behavior of 2D lattice structures, International Journal of Mechanical Sciences. Vol. 170, (2020), pp. 105342-105356, https://doi.org/10.1016/j.ijmecsci.2019.105342.

[26] L. Dong, Mechanical responses of Ti-6Al-4V cuboctahedral truss lattice structures, Composite Structures. Vol. 235, (2020), pp. 111815-111831, https://doi.org/10.1016/j.compstruct.2019.111815.

[27] M.R. Karamooz Ravari, M. Kadkhodaei, M. Badrossamay, R. Rezaei, Numerical investigation on mechanical properties of cellular lattice structures fabricated by fused deposition modeling, International Journal of Mechanical Sciences. Vol. 88, (2014), 154–161, https://doi.org/10.1016/j.ijmecsci.2014.08.009.

[28] M. Mahbod, M. Asgari, Elastic and plastic characterization of a new developed additively manufactured functionally graded porous lattice structure: Analytical and numerical models, International Journal of Mechanical Sciences. Vol. 155, (2019), pp. 248–266, https://doi.org/10.1016/j.ijmecsci.2019.02.041.

[29] J. Chen, N. Chu, M. Zhao, F.L. Jin, S.J. Park, Synthesis and application of thermal latent initiators of epoxy resins: A review, Journal of Applied Polymer Science. Vol. 137, (2020), 49592, https://doi.org/10.1002/app.49592.

[30] R. Gautam, S. Idapalapati, S. Feih, Printing and characterisation of Kagome lattice structures by fused deposition modelling, Materials and Design. Vol. 137, (2018), pp. 266–275, https://doi.org/10.1016/j.matdes.2017.10.022.

[31] D. Zhang, J. Yu, H. Li, X. Zhou, C. Song, C. Zhang, S. Shen, L. Liu, C. Dai, Investigation of laser polishing of four selective laser melting alloy samples, Applied Sciences (Switzerland). Vol. 10, (2020), pp. 760-773, https://doi.org/10.3390/app10030760.

[32] X. Feng, L. Ma, H. Liang, X. Liu, J. Lei, W. Li, K. Wang, Y. Song, B. Wang, G. Li, S. Li, C. Yang, Osteointegration of 3D-printed fully porous polyetheretherketone scaffolds with different pore sizes, ACS Omega. Vol. 5, (2020), pp. 26655-26666, https://doi.org/10.1021/acsomega.0c03489.

[33] F. Wang, Systematic design of 3D auxetic lattice materials with programmable Poisson's ratio for finite strains, Journal of the Mechanics and Physics of Solids. Vol. 114, (2018), pp. 303–318, https://doi.org/10.1016/j.jmps.2018.01.013.

[34] X. Duan, J. Yu, Y. Zhu, Z. Zheng, Q. Liao, Y. Xiao, Y. Li, Z. He, Y. Zhao, H. Wang, L. Qu, Large-scale spinning approach to engineering knittable hydrogel fiber for soft robots, ACS Nano. Vol. 14, (2020), pp. 14929-14938, https://doi.org/10.1021/acsnano.0c04382.

[35] M.J. Choi, S.H. Kang, M.H. Oh, S. Cho, Controllable optimal design of auxetic structures for extremal Poisson's ratio of −2, Composite Structures. Vol. 226, (2019), pp. 111215-111228, https://doi.org/10.1016/j.compstruct.2019.111215.

[36] C. Quan, B. Han, Z. Hou, Q. Zhang, X. Tian, T.J. Lu, 3d printed continuous fiber reinforced composite auxetic honeycomb structures, Composites Part B: Engineering. vol. 187, (2020), pp. 107858-108870, https://doi.org/10.1016/j.compositesb.2020.107858.

[37] Y. Hou, Y.H. Tai, C. Lira, F. Scarpa, J.R. Yates, B. Gu, The bending and failure of sandwich structures with auxetic gradient cellular cores, Composites Part A:

Applied Science and Manufacturing. Vol. 49, (2013), pp. 119–131, https://doi.org/10.1016/j.compositesa.2013.02.007.

[38] V.H. Carneiro, H. Puga, Axisymmetric auxetics, Composite Structures. Vol. 204, (2018), pp. 438–444, https://doi.org/10.1016/j.compstruct.2018.07.116.

[39] T. Li, Y. Chen, X. Hu, Y. Li, L. Wang, Exploiting negative Poisson's ratio to design 3D-printed composites with enhanced mechanical properties, Materials and Design. Vol. 142, (2018), pp. 247–258, https://doi.org/10.1016/j.matdes.2018.01.034.

[40] K. Wang, Y.H. Chang, Y.W. Chen, C. Zhang, B. Wang, Designable dual-material auxetic metamaterials using three-dimensional printing, Materials and Design. Vol. 67, (2015), pp. 159–164, https://doi.org/10.1016/j.matdes.2014.11.033.

[41] Y. Jiang, B. Rudra, J. Shim, Y. Li, Limiting strain for auxeticity under large compressive Deformation: Chiral vs. re-entrant cellular solids, International Journal of Solids and Structures. Vol. 162, (2019), pp. 87–95, https://doi.org/10.1016/j.ijsolstr.2018.11.035.

[42] D. Xiao, Z. Dong, Y. Li, W. Wu, D. Fang, Compression behavior of the graded metallic auxetic reentrant honeycomb: Experiment and finite element analysis, Materials Science and Engineering A. Vol. 758, (2019), pp. 163–171, https://doi.org/10.1016/j.msea.2019.04.116.

[43] Z. Dong, Y. Li, T. Zhao, W. Wu, D. Xiao, J. Liang, Experimental and numerical studies on the compressive mechanical properties of the metallic auxetic reentrant honeycomb, Materials and Design. Vol. 182, (2019), pp. 108036–108048, https://doi.org/10.1016/j.matdes.2019.108036.

[44] M.H. Fu, Y. Chen, L.L. Hu, A novel auxetic honeycomb with enhanced in-plane stiffness and buckling strength, Composite Structures. Vol. 160, (2017), pp. 574–585, https://doi.org/10.1016/j.compstruct.2016.10.090.

[45] J. Zhang, G. Lu, D. Ruan, Z. Wang, Tensile behavior of an auxetic structure: Analytical modeling and finite element analysis, International Journal of Mechanical Sciences. Vol. 136, (2018), pp. 143–154, https://doi.org/10.1016/j.ijmecsci.2017.12.029.

[46] Y. Yao, L. Wang, J. Li, S. Tian, M. Zhang, Y. Fan, A novel auxetic structure-based bone screw design: Tensile mechanical characterization and pullout fixation strength evaluation, Materials and Design. Vol. 188, (2020), pp. 108424–108435, https://doi.org/10.1016/j.matdes.2019.108424.

[47] H.M.A. Kolken, K. Lietaert, T. van der Sloten, B. Pouran, A. Meynen, G. van Loock, H. Weinans, L. Scheys, A.A. Zadpoor, Mechanical performance of auxetic meta-biomaterials, Journal of the Mechanical Behavior of Biomedical Materials. Vol. 104, (2020), pp. 103658–103671, https://doi.org/10.1016/j.jmbbm.2020.103658.

[48] P.H. Cong, P.T. Long, N. van Nhat, N.D. Duc, Geometrically nonlinear dynamic response of eccentrically stiffened circular cylindrical shells with negative poisson's ratio in auxetic honeycombs core layer, International Journal of Mechanical Sciences. Vol. 152, (2019), pp. 443–453, https://doi.org/10.1016/j.ijmecsci.2018.12.052.

[49] Y. Xue, W. Wang, F. Han, Enhanced compressive mechanical properties of aluminum based auxetic lattice structures filled with polymers, Composites Part B: Engineering. Vol. 171, (2019), pp. 183–191, https://doi.org/10.1016/j.compositesb.2019.05.002.

[50] H.L. Tan, Z.C. He, K.X. Li, E. Li, A.G. Cheng, B. Xu, In-plane crashworthiness of re-entrant hierarchical honeycombs with negative Poisson's ratio, Composite Structures. Vol. 229, (2019). pp. 111415–111430, https://doi.org/10.1016/j.compstruct.2019.111415.

[51] Y. Xue, X. Wang, W. Wang, X. Zhong, F. Han, Compressive property of Al-based auxetic lattice structures fabricated by 3-D printing combined with investment casting, Materials Science and Engineering A. Vol. 722, (2018), pp. 255–262, https://doi.org/10.1016/j.msea.2018.02.105.

[52] Q. Gao, W.H. Liao, L. Wang, An analytical model of cylindrical double-arrowed honeycomb with negative Poisson's ratio, International Journal of Mechanical Sciences. Vol. 173, (2020), pp. 105400-105410, https://doi.org/10.1016/j.ijmecsci.2019.105400.

[53] Q. Gao, C.A. Tan, G. Hulbert, L. Wang, Geometrically nonlinear mechanical properties of auxetic double-V microstructures with negative Poisson's ratio, European Journal of Mechanics, A/Solids. Vol. 80, (2020), pp. 103933–103944, https://doi.org/10.1016/j.euromechsol.2019.103933.

[54] Y. Xue, F. Han, Compressive mechanical property of a new three-dimensional aluminum based double-V lattice structure, Materials Letters. Vol. 254, (2019), pp. 99–102, https://doi.org/10.1016/j.matlet.2019.07.048.

[55] Q. Gao, L. Wang, Z. Zhou, Z.D. Ma, C. Wang, Y. Wang, Theoretical, numerical and experimental analysis of three-dimensional double-V honeycomb, Materials and Design. Vol. 139, (2018), pp. 380–391, https://doi.org/10.1016/j.matdes.2017.11.024.

[56] L. Wei, X. Zhao, Q. Yu, G. Zhu, A novel star auxetic honeycomb with enhanced in-plane crushing strength, Thin-Walled Structures. Vol. 149, (2020), pp. 106623–106638, https://doi.org/10.1016/j.tws.2020.106623.

[57] X. Li, L. Gao, W. Zhou, Y. Wang, Y. Lu, Novel 2D metamaterials with negative Poisson's ratio and negative thermal expansion, Extreme Mech Lett. Vol. 30, (2019), pp. 100498–100517, https://doi.org/10.1016/j.eml.2019.100498.

[58] L. Ai, X.L. Gao, An analytical model for star-shaped re-entrant lattice structures with the orthotropic symmetry and negative Poisson's ratios, International

Journal of Mechanical Sciences. Vol. 145, (2018), pp. 158–170, https://doi.org/10.1016/j.ijmecsci.2018.06.027.

[59] L.L. Hu, Z.R. Luo, Q.Y. Yin, Negative Poisson's ratio effect of re-entrant anti-trichiral honeycombs under large deformation, Thin-Walled Structures. Vol. 141, (2019), pp. 283–292, https://doi.org/10.1016/j.tws.2019.04.032.

[60] L.L. Hu, Z.J. Wu, M.H. Fu, Mechanical behavior of anti-trichiral honeycombs under lateral crushing, International Journal of Mechanical Sciences. Vol. 140, (2018), pp. 537–546, https://doi.org/10.1016/j.ijmecsci.2018.03.039.

[61] R. Hamzehei, S. Rezaei, J. Kadkhodapour, A.P. Anaraki, A. Mahmoudi, 2D triangular anti-trichiral structures and auxetic stents with symmetric shrinkage behavior and high energy absorption, Mechanics of Materials. Vol. 142, (2020), pp. 103291–103301, https://doi.org/10.1016/j.mechmat.2019.103291.

[62] F. Auricchio, A. Bacigalupo, L. Gambarotta, M. Lepidi, S. Morganti, F. Vadalà, A novel layered topology of auxetic materials based on the tetrachiral honeycomb microstructure, Materials and Design. Vol. 179, (2019), https://doi.org/10.1016/j.matdes.2019.107883.

[63] M. Fu, F. Liu, L. Hu, A novel category of 3D chiral material with negative Poisson's ratio, Composites Science and Technology. Vol. 160, (2018), pp. 111–118, https://doi.org/10.1016/j.compscitech.2018.03.017.

[64] C. Ma, H. Lei, J. Liang, W. Wu, T. Wang, D. Fang, Macroscopic mechanical response of chiral-type cylindrical metastructures under axial compression loading, Materials and Design. Vol. 158, (2018), pp. 198–212, https://doi.org/10.1016/j.matdes.2018.08.022.

[65] W. Wu, X. Song, J. Liang, R. Xia, G. Qian, D. Fang, Mechanical properties of anti-tetrachiral auxetic stents, Composite Structures. Vol. 185, (2018), pp. 381–392, https://doi.org/10.1016/j.compstruct.2017.11.048.

[66] B. Nečemer, S. Glodež, N. Novak, J. Kramberger, Numerical modelling of a chiral auxetic cellular structure under multiaxial loading conditions, Theoretical and Applied Fracture Mechanics. Vol. 107, (2020), https://doi.org/10.1016/j.tafmec.2020.102514.

[67] K.E. Evans, Auxetic polymers: a new range of materials, Endeavour. Vol. 15, (1991), pp. 170-174, https://doi.org/10.1016/0160-9327(91)90123-S.

[68] G. Nabiyouni, H. Halakouie, D. Ghanbari, Microwave synthesis of different morphologies of lead ferrite nanostructures and investigation of magnetic properties, Journal of Nanostructures. Vol. 7, (2017), pp. 77-81, https://doi.org/10.22052/jns.2017.01.009.

[69] R. Lakes, Foam structures with a negative poisson's ratio, Science (1979). Vol. 235, (1987), pp. 1038-1040, https://doi.org/10.1126/science.235.4792.1038.

[70] K.L. Alderson, A. Fitzgerald, K.E. Evans, The strain dependent indentation resilience of auxetic microporous polyethylene, Journal of Materials Science. Vol. 35, (2000), pp. 4039-4047, https://doi.org/10.1023/A:1004830103411.

[71] G.E.P. Box, D.W. Behnken, Some New Three Level Designs for the Study of Quantitative Variables, Technometrics. Vol. 2, (1960), pp. 455–475, https://doi.org/10.1080/00401706.1960.10489912.

[72] A.R. Damanpack, M. Bodaghi, W.H. Liao, Experimentally validated multi-scale modeling of 3D printed hyper-elastic lattices, International Journal of Non-Linear Mechanics. Vol. 108, (2019), pp. 87–110, https://doi.org/10.1016/j.ijnonlinmec.2018.10.008.

[73] M.R.K Ravari, M. Kadkhodaei, M. Badrossamay, R. Rezaei, Numerical investigation on mechanical properties of cellular lattice structures fabricated by fused deposition modeling, International Journal of Mechanical Sciences. Vol. 88, (2014), pp. 154–161, https://doi.org/10.1016/j.ijmecsci.2014.08.009.

[74] G. Yan, M.J. Tan, A. Crivoi, F. Li, S. Kumar, & C.H. Nicholas, Improving the mechanical properties of TIG welding Ti-6Al-4V by post weld heat treatment, Procedia Engineering, Vol. 207, (2017), pp. 633–638, https://doi.org/10.1016/J.PROENG.2017.10.1033

[75] P. Edwards, & M. Ramulu, Fatigue performance of Friction Stir Welded Ti–6Al–4V subjected to various post weld heat treatment temperatures, International Journal of Fatigue, Vol. 75, (2015), pp. 19–27, https://doi.org/10.1016/J.IJFATIGUE.2015.01.012

[76] B.W. Chieng, N.A. Ibrahim, W.M.Z. Wan Yunus, M.Z. Hussein, Effects of graphene nanopletelets on poly(lactic acid)/poly(ethylene glycol) polymer nanocomposites, in: Advanced Materials Research, Vol. 6, (2014), pp. 136-139, https://doi.org/10.4028/www.scientific.net/AMR.1024.136.

[77] W.C. Hung, S.H. Fu, J.J. Tseng, H. Chu, T.H. Ko, Study on photocatalytic degradation of gaseous dichloromethane using pure and iron ion-doped TiO_2 prepared by the sol-gel method, Chemosphere. Vol. 66, (2007), pp. 2142–2151, https://doi.org/10.1016/j.chemosphere.2006.09.037.

[78] H. Liu, Y. Pei, D. Xie, X. Deng, Y.X. Leng, Y. Jin, N. Huang, Surface modification of ultra-high molecular weight polyethylene (UHMWPE) by argon plasma, Applied Surface Science. Vol. 256, (2010), pp. 3941-3945, https://doi.org/10.1016/j.apsusc.2010.01.054.

[79] S. Durdu, G. Cihan, E. Yalcin, A. Altinkok, Characterization and mechanical properties of TiO_2 nanotubes formed on titanium by anodic oxidation, Ceramics International. Vol. 47, (2021), pp. 10972-10979, https://doi.org/10.1016/j.ceramint.2020.12.218.

[80] S. Nanaki, P. Barmpalexis, A. Iatrou, E. Christodoulou, M. Kostoglou, D.N. Bikiaris, Risperidone controlled release microspheres based on poly(lactic acid)-poly(propylene adipate) novel polymer blends appropriate for long acting

injectable formulations, Pharmaceutics. Vol. 10, (2018), pp. 130-151, https://doi.org/10.3390/pharmaceutics10030130.

[81] Z. Ren, L. Dong, Y. Yang, Dynamic mechanical and thermal properties of plasticized poly(lactic acid), Journal of Applied Polymer Science. Vol. 101, (2006), pp. 1583-1590, https://doi.org/10.1002/app.23549.

[82] V.S. Giita Silverajah, N.A. Ibrahim, W. Md Zin Wan Yunus, H.A. Hassan, C.B. Woei, A comparative study on the mechanical, thermal and morphological characterization of poly(lactic acid)/epoxidized palm oil blend, International Journal of Molecular Sciences. Vol. 13, (2012), pp. 5878,5898, https://doi.org/10.3390/ijms13055878.

[83] Z. Yang, X.L. Zong, Z. Ye, B. Zhao, Q.L. Wang, P. Wang, The application of complex multiple forklike ZnO nanostructures to rapid and ultrahigh sensitive hydrogen peroxide biosensors, Biomaterials. Vol. 31, (2010), pp. 7534,7541, https://doi.org/10.1016/j.biomaterials.2010.06.019.

[84] S. Krishnamohan, S. Ramanathan, Synthesis and characterization of Ti6Al4V alloy by powder metallurgy, International Journal of Engineering Research and Technology. Vol. 2, (2013), pp. 2725-2729.

[85] U.T. Kalyoncuoglu, B. Yilmaz, S. Gungor, Z. Evis, P. Uyar, G. Akca, G. Kansu, Evaluation of the chitosan-coating effectiveness on a dental titanium alloy in terms of microbial and fibroblastic attachment and the effect of aging, Materiali in Tehnologije. Vol. 49, (2015), pp. 925-931, https://doi.org/10.17222/mit.2014.239.

[86] C. Abeykoon, P. Sri-Amphorn, & A. Fernando, Optimization of fused deposition modeling parameters for improved PLA and ABS 3D printed structures. International Journal of Lightweight Materials and Manufacture, Vol. 3, (2020), pp. 284–297, https://doi.org/10.1016/j.ijlmm.2020.03.003.

[87] M. Kodal, A. A. Wis, & G. Ozkoc, The mechanical, thermal and morphological properties of γ-irradiated PLA/TAIC and PLA/OvPOSS. Radiation Physics and Chemistry, Vol. 153, (2018), pp. 214–225, https://doi.org/10.1016/j.radphyschem.2018.10.018

[88] X. Zhou, J. Deng, C. Fang, W. Lei, Y. Song, Z. Zhang, Z. Huang, & Y. Li, Additive manufacturing of CNTs/PLA composites and the correlation between microstructure and functional properties. Journal of Materials Science and Technology, Vol. 60, (2021), pp. 27–34, https://doi.org/10.1016/j.jmst.2020.04.038

[89] F. Hayoune, S. Chelouche, D. Trache, S. Zitouni, & Y. Grohens, Thermal decomposition kinetics and lifetime prediction of a PP/PLA blend supplemented with iron stearate during artificial aging, Thermochimica Acta. Vol. 690, (2020), pp. 178700, https://doi.org/10.1016/j.tca.2020.178700

[90] S. Xiang, L. Feng, X. Bian, G. Li, & X. Chen, Evaluation of PLA content in PLA/PBAT blends using TGA, Polymer Testing. Vol 81, (2020), pp. 106211, https://doi.org/10.1016/j.polymertesting.2019.106211

[91] M. Zheng, S. Zhang, Y. Chen, Q. Wu, Q. Li, & S. Wang, Structure evolution of bio-based PLA/ENR thermoplastic vulcanizates during dynamic vulcanization processing. Polymer Testing, Vol. 82, (2020), pp. 106324, https://doi.org/10.1016/j.polymertesting.2020.106324,

[92] M. Lei, W. Hong, Z. Zhao, C. Hamel, M. Chen, H. Lu, 3D printing of auxetic metamaterials with digitally reprogrammable shape, ACS Appl Mater Interfaces. Vol. 11(25), (2019), pp. 68–76.

[93] F. Auricchio, A. Bacigalupo, L. Gambarotta, M. Lepidi, S. Morganti, F. Vadala, A novel layered topology of auxetic materials based on the tetrachiral honeycomb microstructure, Materials and Design. Vol. 179, (2019), pp. 107883.

[94] M. Fu, F. Liu, L. Hu, A novel category of 3D chiral material with negative Poisson's ratio, Composites Science and Technology. Vol. 160, (2018), pp. 111-118, https://doi.org/10.1016/j.compscitech.2018.03.017.

[95] C. Ma, H. Lei, J. Liang, W. Wu, T. Wang, D. Fang, Macroscopic mechanical response of chiral-type cylindrical metastructures under axial compression loading, Materials and Design. Vol. 158, (2018b), pp. 198–212, https://doi.org/10.1016/j.matdes.2018.08.022

[96] M.H. Fu, Y. Chen, L.L. Hu, A novel auxetic honeycomb with enhanced in-plane stiffness and buckling strength, Composite Structures. Vol. 160, (2017), pp. 574–585, https://doi.org/10.1016/j.compstruct.2016.10.090.

[97] H. Wang, Y. Zhang, W. Lin, Q.H. Qin, A novel two-dimensional mechanical metamaterial with negative Poisson's ratio, Computational Materials Science, Vol. 171, (2020), pp. 109232, https://doi.org/10.1016/j.commatsci.2019.109232.

[98] Y. Yao, L. Wang, J. Li, S. Tian, M. Zhang, Y. Fan, A novel auxetic structure-based bone screw design: Tensile mechanical characterization and pullout fixation strength evaluation, Materials and Design. Vol. 188, (2020), pp. 108424, https://doi.org/10.1016/j.matdes.2019.108424

[99] J. Simpson, Z. Kazancı, Crushing investigation of crash boxes filled with honeycomb and re-entrant (auxetic) lattices, Thin–Walled Structures. Vol. 150, (2020), pp. 106676, https://doi.org/10.1016/j.tws.2020.106676